AD NUMBER
ADB010797
LIMITATION CHANGES

TO:

Approved for public release; distribution is unlimited.

FROM:

Distribution authorized to U.S. Gov't. agencies only; Test and Evaluation; JAN 1976. Other requests shall be referred to Air Force Weapons Laboratory, DEV, Kirtland AFB, NM 87117.

AUTHORITY

AFWL ltr, 29 APR 1985

AD _ BD10797

ADB010797

AN INVESTIGATION OF AIRBLAST DIFFRACTION LOADING ON SIMPLE STRUCTURAL SHAPES

January 1976

Final Report

Distribution limited to US Government agencies only because test and evaluation of military systems is discussed in the report (Jan 76). Other requests for this document must be referred to AFWL (DEV), Kirtland AFB, NM, 87117.

This research was sponsored by the Defense Nuclear Agency under Subtask Y99QAXSC157, Work Unit 04, Work Unit Title: Strategic Structure Vulnerability/Hardening.

Prepared for
Director
DEFENSE NUCLEAR AGENCY
Washington, DC 20305

DDC
RECEIVED
MAY 7 1976
B

AIR FORCE WEAPONS LABORATORY
Air Force Systems Command
Kirtland Air Force Base, NM 87117
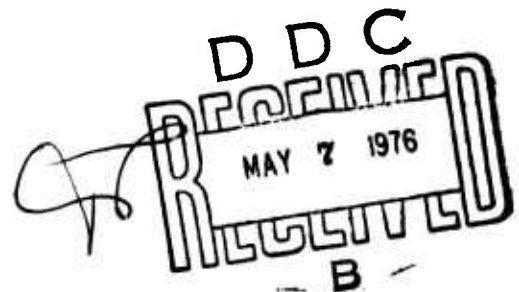
AD No.
DDC FILE COPY

2608

This final report was prepared by the Air Force Weapons Laboratory, Kirtland AFB, NM, for the Defense Nuclear Agency under Job Order WDNS3424. Dr. Maynard A. Plamondon (DEV) was the Laboratory Project Officer-in-Charge. Captain Jerry S. Doughty was the former project officer.

When US Government drawings, specifications, or other data are used for any purpose other than a definitely related Government procurement operation, the Government thereby incurs no responsibility nor any obligation whatsoever, and the fact that the Government may have formulated, furnished, or in any way supplied the said drawings, specifications, or other data is not to be regarded by implication or otherwise as in any manner licensing the holder or any other person or corporation or conveying any rights or permission to manufacture, use or sell any patented invention that may in any way be related thereto.

This technical report has been reviewed and is approved for publication.

MAYNARD A. PLAMONDON, PhD
Project Officer

FOR THE COMMANDER

JAMES M. WARREN
Lt Colonel, USAF
Chief, Facility Survivability
 Branch

FRANK J. LEECH
Lt Colonel, USAF
Chief, Civil Engineering Research
 Division

DO NOT RETURN THIS COPY. RETAIN OR DESTROY.

1

REPORT DOCUMENTATION PAGE		READ INSTRUCTIONS BEFORE COMPLETING FORM
1. REPORT NUMBER AFWL-TR-75-290	2. GOVT ACCESSION NO.	3. RECIPIENT'S CATALOG NUMBER
4. TITLE (and Subtitle) AN INVESTIGATION OF AIRBLAST DIFFRACTION LOADING ON SIMPLE STRUCTURAL SHAPES.		5. TYPE OF REPORT & PERIOD COVERED Final Report. Mar 73 - Dec 75
		6. PERFORMING ORG. REPORT NUMBER
7. AUTHOR(s) Jerry S. Doughty, Captain, USAF		8. CONTRACT OR GRANT NUMBER(s) 353 p.
9. PERFORMING ORGANIZATION NAME AND ADDRESS Air Force Weapons Laboratory (DEV) Kirtland AFB, NM 87117		10. PROGRAM ELEMENT, PROJECT, TASK AREA & WORK UNIT NUMBERS 62704H; WDNS3424: Subtask Y99QAXSC157
11. CONTROLLING OFFICE NAME AND ADDRESS Air Force Weapons Laboratory (DEV) Kirtland AFB, NM 87117		12. REPORT DATE Jan 1976
		13. NUMBER OF PAGES 362
14. MONITORING AGENCY NAME & ADDRESS(if different from Controlling Office) Director Defense Nuclear Agency Washington, D.C. 20305	DNA-NWED-QAXS C157	15. SECURITY CLASS. (of this report) UNCLASSIFIED
		15a. DECLASSIFICATION/DOWNGRADING SCHEDULE

16. DISTRIBUTION STATEMENT (of this Report)

Distribution limited to US Government agencies only because test and evaluation of military systems is discussed in the report (Jan 76). Other requests for this document must be referred to AFWL (DEV), Kirtland AFB, NM, 87117.

17. DISTRIBUTION STATEMENT (of the abstract entered in Block 20, if different from Report)

18. SUPPLEMENTARY NOTES

This research was sponsored by the Defense Nuclear Agency under Subtask Y99QAXSC157, Work Unit 04, Work Unit Title: Strategic Structure Vulnerability/Hardening.

19. KEY WORDS (Continue on reverse side if necessary and identify by block number)

Airblast; Airblast loads; Shock tube; Diffraction loading; High pressure; Reflection factor; Drag coefficient; Structural design

20. ABSTRACT (Continue on reverse side if necessary and identify by block number)

The primary objective of this investigation was to determine the adequacy of current simplified techniques for predicting airblast loadings on exposed aboveground structures subjected to high incident overpressures. The experimental program consisted of testing basic two-dimensional shapes in a 13-inch diameter, high-pressure shock tube. Rectangular and cylindrical configurations were tested at nominal incident overpressures of 100 and 300 psi. The investigation was limited to early time loading because the initial diffraction period

(cont on p 1473 B)

DD FORM 1473 1 JAN 73 EDITION OF 1 NOV 85 IS OBSOLETE

013 150

was considered the area of greatest uncertainty. Pressure measurements were recorded on the front, roof, and rear sections of the rectangle and at specified intervals around the upper half of the cylindrical model. Additional measurements were taken on a simulated ground plane in front of both structures. The effect of a horizontal roof extension on both structures was also investigated. The experimental data were used to provide a description of the phenomenology associated with high-pressure shock diffraction and an evaluation of current simplified prediction techniques. The prediction techniques evaluated were those presented in The Air Force Manual for Design and Analysis of Hardened Structures (AFWL-TR-74-102). The prediction techniques for rectangular structural loads were fairly reliable. However, suggestions for additional improvements in the techniques were presented. The evaluations indicate that unsatisfactory techniques exist for determining pointwise structural loads on the cylindrical model and for determining ground surface loads in front of an above-ground obstruction. During the investigation, the upper half of the cylindrical model was considered to be an arch structure. It is recommended that future efforts consider parametric investigations using reliable current computer codes as a data base for improving the simplified prediction techniques.

PREFACE

The experimental testing described within this report was conducted by the Civil Engineering Research Facility (CERF) operated by the University of New Mexico under contract F29601-72-C-0024, Work Order 4.01C. This testing was performed by Mr. Robert O. Clark with the assistance of Mr. Wayne McMurtry. Mr. Clark also provided information used in this report to describe the instrumentation and testing procedures. Mr. Douglas Seemann, formerly of the Air Force Weapons Laboratory, was responsible for the conversion of digital data to final engineering units and the resulting data plots. Captain Jerry S. Doughty of the Air Force Weapons Laboratory was the Laboratory Project Officer from March 1973 until April 1975. Dr. Maynard A. Plamondon was the Laboratory Project Officer from April 1975 until December 1975.

CONTENTS

CONTENTS (Continued)

ILLUSTRATIONS

ILLUSTRATIONS (Continued)

TABLES

SECTION I

INTRODUCTION

1. BACKGROUND

Two basic criteria must be satisfied to provide accurate design or analysis of structures. First, the applied loading conditions on the structure must be defined and, second, structural behavior models must be available which adequately simulate the structure's response under the applied loading conditions. The calculations involved can range anywhere from simple hand solutions to complex computer codes. The required complexity of the loading function will depend upon the degree of refinement attempted in analyzing the structure.

For an aboveground structure subjected to airblast loading, the external boundary conditions are composed of (a) the airblast induced pressures acting on the exposed faces of the structure and (b) the foundation reactions resulting from these pressure loadings and the motions of the structure.

These airblast loadings have generally been determined by one of the following methods.

    a. Extension of experimental data derived from high explosive tests and shock tube and wind tunnel experiments.

    b. Theoretical calculations based on ideal gases.

    c. Large hydrodynamic codes employing theory and experimental data as the basis of their behavior models.

Since most experiments have been conducted at incident overpressures less than 50 psi and only a few tests above 100 psi, the use of empirical methods without verification becomes questionable at higher pressures; extrapolation can be misleading and ideal gas behavior may no longer apply.

2. OBJECTIVE

The primary objective of this investigation was to determine the adequacy of current techniques for predicting airblast loadings on exposed aboveground structures subjected to high incident overpressures. To satisfy this objective, experimental data were collected to evaluate and refine current simplified techniques and complex mathematical models. Because the initial diffraction loading

phase was considered the area of greatest uncertainty, this investigation was directed at the early time loading of simple structural shapes. Two basic shapes, a rectangular block and a cylinder, were subjected to nominal 100 and 300 psi incident overpressure levels. Pressure measurements were recorded on the front, roof, and rear section of the rectangle and at specified intervals around the upper front and rear of the cylinder. Additional measurements were taken on a simulated ground plane in front of both structures. The effect of a horizontal roof extension on both structures was also investigated.

The experimental data were used to provide both a description of the phenomenology associated with high pressure shock diffraction and an evaluation of current simplified prediction techniques specified by The Air Force Manual for the Design and Analysis of Hardened Structures. An evaluation of a more complex analytic technique for predicting airblast diffraction is reported in reference 1 and employs the data collected under this effort.

3. APPROACH

The experimental phase consisted of testing basic two dimensional structural shapes in a 13-inch diameter high-pressure shock tube. The time duration of interest and height and depth of the test structures were such that the effects of the third dimension are not inherent in the test presented. The shock tube used in this investigation was a combustible gas driven tube located at the Civil Engineering Research Facility, Kirtland AFB, New Mexico. Nominal 100 and 300 psi st shock pulses were used as incident loading conditions on the test structures shown in figure 1. Representative waveforms of each loading are shown in figure 2. Figures 1.(a) and 1.(b) show the basic rectangular and cylindrical structures and also indicate the central gage locations for measuring pressure. The supports for both structures were designed such that each structure could be rotated between tests allowing measurements at all locations around the structures. Figures 1.(c) and 1.(d) show the wedges used to slice the incident shock wave and provide a surface for measuring reflected shocks propagating from the faces of the structures. The orientation view of these figures is such that the shock propagation direction is down and parallel to the plane of the figure. Two gage locations were chosen on the left faces of the wedges. These gages were on a line parallel to the direction of shock propagation and intersecting the stagnation point on the structure faces. Because the gages lie along a plane of symmetry with respect to the shock front and structure face, the test setup may be viewed as measurements along a ground
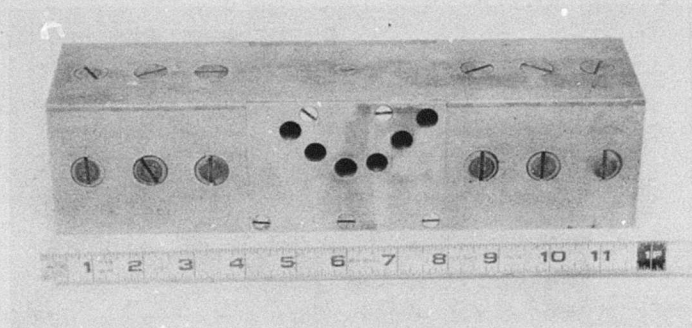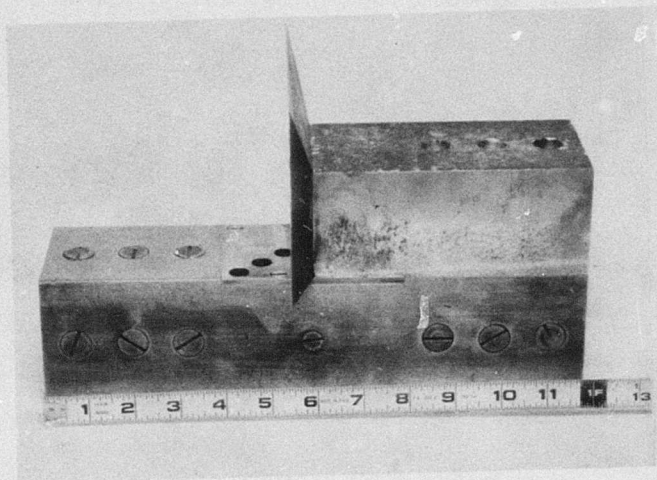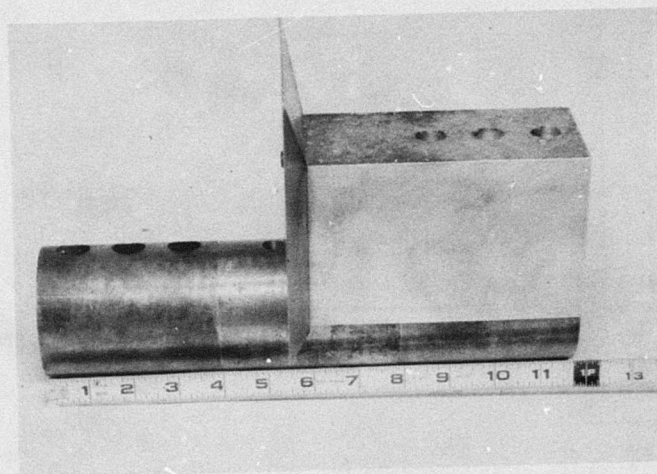
(a) Rectangular Structure
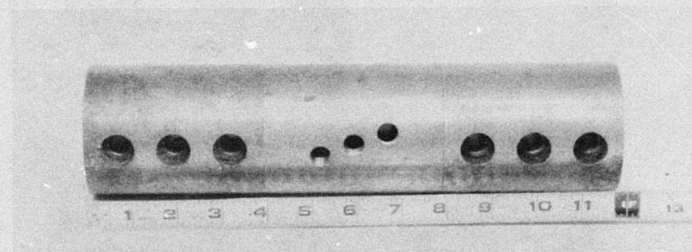
(b) Cylindrical Structure
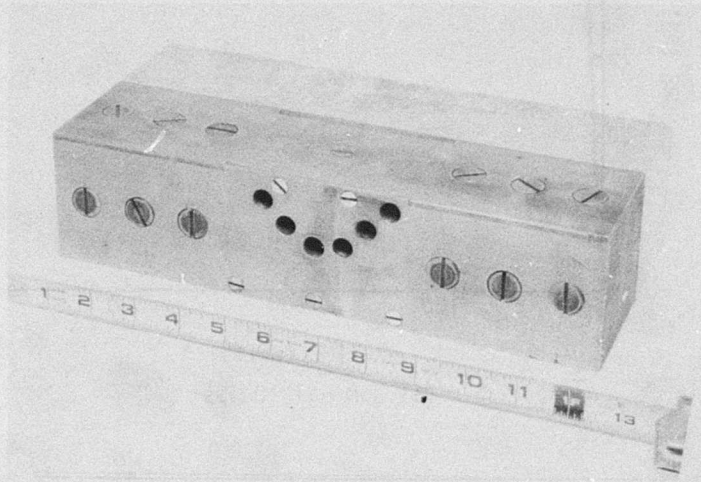
Figure 1. Test Structures
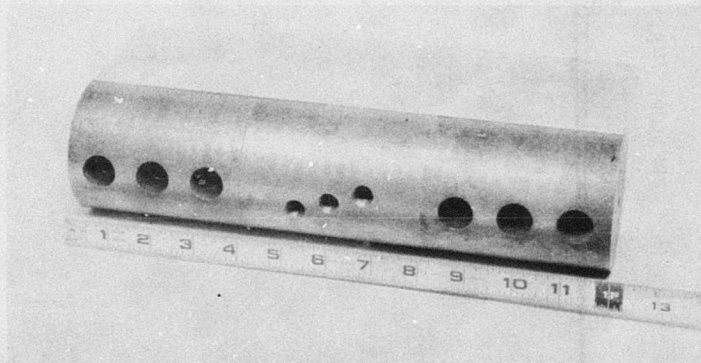
9

(c) Rectangle and Wedge Extension

(d) Cylinder and Wedge Extension

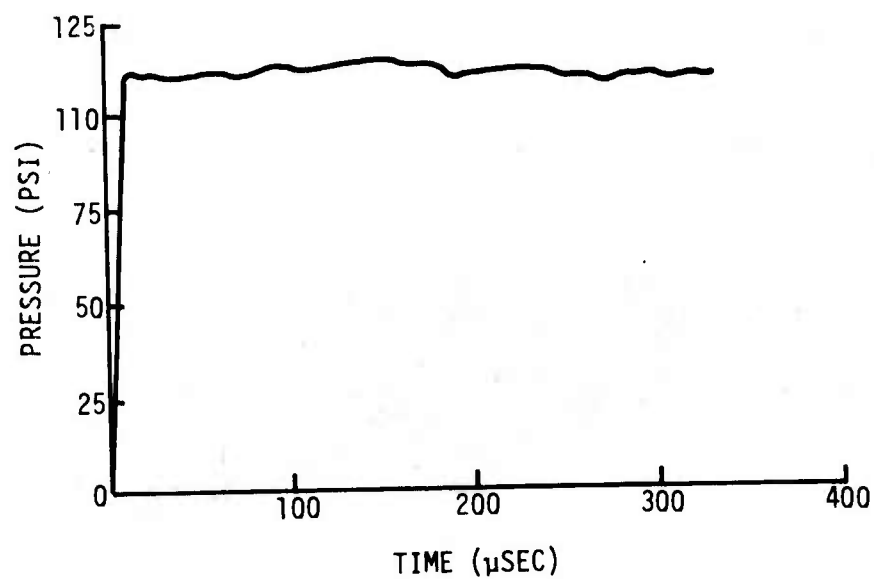Figure 1. Test Structures (Continued)
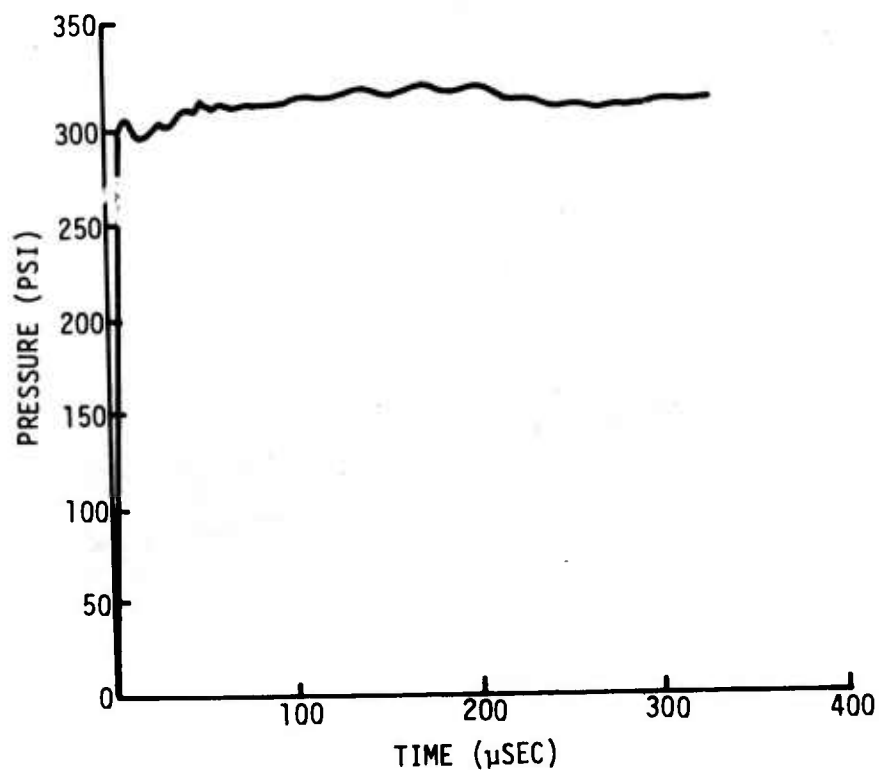
10

(e) Rectangle with Roof Extension

(f) Cylinder with Roof Extension

Figure 1. Test Structures (Continued)

(a) Nominal 100 psi

(b) Nominal 300 psi

Figure 2. Representative Incident Overpressure Waveforms

plane which intersects the midpoints of the structure face. Figures 1.(e) and 1.(f) show the roof extensions attached to the rectangle and cylinder. These were tested to determine whether the pressure loading on the front and top surfaces would be independent of the downstream extensions. In addition to the on-structure pressure measurements, measurements of incident pressure were made during each test for control purposes. Additional details concerning the test structures and gage locations are provided in figures 3 and 4.

After conversion to engineering units, the experimental data were evaluated to produce details associated with the shock diffraction process--details consisting primarily of reflected pressures, relief times to stagnation pressure, and vortex action on the top and rear of the structures. Once the basic phenomenology was described, the data were compared to predictions based on techniques specified in the available literature. These comparisons were then used to evaluate the validity of the prediction techniques.
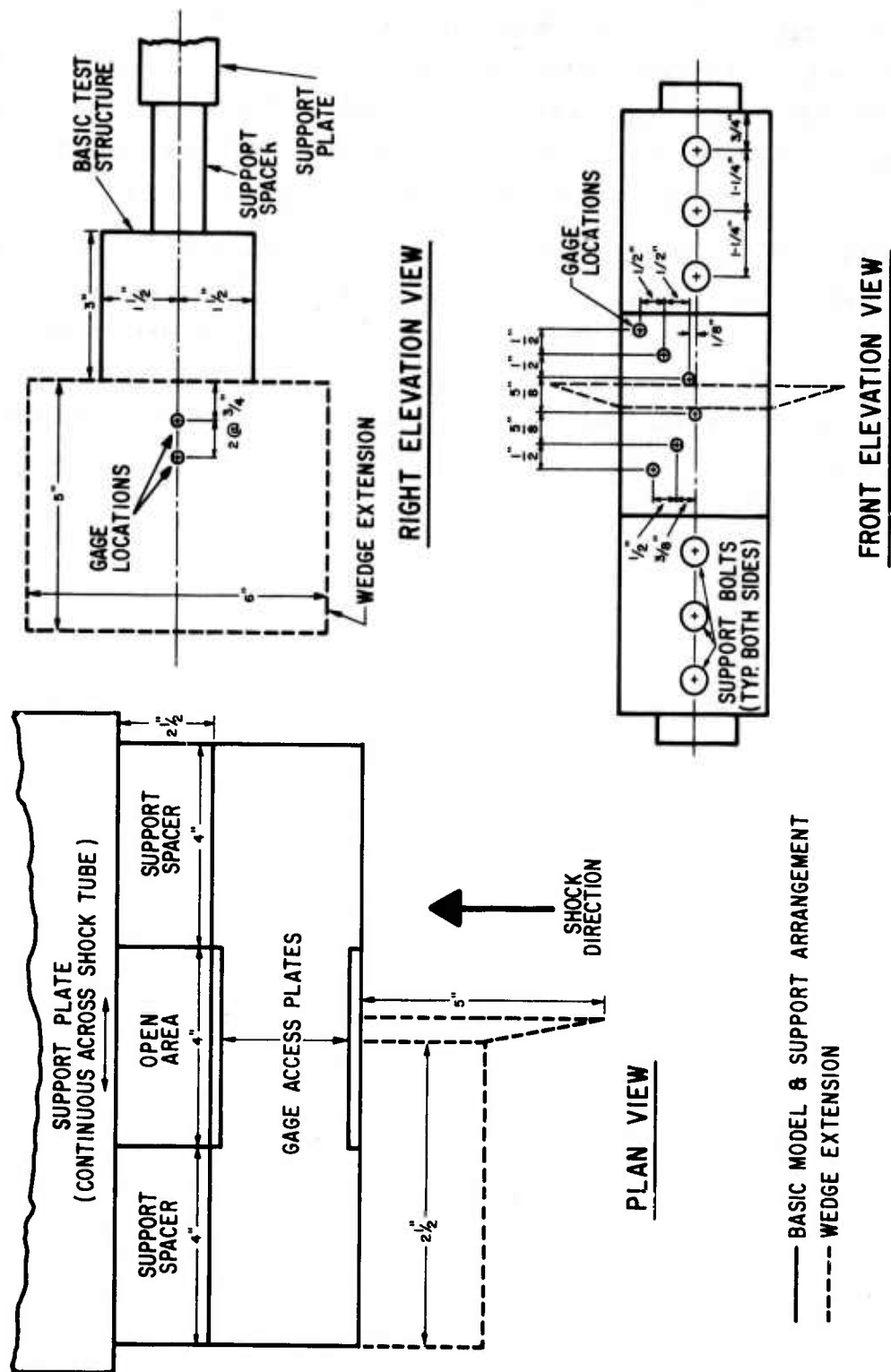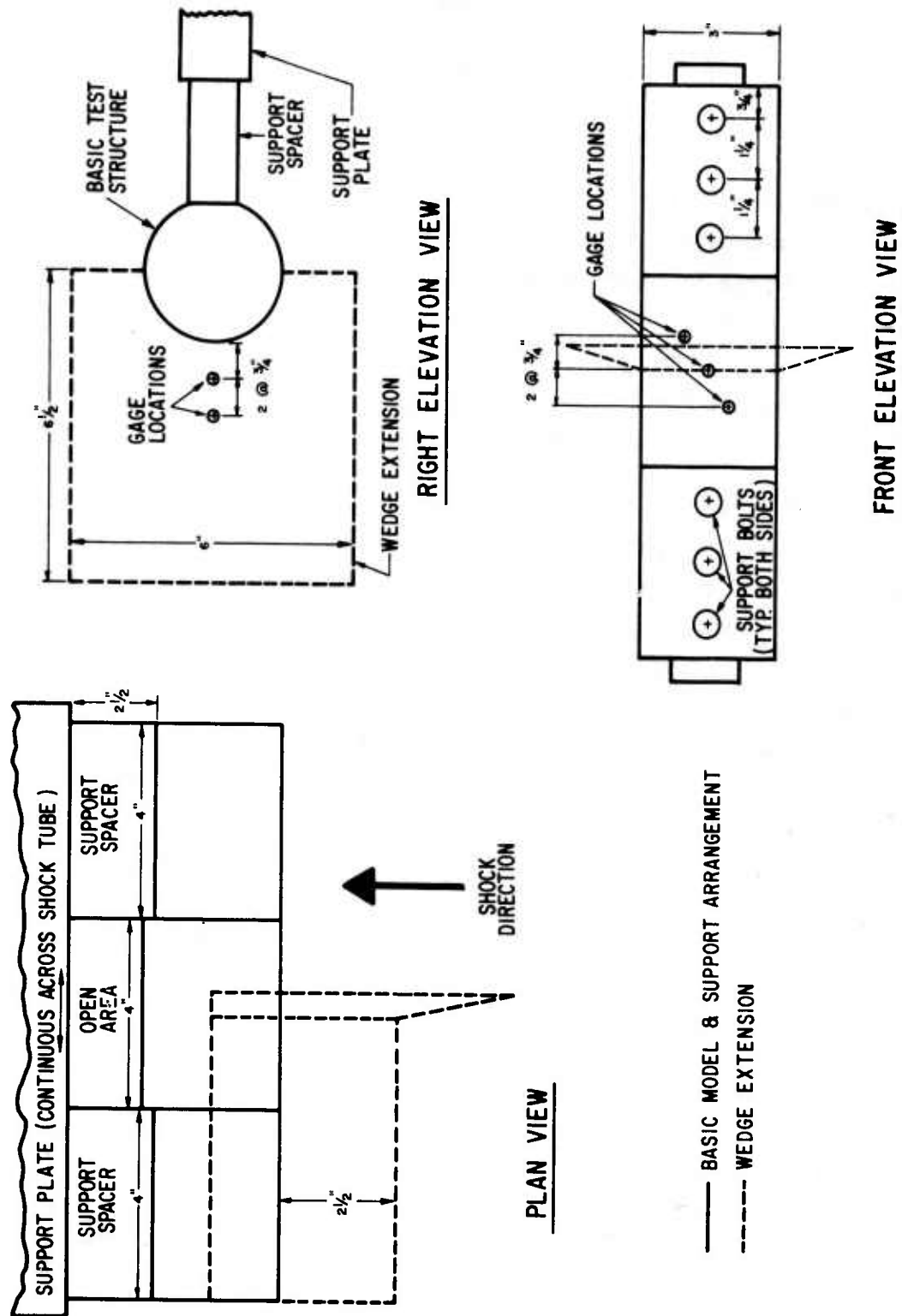
Figure 3. Rectangular Test Structure Details

RIGHT ELEVATION VIEW

FRONT ELEVATION VIEW

PLAN VIEW

Figure 4. Cylindrical Test Structure Details

15

SECTION II

TEST DESCRIPTION

1. SHOCK TUBE

A general description of the 13-in. high-pressure shock tube is shown in figure 5. Also depicted in this figure are the locations of the pressure gages used to monitor the incident pressure during each test and the velocity count and oscilloscope start triggers. The combustible gas for all tests consisted of one part oxygen to two parts hydrogen. The 15-ft. long combustion chamber is sufficient to produce a constant or step function shockwave for approximately 400 microseconds at the test station located 65 feet away.

2. TEST PREPARATION

After sealing both ends of the shock tube expansion chamber with thin aluminum sheeting, the hydrogen and oxygen gases were fed into the chamber and allowed to mix for a minimum time of 1 hour. Prior to this time the test structures had been instrumented and positioned in the test section. The test section was then sealed by closing the access ports. The instrumentation recording systems were given a final check and ambient measurements of temperature and pressure were made. Firing of the explosive gas mixture was accomplished by spark plugs equally spaced along the top and bottom lengths of the combustion chamber. The oscilloscopes used to record the transducer signals were automatically activated by the trigger gages located upstream from the test structures. These procedures were repeated for each test.
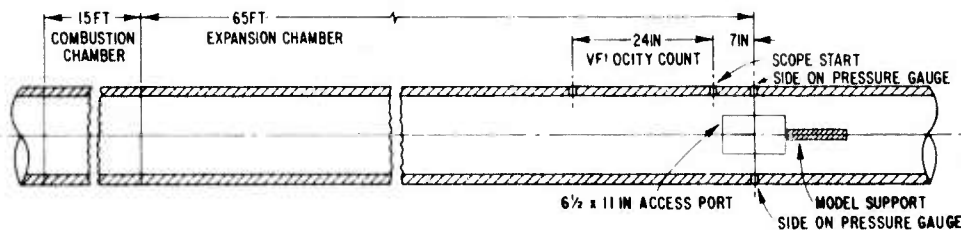

Figure 5. Thirteen-inch High-Pressure Shock Tube

3. TEST STRUCTURES

The test structures used in this investigation are shown in figure 1. The 3 x 3 x 12 in. rectangular structure was instrumented with pressure transducers located on the upper half of one face as shown in figure 3. It was necessary to space these gages along the third dimension (width) in order to reduce the vertical spacing between gages. For the short time durations of interest and the dimensions of the shock tube and test structures, the variations in pressure at each gage location will be independent of the third dimension. Further, symmetry considerations require the measurement of pressure only on one-half of the vertical face of the test structure. Measurements were conducted on the roof and rear faces by rotating the test structure in the manner suggested by figure 6. However, pressure measurements were made only at two upper locations on the rear face of the model since the proximity of the lower locations to the model support plates would have yielded questionable data from reflections and flow disturbance.

A. FRONT FACE   B. ROOF - FRONT HALF   C. ROOF - REAR HALF   D. REAR
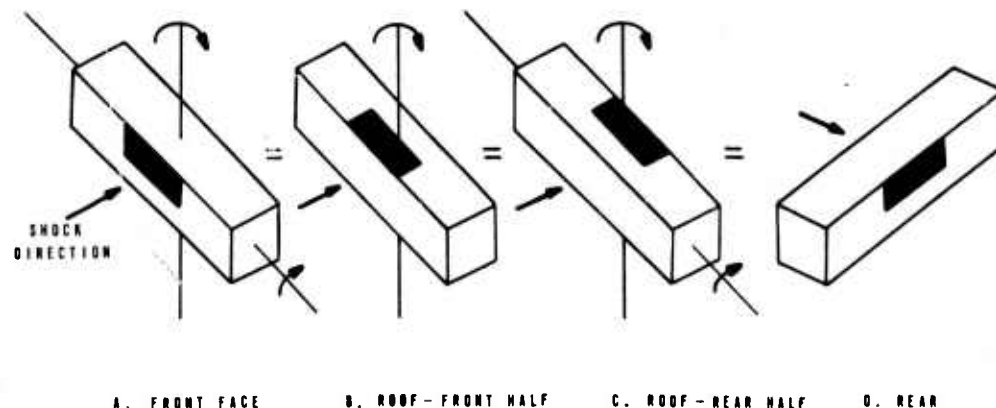
Figure 6. Rectangular Structure Rotation Sequence

The 3-in. diameter by 12-in. length cylindrical structure was instrumented with three gages at 10 degree intervals as shown in figure 4. Again, the third dimension was used to allow closer angular spacing of the gages. The cylindrical structure was designed such that the central 4 inch section could be rotated, thus providing complete pressure measurement capability around the structure. Naturally, numerous tests were necessary to provide complete data acquisition around both structures.

Symmetry considerations allow the top half of the cylindrical structure to be viewed as an arch lying on a planar surface when boundary layer effects are neglected. For this reason, the cylindrical structure will be referred to as an arch throughout the remainder of this report.

All test structures were supported across the center of the shock tube by a backup plate which was bolted to either side of the shock tube wall. This plate also served to conduct the gage cables from the test structure to the outside of the shock tube. The support spacers shown in figures 3 and 4 were replaced with the roof extensions when these tests were conducted.

4. INSTRUMENTATION

Model ST4 and ST4A pressure transducers manufactured by Susquehanna Instruments were used to measure incident, stagnation, and on-structure pressure loadings. These gages differ only in that the ST4 gage is designed for a threaded receptacle whereas the ST4A is not (see figure 7). The manufacturer's specifications for these gages are presented in appendix A. These gages are miniature piezoelectric bar type pressure transducers which have been found to be suitable gages for high pressure shock tube experimentation. The ST4 and ST4A gages have a high frequency response with low acceleration sensitivity and low cross-axis sensitivity.

At the higher 300 psi test level the gages had to be protected against the temperatures associated with the high reflected pressures and gas combustion products. This protection was provided by a layer of Scotch electrical tape covered with a thin layer of silicone lubricant as an ablative material.

Initial data recording of these gages was accomplished with Kistler charge amplifiers, Models 503 and 568, and Tektronix 555 oscilloscopes using 1A6 preamplifiers and recorded on Polaroid film.

Calibration of the pressure transducers was accomplished with the use of a specially modified hydraulic dead weight tester. This device was capable of providing step pulses of fixed magnitude. Each gage was calibrated at various pressure levels and sensitivity settings. The resulting calibration curves were used to convert the Polaroid recordings of oscilloscope traces to final engineering units. Periodic recalibration was performed during the testing phase to detect any changes in gage response characteristics. If and when detected, the new calibration curve was used.
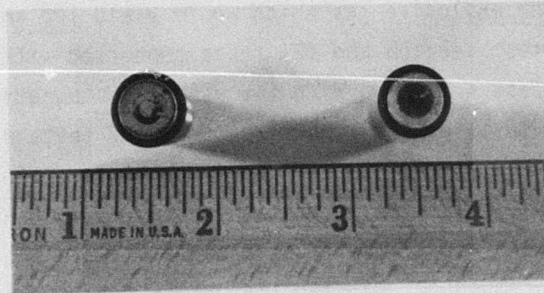
(a) Face View
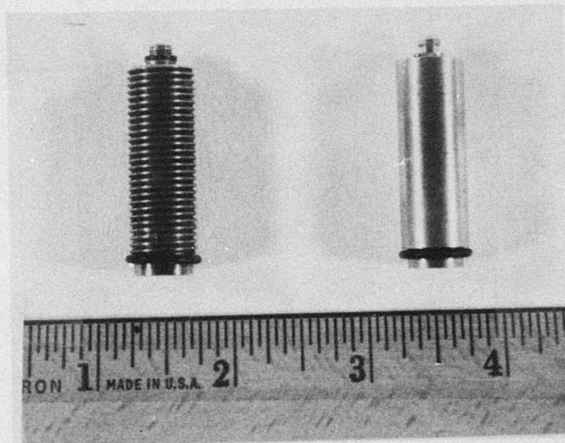
(b) Side View

Figure 7. ST4 and ST4A Pressure Transducers

5.   TEST SEQUENCE

A complete list of all tests conducted during this investigation is provided in appendix B.   Included in this list are the ambient pressures and temperatures recorded prior to each test.   In general, the test sequence consisted of (1) preliminary tests with no structure present to determine the correct amounts and mixture for the explosive gas which would yield 100 and 300 psi incident pressures at the test section and (2) tests conducted with a fully instrumented structure in the test section.   With the use of a stagnation probe mounted in the center of the test section, the first group of tests also provided information on reflected and stagnation pressures on the face of the probe at varying incident pressure levels.   The stagnation probe was in the shape of a frustum of a right cone.   The tip of the frustum had a diameter only slightly larger than the pressure transducer mounted there (see figure 7).

SECTION III

DATA REDUCTION

Thorough interpretation of test data often requires an understanding of how the raw experimental data were treated during conversion to final computer produced plots. This section presents a general description of the process used to convert the raw data to engineering units.

1. OPTICAL - TO - DIGITAL CONVERSION

All gage response data, including calibrations, were initially recorded as oscilloscope traces on Polaroid film. These traces were then reduced from optical form to digital data with a Universal Telereader in the following manner. The oscilloscope traces were electronically converted to digital records as the operator of this device manually followed each trace with moveable crosshairs. The output from this device in counts goes to an X and Y accumulator which then transfers the data to a summary card punch. A calibration for each trace was obtained by recording the X and Y coordinates of diagonal points on an indicated 4 x 4 -cm grid on the Polaroid. During all optical reduction, a 10 power magnification was used resulting in a resolution of approximately 400 counts/cm where the data traces were confined to a minimum 5 x 10 -cm grid area. The resulting punched card output was then stored on magnetic tape in card image format.

2. DIGITAL - TO - ENGINEERINGS UNITS CONVERSION

Before the test data could be converted to standard engineering units of pressure and time, it was necessary to generate calibration values for each pressure transducer. This was accomplished by converting the digital analog of the calibration oscilloscope traces to units of time and deflection based on the oscilloscope grid scale and the prescribed time scale for each calibration. A typical time duration for each calibration pulse was four seconds. Each pressure time curve was then numerically integrated. The value of this integral just prior to pressure relief was then divided by the time duration to provide an average deflection or amplitude. The deflection values thus generated and the known calibration pressure levels were then used to provide pressure versus deflection calibration curves for each transducer. All data conversion, integration, and plotting were performed by a computer.

21

After the calibration curves were generated, it was then possible to convert the test data from digital format to units of pressure and time. The computer program developed for this data reduction first converted the digital data to deflection versus time coordinates and then used the linear segmented calibration curves to convert to units of pressure versus time.

The label appearing on each individual data plot is used to identify the plot according to the designation system described by figure 8. The exception to this system is the identifying label used for the stagnation probe tests. The following system was used for these tests:

$$1 - STAG. \ PROBE - INC * 296$$

or

$$1 - STAG. \ PROBE - FF \ * 297$$

where the "1" represents the test number, INC represents an incident pressure measurement, FF represents a measurement on the probe tip, and the last characters represent the measurement number.

3. COMPOSITE DATA CONSTRUCTION

When two or more measurements were made at similar locations and under similar conditions, composite data records were constructed by averaging the similar measurements. Similar measurements were averaged only when there were no major discrepancies in waveform or magnitude between measurements. The composite record identification system used for these traces is the same as for the individual measurements with the exception that all measurement numbers used to generate the composite are listed.

MEASUREMENT NUMBER

184

GAGE LOCATION

RECTANGULAR STRUCTURE

11F - 11/8-in. from Top Edge of Front Face

11T - 11/8-in. from Leading Edge of Top Face

05B - 5/8-in. from Top Edge of Back Face

ARCH STRUCTURE

010 - 10 Degrees Measured from the Front Horizontal

WEDGE EXTENSION - BOTH STRUCTURES

1.0H* - One Structure Height (Radius) in Front of Structure along the Simulated Ground Plane

0.5H - One-Half Structure Height (Radius) in Front of Structure along the Simulated Ground Plane

STAG - Gage Located on the Structure at the Intersection of the Ground Plane and Structure

*The symbol R is used for the Arch Structure

ALL STRUCTURES

INC - Incident Pressure Measurements

11F

STRUCTURE CONFIGURATION

SR - Simple Rectangle

SA - Simple Arch

ER - Extended Rectangle

EA - Extended Arch

WR - Rectangle With Wedge Extension

WA - Arch With Wedge Extension

SR

INCIDENT PRESSURE LEVEL (NOMINAL)

100 - 100 PSI

300 - 300 PSI

100

Figure 8. Measurement Designation System for Individual Plots

23

SECTION IV

EXPERIMENTAL DATA

1. INTRODUCTION

The objective of this section is to provide characteristic descriptions of the test data in a condensed format. The stagnation probe data are presented primarily as reflection factors and drag coefficients as functions of incident overpressure level. Test data from the simple structural shapes are shown in the form of pressure variations as a function of time and position. Local reflection factors and drag coefficients are also presented. The data from the extended model tests are provided as overlays on the pressure-time histories recorded at similar locations on the basic structural shapes without extensions. And, finally, the simulated ground plane test data are presented as reflected wave attenuation curves.

More specific information in the form of individual pressure-time histories are presented in appendix C for all measurements conducted during this effort. Appendix C also contains composite pressure-time histories constructed from similar measurements. These composites were used in the following data presentation when possible.

2. STAGNATION PROBE TESTS

As stated earlier, preliminary tests were conducted using varying amounts and ratios of oxygen and hydrogen. The objective of these tests was to identify the correct gas mixtures which would yield the desired 100 and 300 psi incident pressure levels. Table 1 provides a tabulation of incident pressures and resulting reflected and stagnation pressures measured during these tests. Included in this tabulation are the shock front velocities which were measured with trigger gages located upstream from the shock tube test section. A comparison of the measured incident pressures and incident pressures derived theoretically from the measured shock front velocities is also provided in table 1. This comparison demonstrates reasonable agreement between the two quantities and indicates that within this range of pressures, free stream shock characteristics do not vary significantly from ideal behavior. In fact the primary source of variation may easily be attributed to experimental errors in measuring pressure and shock velocity.

Table 1

STAGNATION PROBE MEASUREMENTS

INCIDENT PRESSURE (psi)	REFLECTED PRESSURE (psi)	STAGNATION PRESSURE (psi)	SHOCK FRONT VELOCITY (fps)	CALCULATED INCIDENT PRESSURE (psi)
94	450	230	3144	93
95	465	237	3164	94
100	510	275	3175	95
104	570	310	*	
104	585	280	3156	94
104	650	375	3220	99
106	530	290	3169	95
107	675	350	3214	98
110	650	350	3223	99
113	650	350	3227	99
135	745	390	3759	138
153	950	550	3929	154
158	920	460	3935	152
161	980	465	3967	154
224	1590	925	4638	220
300	2140	1250	5273	287
330	2350	1400	*	

*Quantity Not Measured.

The data collected during these tests can be used to determine reflection factors and drag coefficients for a range of incident pressure levels. The values would be applicable to frontal loads on a disc shaped plane oriented normal to the direction of shock propagation. The reflection factors may be calculated simply as follows:

$$RF = \frac{P_{RO}}{P_{SO}}$$

where

$$RF = \text{Reflection Factor}$$

$$P_{RO} = \text{Reflected Pressure}$$

$$P_{SO} = \text{Incident Overpressure}$$

The drag coefficients require a knowledge of the density (ρ) and flow velocity (u) behind the shock front. Neither of these quantities were measured in the experiments. However, ρ and u may be calculated from the measured incident pressures and ambient shock tube conditions as follows:

$$u = \frac{5P_{so}}{7P_o} \left[\frac{C_o}{(1 + 6P_{so}/7P_o)^{1/2}} \right]$$

$$\rho = \rho_o \left[\frac{7 + 6P_{so}/P_o}{7 + P_{so}/P_o} \right]$$

where

$$C_o = \text{Ambient Speed of Sound}$$

$$\rho_o = \text{Ambient Density of Unshocked Gas}$$

The above relationships are for an ideal gas with constant specific heats. However, within the range of pressures investigated there is negligible difference in flow velocity when air is considered an ideal gas or a nonideal gas (reference 2) and the variation in density of the shocked gas amounts to less than 10 percent at 300 psi under ideal and nonideal considerations.

26

With values of ρ and u determined as above, the dynamic pressure may be calculated as $q_0 = 1/2 \rho u^2$. The difference between measured quasi-steady pressure and incident overpressure is commonly defined as drag pressure. For the stagnation probe tests, this quasi-steady pressure is the same as the stagnation pressure. The experimental drag coefficients were then determined as the ratio between drag pressure and dynamic pressure.

Reflection factors and drag coefficients determined from the preceding relationships are presented in table 2. Figure 9 shows reflection factors as a function of incident overpressure level and figure 10 displays similar information for drag coefficients. Both sets of data are weighted heavily by the larger number of lower pressure level measurements. Figure 9 shows the expected increase in reflection factors with increasing overpressure level while figure 10 shows a smaller increase in drag coefficients. A disturbing observation is the relatively larger scatter in data shown in figure 10 when compared to the reflection factor data of figure 9.
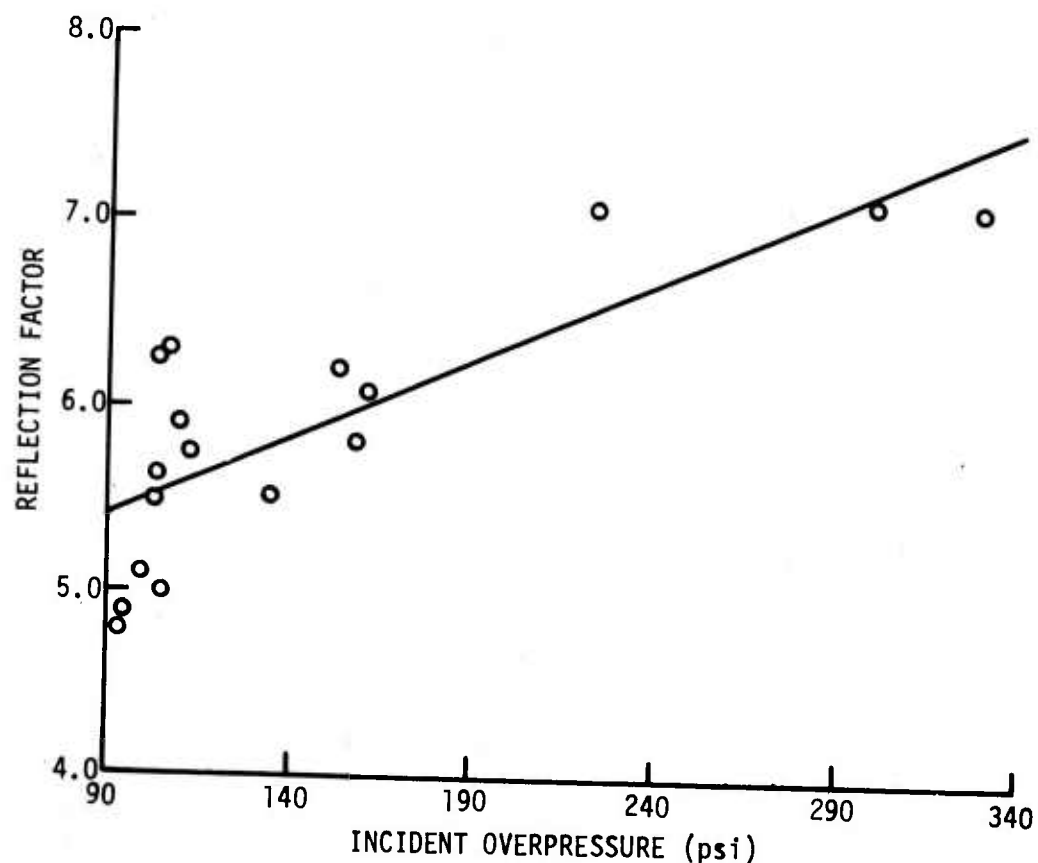
Figure 9. Stagnation Probe Tests Reflection Factors

Table 2

STAGNATION PROBE REFLECTION FACTORS AND DRAG COEFFICIENTS

INCIDENT PRESSURE (psi)	REFLECTION FACTOR (RF)	DRAG COEFFICIENT (C_d)
94	4.79	1.12
95	4.89	1.16
100	5.1	1.32
104	5.48	1.46
104	5.63	1.25
104	6.25	1.93
106	5.00	1.27
107	6.31	1.66
110	5.91	1.57
113	5.75	1.49
135	5.52	1.25
153	6.21	1.64
158	5.82	1.20
161	6.09	1.17
224	7.10	1.76
300	7.13	1.66
330	7.12	1.66
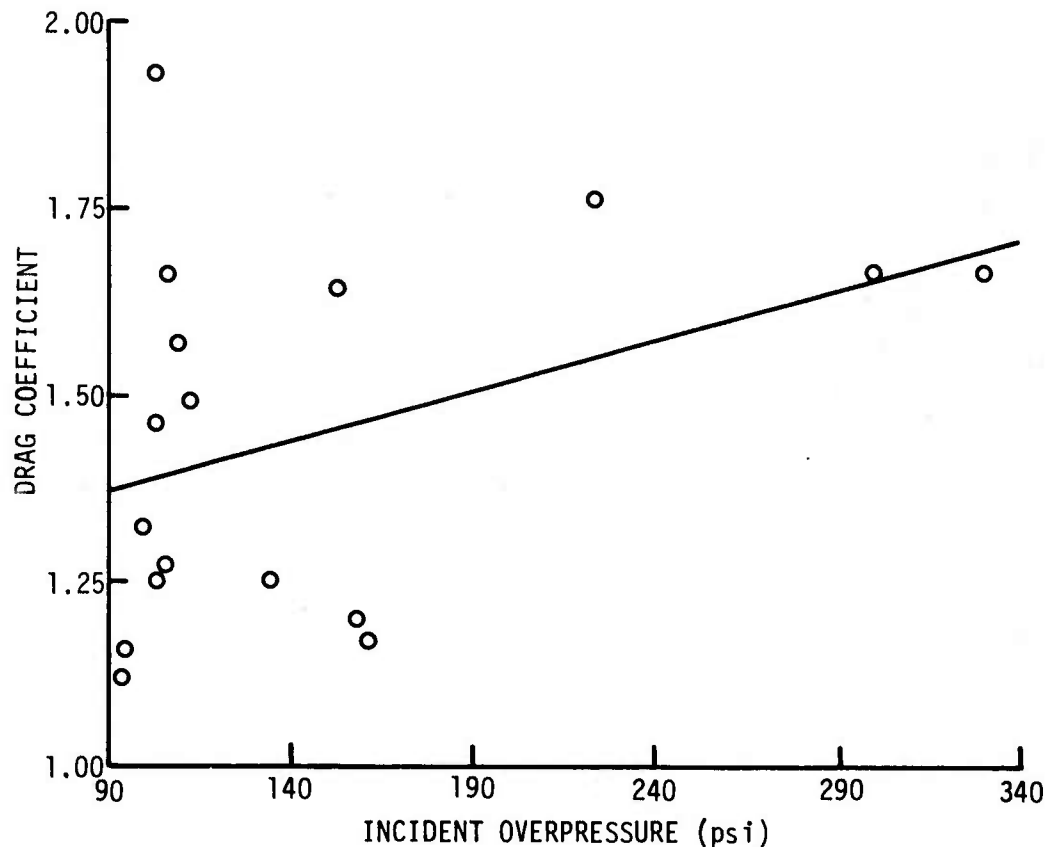
Figure 10. Stagnation Probe Tests Drag Coefficients

3. STRUCTURAL MODEL TESTS

The experimental data gathered during the structural model tests are pre-sented in three separate subsections. These subsections consist of the basic structural shapes, the extended roof models, and the models with wedge exten-sions (ground planes). Each of these subsections is further divided into the data associated with the arch and data associated with the rectangle.

a. Basic Structural Shapes

(1) Simple Arch

General descriptions of pressure loading around the arch structure at nominal 100 and 300 psi incident pressure levels are presented in figures 11 and 12. These figures show the pressure distributions at 12.5 μsec intervals between 0 and 400 μsec for the 100 psi level and between 0 and 300 μsec for the 300 psi level. Inspection of these figures provides a description of the basic phenomena associated with shock diffraction. First, envelopment of the

29
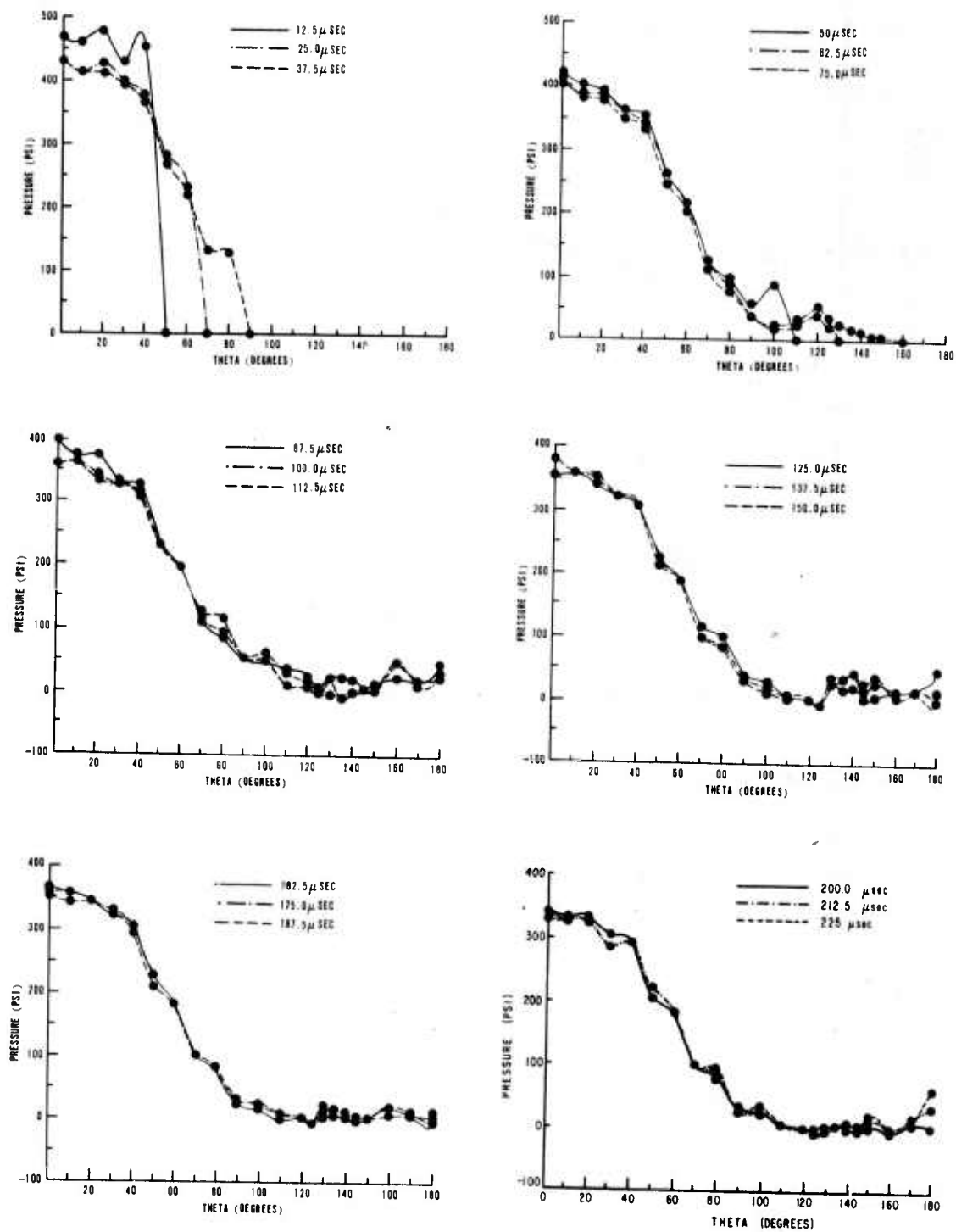
Figure 11. 100 Psi Overpressure Load Distribution - Arch Structure
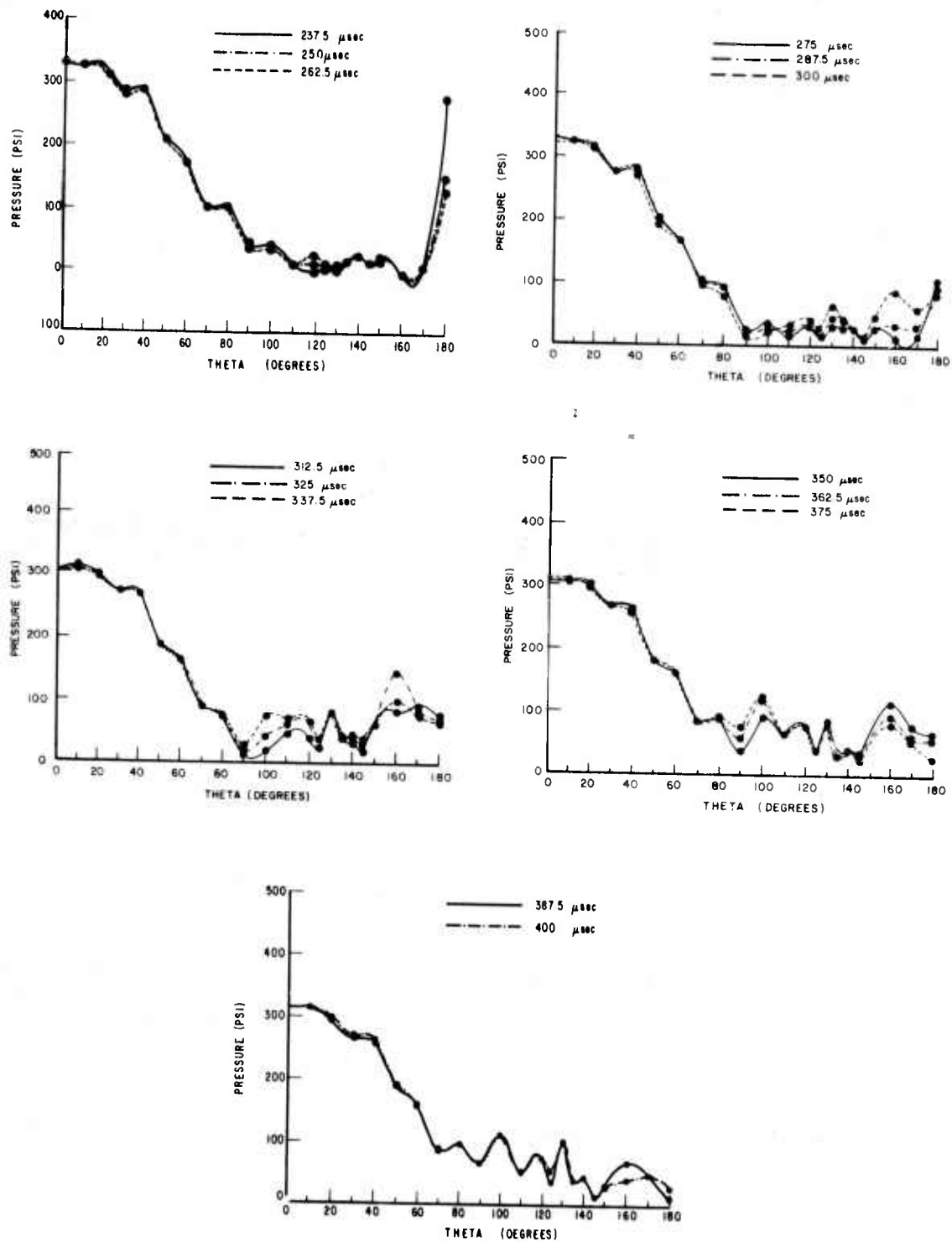
Figure 11.   100 Psi Overpressure Load Distribution -
Arch Structure (Continued)
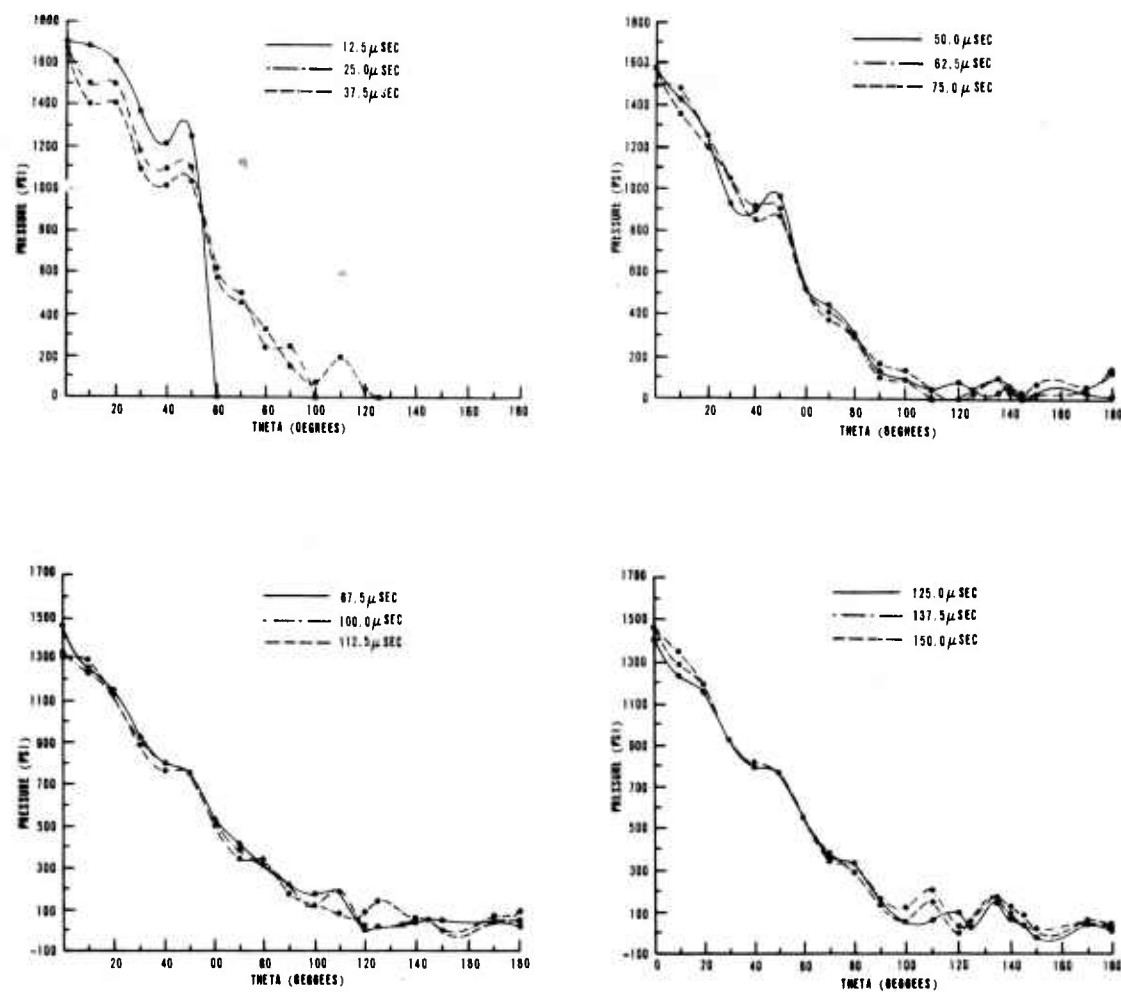
Figure 12.   300 Psi Overpressure Load Distribution - Arch Structure
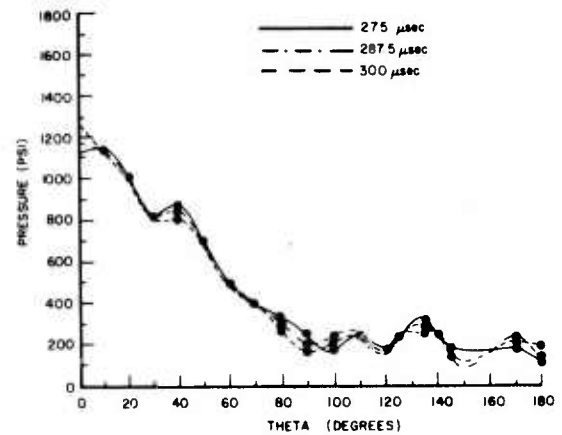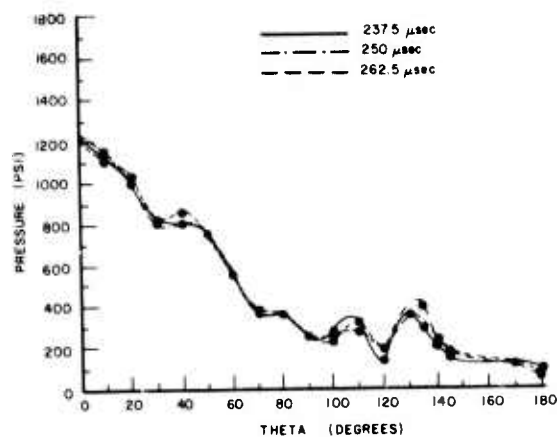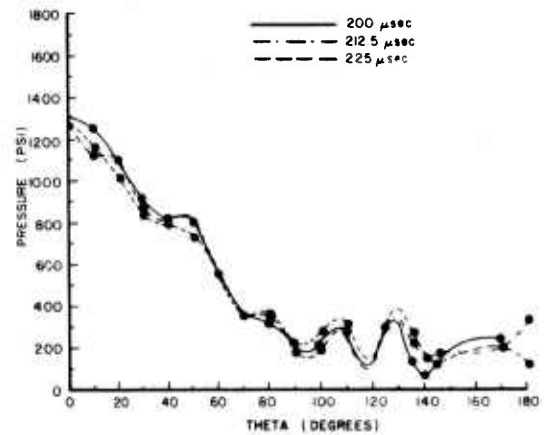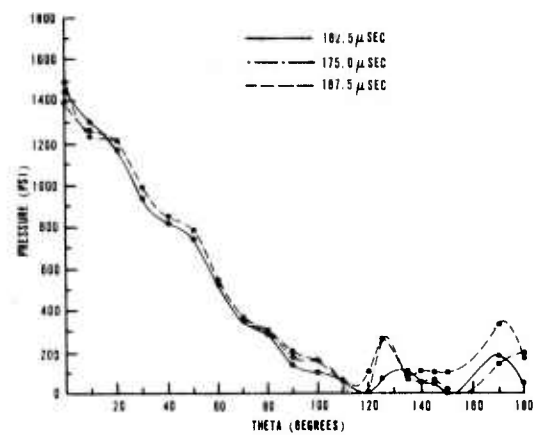
Figure 12.   300 Psi Overpressure Load Distribution -
Arch Structure (Continued)

structure by the incident shock wave is seen to result in subsequently higher pressures on the upstream face from reflection behavior. As time progresses, the reflected pressure levels are eventually reduced to a quasi-steady level by rarefaction waves. The resulting pressures on the windward face are then composed of the combined action of overpressure and a positive dynamic pressure effect (drag loading). Both the reflected pressure levels and the later quasi-steady pressure levels are seen to decrease at higher angles of incidence.

The rear face locations show that the initial pressure levels are generally lower than the incident overpressure. This decrease results from the expansion of the incident pressure wave into the rear region of the structure. After the initial passage, the pressure levels continue to be less than the incident overpressure. However, the reduction is now caused by the action of vortices which follow the initial wave and are generated as the shocked gas flow deflects around the crown of the structure. These vortices generate extremely complex, dynamic loading behavior during the first half of the diffraction process, but eventually form somewhat stable high and low pressure regions on the rear face. The loading throughout this period of time is composed of the shock wave overpressure and again a dynamic pressure effect. However, in this situation the dynamic pressure results in a negative drag effect due to the direction of the flow field which is additionally disturbed by the localized vortices. The "valleys" displayed on the curves suggest the location and number of vortices acting at any one time. In the later stages of the diffraction process the number and magnitude of these vortices tend to stabilize, but not disappear. A comparison between the 100 psi and 300 psi data indicates that the lower pressure level is subject to a larger number of localized vortices than the higher pressure level.

Tables 3 and 4 provide a list of initial peak pressures, steady state pressures, and time lapses between initial peak load and the steady state load. Also included in these tables are the measured incident pressures, measured shock front velocities, and incident pressures calculated from the shock front velocities. Again, the latter quantities are provided as a measurement check. Since each test on the arch structure included three different on-structure measurements (different locations), the measured shock front velocity and calculated incident pressure are listed only once for each group of measurements common to any one test.

34

Table 3

ARCH STRUCTURE MEASUREMENTS-100 PSI OVERPRESSURE

POSITION (DEGREES)	INCIDENT PRESSURE (PSI)	INITIAL PEAK PRESSURE (PSI)	STEADY STATE PRESSURE (PSI)	TIME LAPSE (µsec)	SHOCK FRONT VELOCITY (FPS)	CALCULATED INCIDENT PRESSURE (PSI)
0	109	525	300	320	3217	99
	109	607	323	320	3224	99
10	109	500	320	320		
	109	550	305	320	3213	99
	109	555	310	320		
	109	630	341	320		
20	109	467	295	310		
	109	560	313	300		
30	109	438	285	330		
	110	440	260	300	3196	99
40	110	485	260	300		
50	110	304	198	310	3190	98
	110	310	199	290		
60	105	240	175	290	3238	100
70	105	155	100	270		
	110	131	90	245	*	
	110	163	80	260	3206	98
	112	153	90	280	3221	99
80	108	105	70	240		
	110	130	60	220		
	110	125	75	175		
90	108	80	40	140		
	110	67	40	180		
	110	88	60	185	3220	99
	110	105	70	160		
100	105	87	80	285		
	110	80	90	305		
110	110	45	50	260		
120	110	52	70	145	3199	98
125	108	34	50	215	3197	93
130	110	35	90	235		
135	108	25	40	215		
140	110	50	50	255		
150	108	30	30	245		
160	108	37	60	235	3194	97
170	108	50	60	215	3208	98
	103	20	75	155		
	108	20	75	155		
	103	20	55	140		
180	103	35	35	100		

* Quantity Not Measured

Table 4

ARCH STRUCTURE MEASUREMENTS-300 PSI OVERPRESSURE

POSITION (DEGREES)	INCIDENT PRESSURE (PSI)	INITIAL PEAK PRESSURE (PSI)	STEADY STATE PRESSURE (PSI)	TIME LAPSE (μsec)	SHOCK FRONT VELOCITY (FPS)	CALCULATED INCIDENT PRESSURE (PSI)
0	319	2100	1250	220	5525	319
10	303	1740	1050	220	6006+	376.7
	319	1950	1125	170		
	319	1825	1300	200		
20	284+	2150	1050	220	*	
	303	1750	1000	220		
30	284+	1670	275	190		
	303	1620	825	200		
40	284+	1395	760	170		
	315	1575	800	120	*	
50	315	1480	750	120		
60	315	830	650	85		
70	305	500	395	90	*	
	311	690	355	85	5618	329
80	330	360	310	40	*	
	305	345	345	0		
	293	355	355	0		
90	330	325	340	0		
	293	290	200	7		
100	330	250	250	0		
110	300	225	250	162	5115	269
120	300	125	125	160		
125	333	125	260	125		
135	333	100	300	175	*	
140	283	100	200	165	5005	257
145	333	37	200	160		
150	283	43	100	190		
170	340	40	200	120	5495	315
	293	150	250	130	*	
	340	90	225	100		
180	340	250	225	107		
	293	100	125	110		

+ Questionable Measurement
* Not Recorded

On the upstream face of the simple arch structure (locations less than 90 degrees), the initial peak pressure values in tables 3 and 4 may be interpreted as reflected pressure levels. At values greater than 90 degrees, the same column of values represent the pressure levels of the initial wave passage which has been reduced below the upstream incident overpressure level because of the expansion of the incident shock as it deflects around the rear face. The pressure-time waveforms became increasingly complex on the downstream face of the test structure and quite often failed to stabilize into what might be identified as a true steady state pressure level. For this reason some of the indicated steady state pressures listed in tables 3 and 4 at angles of incidence greater than 90 degrees represent average pressure levels over a late time interval.

The dynamic nature of the structural loading requires that the time lapse between the initial loading and the development of steady state loading becomes an important parameter in the description of the diffraction process. The time lapse values specified in tables 3 and 4 represent one of two things depending on the location of the measurement. In general, for locations on the front face of the structure, the time lapse values indicate the time required to reduce the initial peak reflected pressure to the steady state level by the action of rarefaction waves. At higher angles of incidence the time lapse values represent an approximate time required for the lower initial peak pressure to rise to the average steady state level. The time lapses represent the combined effect of the expansion process of the upstream incident overpressure into the rear region of the structure and the stabilization of vortex behavior on the rear face.

Initial peak pressure ratios and drag coefficients were determined from the data in tables 3 and 4 and are presented in tables 5 and 6. The initial peak pressure ratios are defined as the peak initial pressure measurements divided by the incident overpressure common to that measurement. The drag coefficients were determined in the same manner as described earlier for the stagnation probe tests. The pressure ratios for values of theta less than 90 degrees represent reflection factors. Pressure ratios and drag coefficients are shown graphically in figures 13 and 14 as functions of theta. Evident in figure 13 are the two regions containing the extreme angles for Mach reflection. The angle of incidence at which the two possible angles of reflection based on theory are equal is termed the extreme angle. Mach reflection occurs when the

Table 5

ARCH STRUCTURE PRESSURE RATIOS AND DRAG COEFFICIENTS-100 PSI OVERPRESSURE

THETA (DEGREES)	INCIDENT PRESSURE (PSI)	INITIAL PEAK PRESSURE RATIO	DRAG COEFFICIENT (C_d)
0	109	4.82	1.27
	109	5.57	1.42
10	109	4.68	1.40
	109	5.05	1.30
	109	5.09	1.33
	109	5.78	1.54
20	109	4.28	1.24
	109	5.14	1.35
30	109	4.02	1.17
	110	4.00	0.98
40	110	4.41	0.98
50	110	2.76	0.57
	110	2.82	0.58
60	105	2.29	0.49
70	105	1.48	-0.03
	110	1.19	-0.13
	110	1.48	-0.20
	112	1.37	-0.16
80	108	0.97	-0.26
	110	1.18	-0.33
	110	1.14	-0.23
90	108	0.74	-0.46
	110	0.61	-0.46
	110	0.80	-0.33
	110	0.95	-0.26
100	105	0.83	-0.18
	110	0.73	-0.13
110	110	0.41	-0.39
120	110	0.47	-0.26
125	108	0.31	-0.38
130	110	0.32	-0.13
135	108	0.23	-0.46
140	110	0.45	-0.46
145	108	0.28	-0.52
150	108	0.34	-0.32
160	108	0.46	-0.32
170	103	0.19	-0.20
	108	0.19	-0.22
	103	0.19	-0.35
180	103	0.34	-0.02

38

Table 6

ARCH STRUCTURE PRESSURE RATIOS AND DRAG COEFFICIENTS-300 PSI OVERPRESSURE

THETA (DEGREES)	INCIDENT PRESSURE (PSI)	INITIAL PEAK PRESSURE RATIO	DRAG COEFFICIENT (C_d)
0	319	6.58	1.51
10	303	5.74	1.29
	319	5.72	1.59
	319	6.11	1.30
20	284*	7.57*	1.42*
	303	5.78	1.20
30	284*	5.88*	1.10*
	303	5.35	0.90
40	284*	4.91*	0.89*
	315	5.00	0.80
50	315	4.70	0.72
60	315	2.63	0.55
70	304	1.64	0.16
	311	2.22	0.07
80	330	1.09	-0.03
	305	1.13	0.07
	293	1.21	0.11
90	330	0.98	0.02
	293	0.99	-0.17
100	330	0.76	-0.12
110	300	0.75	-0.09
120	300	0.42	-0.31
	300	0.42	-0.31
125	333	0.38	-0.11
135	333	0.30	-0.05
140	283	0.35	-0.16
145	333	0.11	-0.20
150	283	0.15	-0.34
170	340	0.12	-0.21
	293	0.51	-0.08
	340	0.26	-0.17
180	340	0.74	-0.17
	293	0.34	-0.30

* Questionable Data
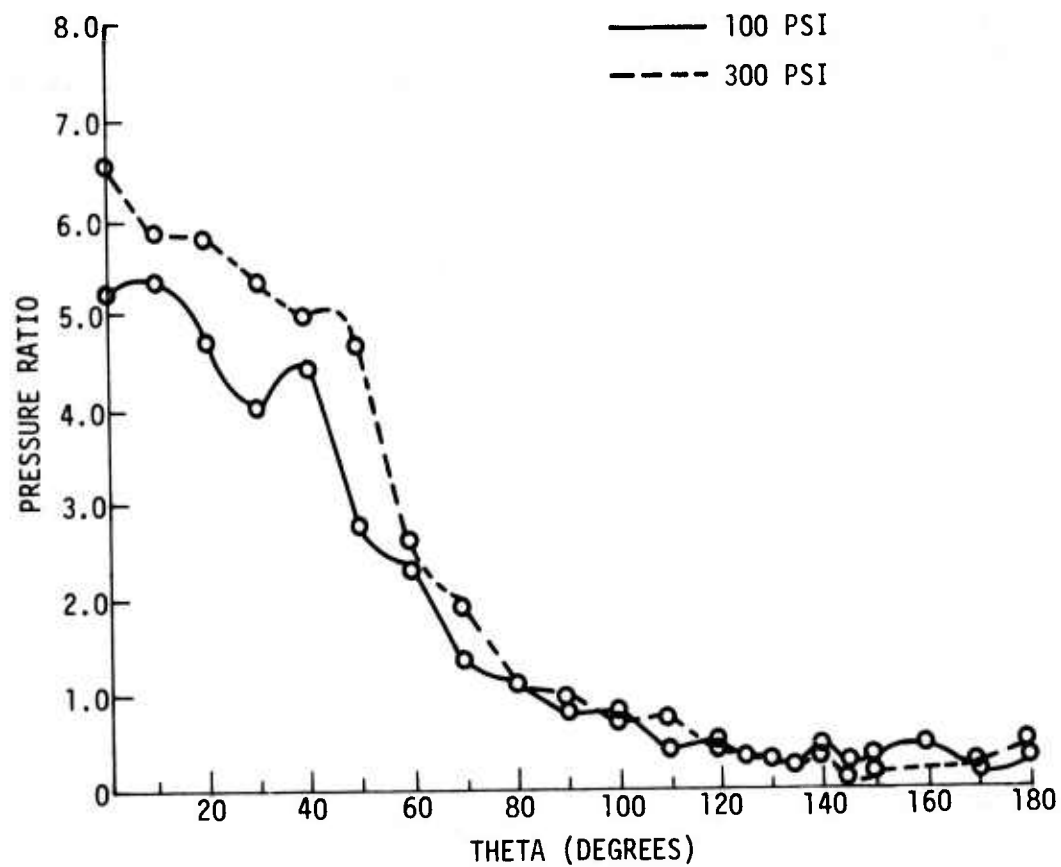
Figure 13. Initial Peak Pressure Ratios - Arch Structure
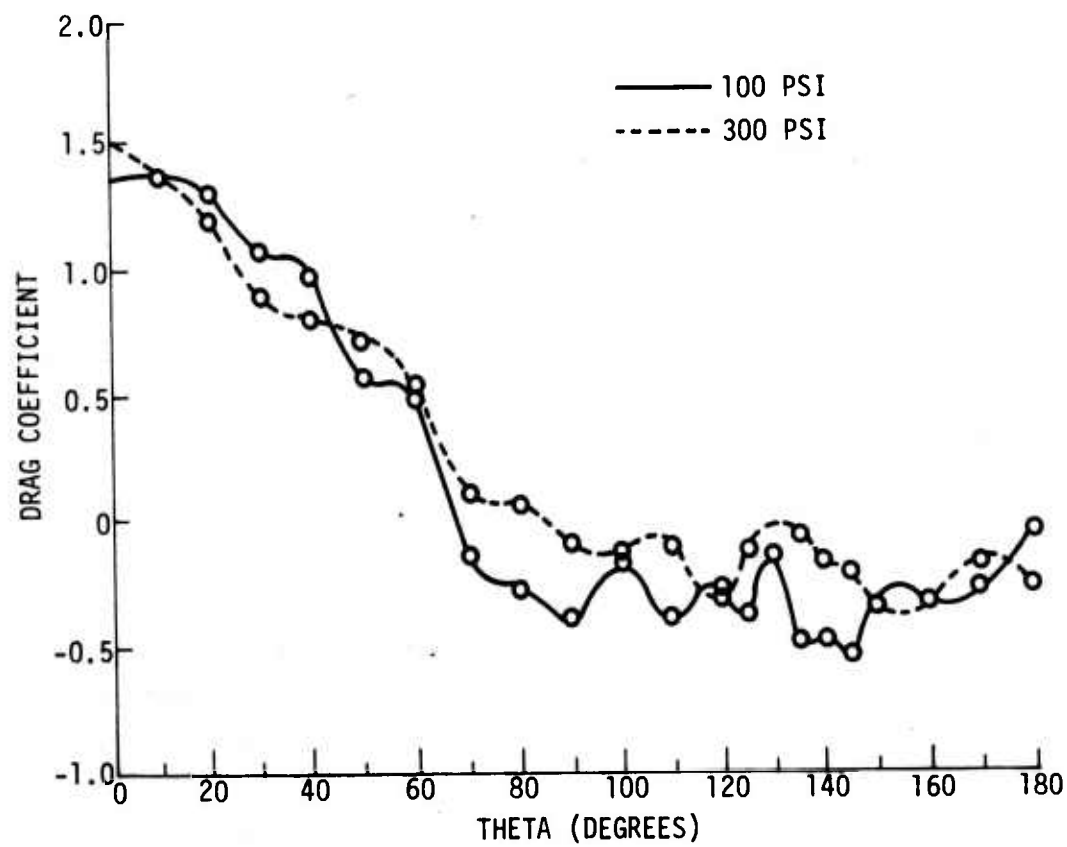
Figure 14. Drag Coefficients - Arch Structure

angle of incidence is slightly greater than the extreme angle. The 100 psi data indicate an angular region located near the 40 degree location while the 300 psi level shows a slightly greater angular position. This higher position is to be expected based on theoretical values of the extreme angle which tend to increase at higher shock strengths. However, this theoretical increase is small compared to the change indicated in figure 13. The larger change may be attributed to a combination of two factors. First and most important, the theoretical values are determined for a planar surface intersecting the shock path and second, any variations arising from experimental error may tend to exaggerate the difference.

The drag coefficients shown in figure 14 indicate little pressure level dependency at angles of incidence less than 60 degrees. At larger angles of incidence the effects of pressure level seem more pronounced with slightly higher values of drag coefficients indicated for the 300 psi level. The data at larger angles of incidence also indicate different variations of drag coefficients with theta between the two pressure levels. The difference results from the number and locations of the vortices acting on the rear surface for the 100 psi tests and the 300 psi tests.

The time lapse values shown in table 3 for the 100 psi arch tests show that the period of reflected pressure relief remains essentially constant for angles of incidence between zero and 80 degrees. At 80 degrees and above, the time required to achieve steady state conditions decreases with a rapid decrease at 90 degrees. This location of decrease is to be expected because this is a region of small reflections and since this region is closest to lower free stream pressures, it is consequently closer to the origin of rarefaction waves. On the rear of the arch structure the time lapse values indicate stabilization times for the vortices acting on the rear surfaces. Again, over a certain region the time lapse values are relatively constant; the region being between 90 and 160 degrees. Below this region a significant decrease is noted. For the 300 psi data shown in table 4 the regions of essentially constant time lapse are found between 0 and 60 degrees and between 100 and 170 degrees. The remaining areas are then affected by more rapid changes. The obvious difference between the two sets of data shown in tables 3 and 4 is that time lapse values are reduced at the 300 psi level.

    (2) Simple Rectangle

In the same manner as the previous subsection, general descriptions

42

of pressure loading around the rectangular structure are presented in figures 15 and 16. These figures show pressure variations as a function of position for specified intervals in time. Somewhat different behavior characteristics are evident in these figures than were found in figures 11 and 12 for the simple arch structure. However, the five basic components of the loading phenomena-overpressure, reflections, uniform drag effects, vortex behavior, and rarefaction effects are still present.

The arrival of the incident shock wave results in high reflected pressures on the front face of the structure which is oriented normal to the direction of shock propagation. Unlike the arch structure, these reflected pressures are maintained for a finite period of time related to the location of the measurement and its distance from the top edge of the structure face which is the origin of rarefaction waves. Once these rarefaction waves arrive at a given point the reflected pressures begin to dissipate, eventually arriving at a quasi-steady pressure level composed of the overpressure and a positive drag component.

On the top surface of the structure each location is initially loaded by the incident overpressure level, but at the leading edge of the surface a vortex is generated which immediately begins to erode the overpressure. After a period of time the overpressure is completely eliminated, actually resulting in a slightly negative pressure level near the leading edge. At positions located farther downstream from the leading edge, the incident pressure level is maintained relatively constant for a period of time which increases with distance from the leading edge. After this time the overpressure level is reduced by a negative drag pressure. This observation of increasing time period of constant overpressure with distance from the leading edge suggests the propagation of some disturbance from the leading edge with a propagation velocity less than the incident wave speed. Since the constant overpressure level is generally equal to the incident shock wave overpressure, an additional suggestion is that the incident wave initially generates a uniform flow with a velocity such that the structure surface realizes negligible drag effect. At some later time the upstream disturbance arrives and alters the flow resulting in a negative drag pressure. This disturbance may well be the expansion of the vortex generated at the leading edge of the top surface. The accuracy of this statement can be determined only by experimental optical techniques. The data then indicate that once the disturbance arrives at a given point the pressure

43
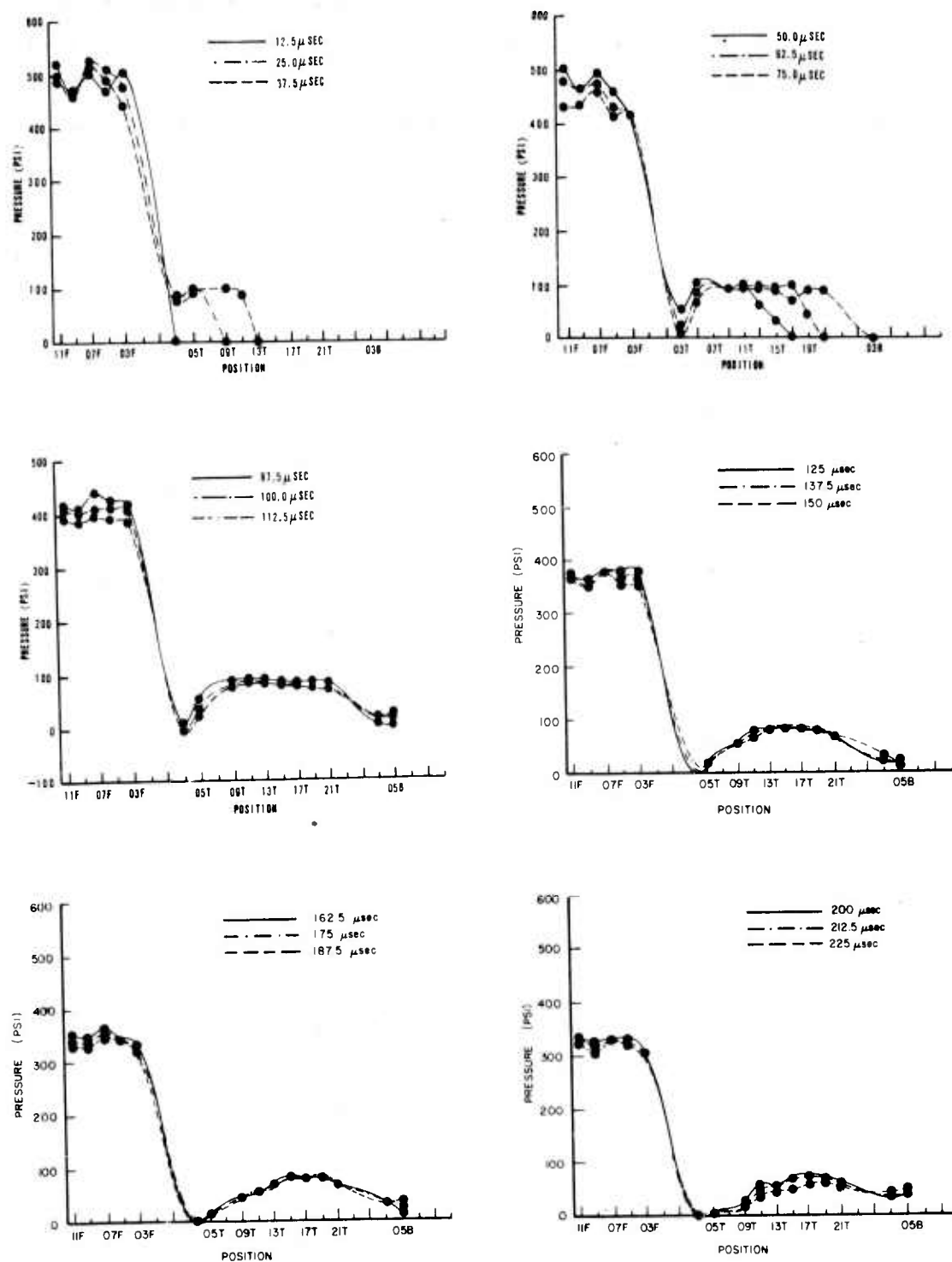
Figure 15. 100 Psi Overpressure Load Distribution - Rectangular Structure
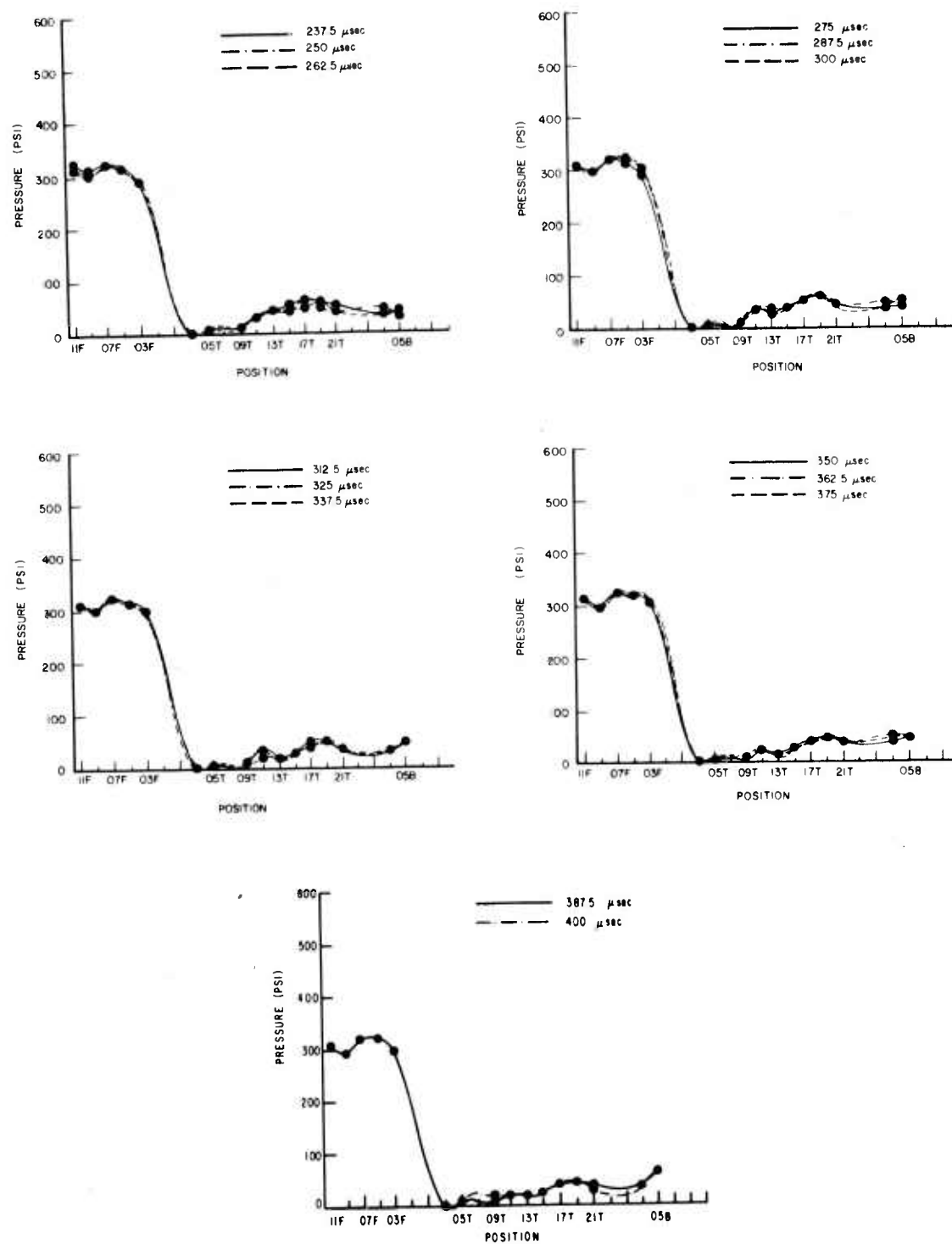
Figure 15. 100 Psi Overpressure Load Distribution -
Rectangular Structure (Continued)
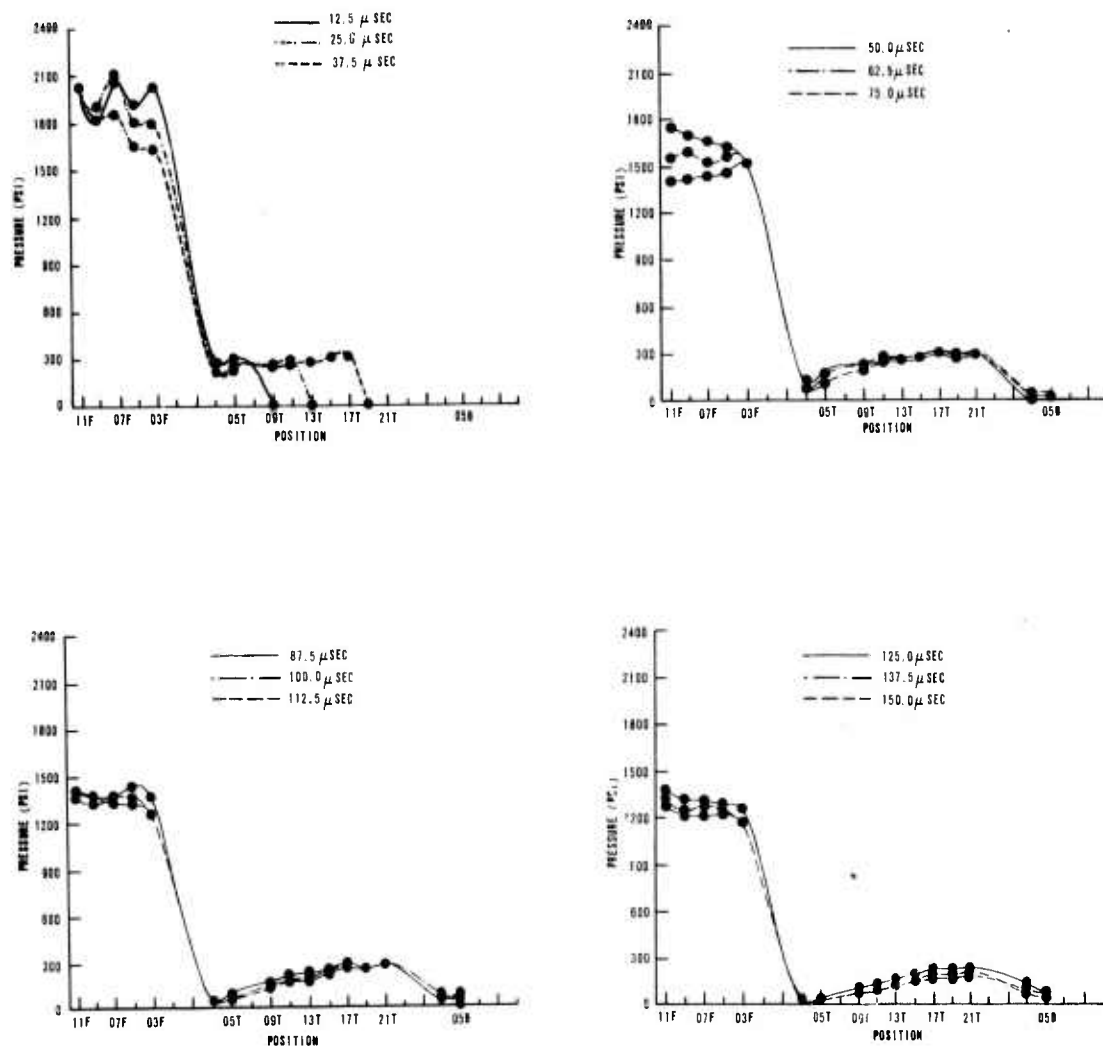
Figure 16.   300 Psi Overpressure Load Distribution - Rectangular Structure
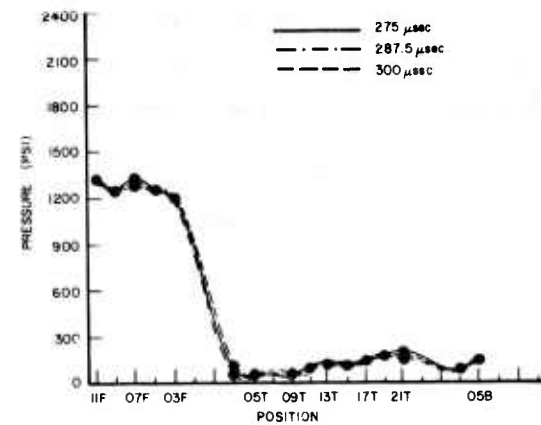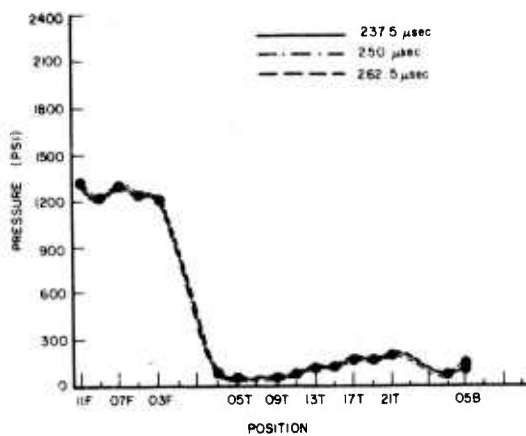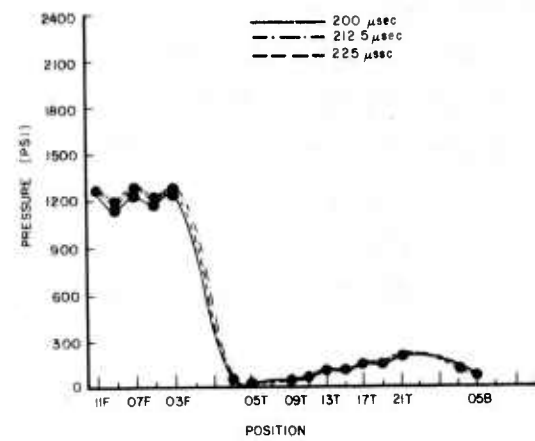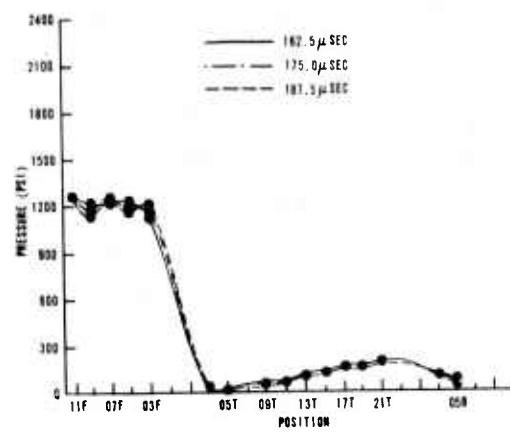
Figure 16. 300 Psi Overpressure Load Distribution - Rectangular Structure (Continued)

loading decreases to a relatively stable level.

The two measurements on the rear of the structure show that the initial loading wave is significantly reduced beneath the incident overpressure level. This reduction again results from the filling process of the incident wave and from a strong vortex generated at the top of the rear surface by the deflection of the shocked gas around the corner. At later times the loading increases abruptly as a result of reflections from the structure support plates. A similar effect would be seen for a structure lying on a flat surface or a structure in free stream conditions. For the free stream condition, a reflection would be generated when the incident waves from the top and bottom collide. Even with the reflections, the rear surface measurements show a pressure level less than the free stream overpressure as a result of the negative drag pressure.

Provided in tables 7 and 8 are the measured peak initial pressures, steady state pressures, and time lapse values as functions of position and incident pressure level. Calculated incident pressure levels derived from measured shock front velocities are also shown. These tables include steady state pressure measurements for two rear face locations. However, caution should be used since a stable pressure level was not clearly identified on the rear face locations, and further, the recorded data at later times in this area include reflected pressure effects from the structural model support plates.

The peak initial pressure values listed for front face gage locations are actually peak reflected pressure levels. All other locations indicate initial wave passage over each gage location.

Tables 9 and 10 list the initial peak pressure ratios and drag coefficients calculated from the measured data in tables 7 and 8. Average values of these pressure ratios and drag coefficients are presented graphically in figures 17 and 18 for each incident overpressure level. The increase in pressure ratios on the front face gage locations (reflection factors) with incident overpressure level is seen in figure 17 while the top surface shows the essentially undisturbed transit of the incident shock front. The rear face locations indicate little dependence on incident pressure level.

Figure 18 suggests that an increase in incident pressure level within the range investigated results in a slightly lower drag coefficient. The top and rear surfaces demonstrate a more pronounced effect with lower drag

Table 7

RECTANGULAR STRUCTURE MEASUREMENTS-100 PSI OVERPRESSURE

POSITION	INCIDENT PRESSURE (PSI)	INITAL PEAK PRESSURE (PSI)	STEADY STATE PRESSURE (PSI)	TIME LAPSE (μsec)	SHOCK FRONT VELOCITY (FPS)	CALCULATED INCIDENT PRESSURE (PSI)
11 F	94 / 103	530 / 545	203 / 318	240 / 245	* / 3241	100
09 F	94 / 103	497 / 525	288 / 305	230 / 240	*	
07 F	94 / 103	550 / 575	313 / 330	210 / 215	*	
05 F	94 / 103	496 / 565	287 / 350	215 / 185	*	
03 F	94	532	300	195	*	
03 T	99	108	-7	80	3236	100
05 T	99	105	4	140		
07 T+						
09 T	99	104	10	180		
11 T	99	100	28	230		
13 T	97 / 99	101 / 97	22 / 16	260 / 180	3175 / 3195	96 / 96
15 T	97 / 99	107 / 93	35 / 28	120 / 105		
17 T	97 / 99	98 / 110	40 / 56	280 / 140		
19 T	97 / 99	91 / 100	45 / 49	225 / 200		
21 T	97 / 99	103 / 98	44 / 36	270 / 180		
03 B	110	18	38	125	3170	97
05 B	110	18	42	100		

* Quantity Not Measured
+ Gage Malfunction

Table 8

RECTANGULAR STRUCTURE MEASUREMENTS-300 PSI OVERPRESSURE

POSITION	INCIDENT PRESSURE (PSI)	INITAL PEAK PRESSURE (PSI)	STEADY STATE PRESSURE (PSI)	TIME LAPSE (μsec)	SHOCK FRONT VELOCITY (FPS)	CALCULATED INCIDENT PRESSURE (PSI)
11 F	309	2095	1300	140	5249	285
	319	2025	1330	135	5141	288
09 F	309	2040	1130	130		
	319	1930	1260	140		
07 F	309	2200	1275	120		
	319	2100	1298	115		
05 F	309	2025	1140	105		
	319	1950	1270	130		
03 F	309	2160	1173	110		
03 T	297	335	69	45	4819	239
05 T	297	300	49	90		
07 T						
09 T	297	258	58	125		
11 T	297	282	89	90		
13 T	297	310	139	110	5222	283
	298	275	120	100	5277	287
15 T	297	317	155	160		
	298	297	103	115		
17 T	297	305	168	150		
	298	342	160	100		
19 T	297	302	175	120		
	298	309	160	120		
21 T	297	319	201	170		
	298	303	185	90		
03 B	293	35	100	65	5376	305
05 B	293	50	150	*		

+ Gage Malfunction
* Not Determined

Table 9

RECTANGULAR STRUCTURE PRESSURE RATIOS AND DRAG
COEFFICIENTS-100 PSI OVERPRESSURE

.

POSITION	INCIDENT PRESSURE (PSI)	INITIAL PEAK PRESSURE RATIO	DRAG COEFFICIENT (C_d)
11 F	94	5.64	1.72
	103	5.29	1.55
09 F	94	5.29	1.60
	103	5.10	1.46
07 F	94	5.85	1.80
	103	5.58	1.64
05 F	94	5.28	1.59
	103	5.49	1.78
03 F	94	5.66	1.70
03 T	99	1.09	-0.81
05 T	99	1.06	-0.73
09 T	99	1.05	-0.68
11 T	99	1.01	-0.54
13 T	97	1.04	-0.59
	99	0.98	-0.63
15 T	97	1.10	-0.49
	99	0.94	-0.54
17 T	97	1.01	-0.45
	99	1.11	-0.33
19 T	99	0.92	-0.38
21 T	97	1.06	-0.42
	99	0.99	-0.48
03 B	110	0.16	-0.47
05 B	110	0.16	-0.45

Table 10

RECTANGULAR STRUCTURE PRESSURE RATIOS AND DRAG
COEFFICIENTS-300 PSI OVERPRESSURE

.

POSITION	INCIDENT PRESSURE (PSI)	INITIAL PEAK PRESSURE RATIO	DRAG COEFFICIENT (C_d)
11 F	309	6.78	1.67
	319	6.35	1.64
09 F	309	6.60	1.38
	319	6.05	1.52
07 F	309	7.12	1.63
	319	6.58	1.59
05 F	309	6.55	1.40
	319	6.11	1.54
03 F	309	6.99	1.45
03 T	297	1.13	-0.40
05 T	297	1.01	-0.44
09 T	297	0.87	-0.42
11 T	297	0.95	-0.37
13 T	297	1.04	-0.28
	298	0.92	-0.31
15 T	297	1.07	-0.25
	298	1.00	-0.34
17 T	297	1.03	-0.23
	298	1.15	-0.24
19 T	297	1.02	-0.22
	298	1.04	-0.24
21 T	297	1.07	-0.17
	298	1.02	-0.20
03 B	293	0.12	-0.35
05 B	293	0.17	-0.26
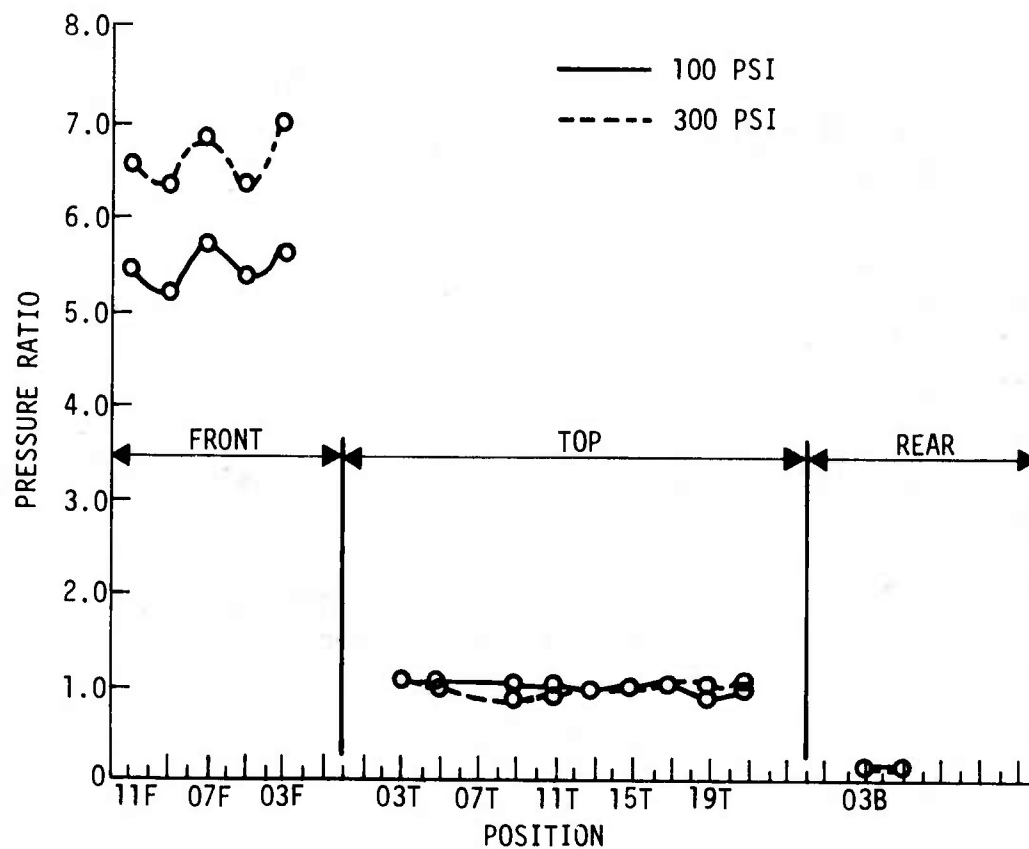
Figure 17. Initial Peak Pressure Ratios - Rectangular Structure
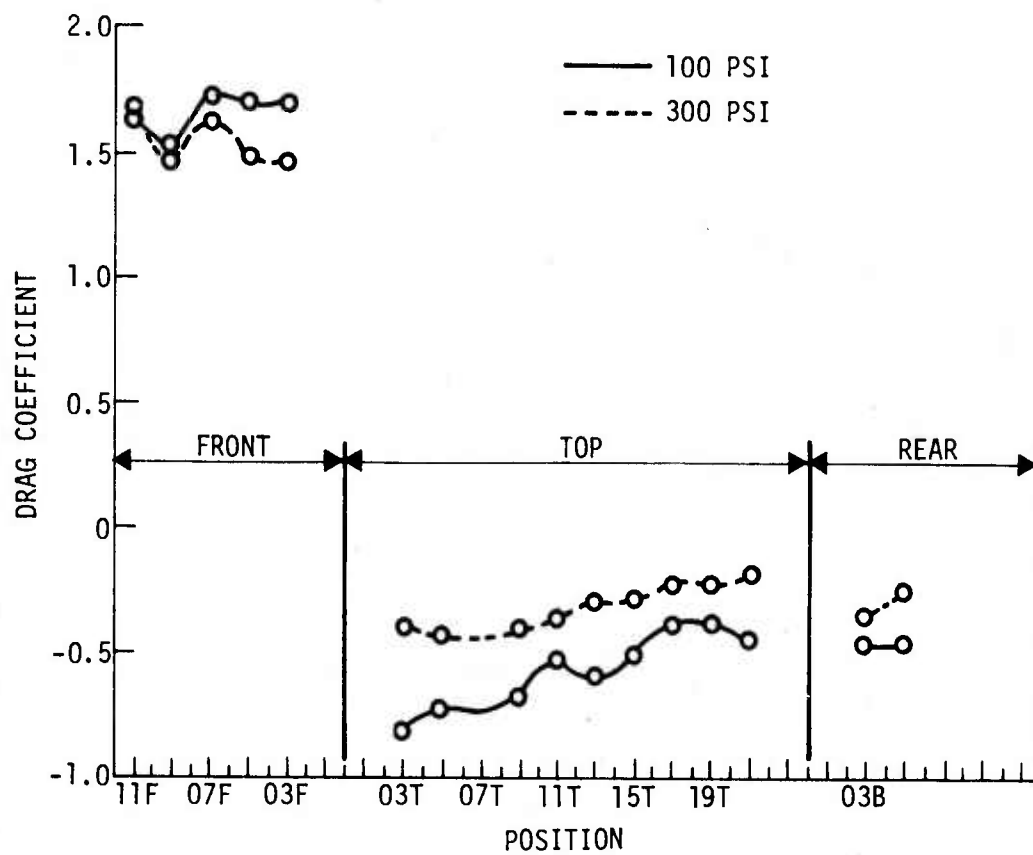
Figure 18. Drag Coefficients - Rectangular Structure

coefficients determined for the 100 psi incident overpressure level.

The time lapse values in tables 7 and 8 show increasing values on the front face with distance from the top edge. This is to be expected since the duration of the rarefaction wave increases with propagation distance. The increased duration results from the faster velocity of the rarefaction wave front compared to the propagation velocity of the tail. On the top surface locations the time lapse values generally increase with distance from the front edge and then reach a relatively constant value on the latter half of the structure surface. This trend must be related to the upstream disturbance, but the nature of the relationship was not determined. The time lapse values for the rear face measurements indicate increasing values with distance from the support plates as one might expect because the steady state pressures are pressure buildups resulting from support plate reflection and drag effects.

The pressure-time histories recorded on the rectangular structure front face were of a form similar to that shown in figure 19 where three specific time parameters are indicated.
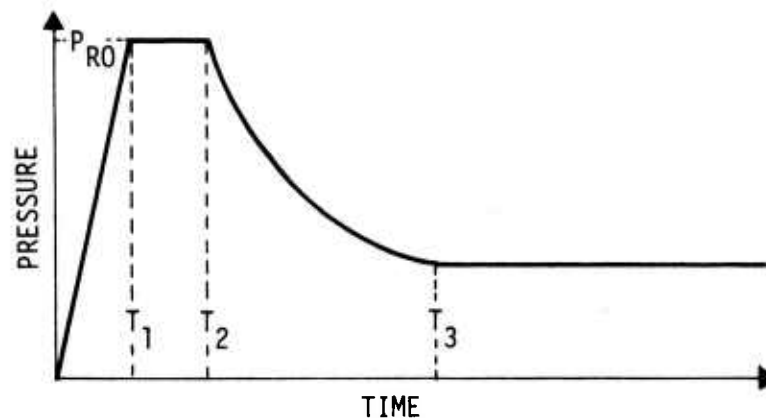
Figure 19. Typical Front Face Loading - Rectangular Structure

The value T_1 represents the rise time to peak reflected pressure P_{RO} which is equivalent to the rise time of the incident overpressure. The second time parameter, T_2, represents the time of arrival of the head of the rarefaction wave at the location of interest. The third parameter, T_3, represents the time at which the tail of the rarefaction wave passes through the point of interest resulting in a steady state pressure equal to the free stream pressure and a drag component of loading. The value of $T_3 - T_2$ will be recognized as the time lapse value discussed earlier. The peak reflected pressure duration, $T_2 - T_1$, will depend upon the distance of the point of interest from the origin of

the rarefaction wave and its wave front velocity. The relief time, $T_3 - T_2$, will then depend only on the duration of the rarefaction wave. Since the duration of the rarefaction wave will increase with propagation distance, relief time should be found to increase with distance from the origin of the rarefaction wave. For the rectangular structure, this origin is in the vicinity of the top edge. With these considerations in mind the peak reflected pressure durations ($T_2 - T_1$) and relief times ($T_3 - T_2$) at each location on the front face were determined and plotted as shown in figure 20 for each of the incident overpressure levels. These values were rounded off to the nearest five microseconds. As can be seen, a somewhat linear relationship exists between the time differences and the distance from the top of the structure front face. Additionally, the curves show increasing values with distance consistent with the previous discussion.

(a) 100 psi Overpressure

(b) 300 psi Overpressure
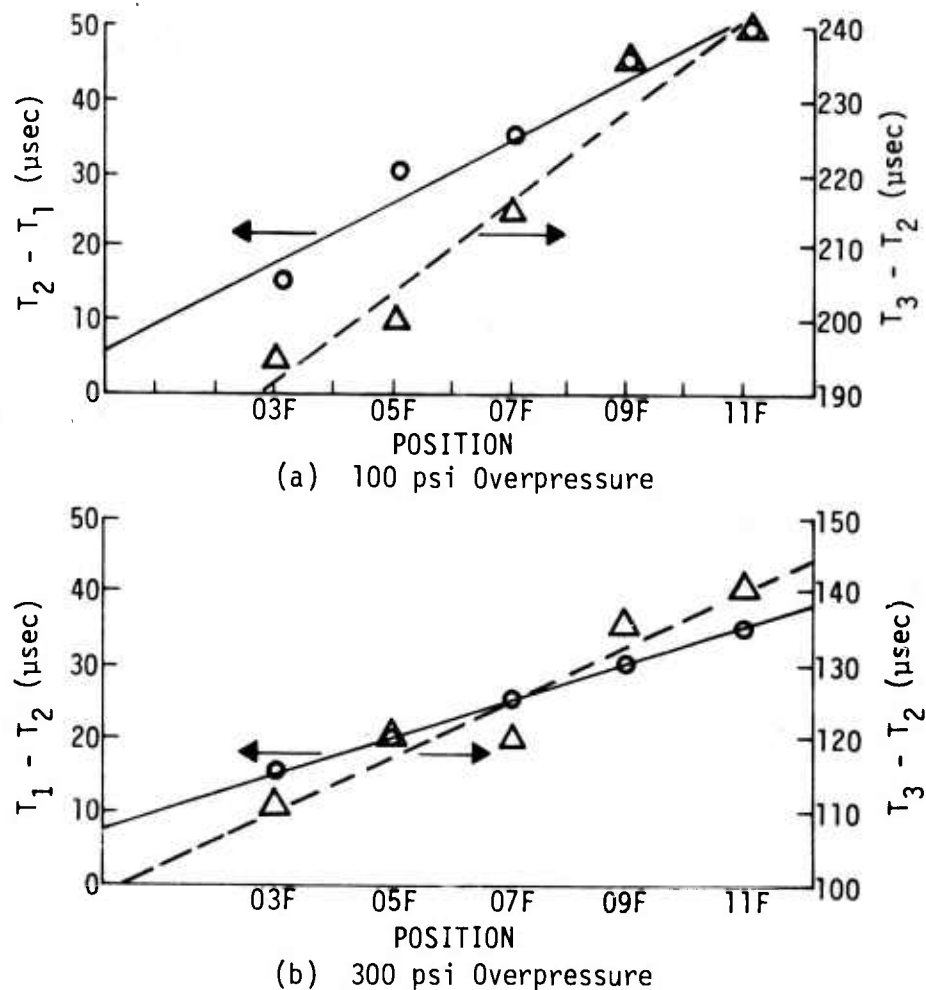
Figure 20. Peak Reflected Pressure Durations and Relief Times

Extension of the curves in figure 20 into the left vertical axis which is the location of the top edge of the structure face, results in initial values being indicated for this position. The initial value of $T_2 - T_1$, if it exists, is probably related to the expansion of reflected pressure into the adjacent region near the edge during reflected pressure buildup $(T \leq T_1)$. The primary rarefaction wave then originates at some point away from the edge defined by the zone of expansion at $T > T_1$ when increasing reflected pressures no longer occur and no longer prevent the propagation of the rarefaction wave into the zone of expansion. The initial value of $T_2 - T_1$ then describes the transit time of the rarefaction wave from its true origin to the edge of the structure face.

If the preceding hypothesized behavior with regard to $T_2 - T_1$ is correct, then the initial value will be dependent only on the shock strength of the incident overpressure while the slope of the $T_2 - T_1$ curve will be a function of the rarefaction wavefront velocity and the distance of the point of interest from the edge of the front face. An estimate of the rarefaction wavefront velocity (C_R) may be obtained from the following expression (ref. 3).

$$C_R = C_o \left\{ \left[\frac{\left(\frac{P_{so}+P_o}{P_o}\right)\left(\frac{P_{so}+P_o}{P_o} + 6\right)}{(6)\left(\frac{P_{so}+P_o}{P_o}\right)+ 1} \right] \cdot \left[\frac{\left(\frac{P_{RO}+P_o}{P_{so}+P_o}\right)\left(\frac{P_{RO}+P_o}{P_{so}+P_o} + 6\right)}{(6)\left(\frac{P_{RO}+P_o}{P_{so}+P_o}\right)+ 1} \right] \right\}^{1/2}$$

Using average values of peak reflected pressure (P_{RO}) across the front face and the measured incident overpressure, rarefaction wave velocities of 2320 ft/sec and 3720 ft/sec were determined for each of the incident overpressure levels. These values compare favorably to 2430 ft/sec and 3970 ft/sec determined from the $T_2 - T_1$ slopes in figures 20a and b respectively. The relationship between $T_2 - T_1$ and position may therefore be expressed as follows:

$$T_2 - T_1 = A + \frac{S}{C_R}$$

where A represents the initial time value at the edge location and S represents the distance of the point of interest from the edge of the structure face. For realistic structure sizes the value of A becomes inconsequential so that the

peak reflected pressure duration could be taken equal to $\frac{S}{C_R}$.

The $T_3 - T_2$ versus position curves in figure 20 for each of the overpressures show the increase in rarefaction wave duration with propagation distance. These durations may also be expressed as an initial value plus an expression in terms of the propagation distance and rarefaction wave speed. The expressions result in values of 1.41 S/C_R and 1.34 S/C_R for each of the overpressure levels investigated. Since the initial values of the $T_3 - T_2$ curves at the edge of the structure face are relatively large, these values cannot be ignored for structural dimensions considered in this investigation. However, for much larger dimensions, the importance again becomes minimal with respect to the slope equation, assuming of course that the slope equation remains valid for larger dimensions.

b. Extended Roof Models

The objective of the extended roof tests was to determine whether the front and top surface loadings would be independent of the downstream extensions. The approach taken to satisfy this objective was to measure surface loadings at the 70, 80, and 90 degree locations on the arch structure and at the 13T, 15T, 17T, 19T, and 21T locations on the rectangular structure; both structures had the roof extensions in place. These measurements were then compared to earlier measurements taken without the extensions, but at similar gage locations. These comparisons are presented in the following subsections.

(1) Extended Arch

Comparisons of the pressure-time histories recorded for the simple arch structure (SA) and the extended arch structure (EA) are presented in figures 21 and 22. Figures 21 a, b, and c show the 100 psi incident overpressure measurements at the 70, 80, and 90 degree locations respectively. The comparison presented for the 70 degree location supports the contention of no effect due to downstream extensions. However, the 80 and 90 degree locations indicate otherwise, showing a more stable waveform for the extended models. Obviously, the initial difference in magnitudes shown in figures 21 b and 21 c can result only from differences in gage sensitivity, but this sensitivity difference would result in consistent magnitude differences throughout the period of recording and the waveforms would be similar. The contradiction shown by the dissimilarity in waveforms suggests that the downstream extensions do affect the pressure loadings in areas of proximity to the extension.
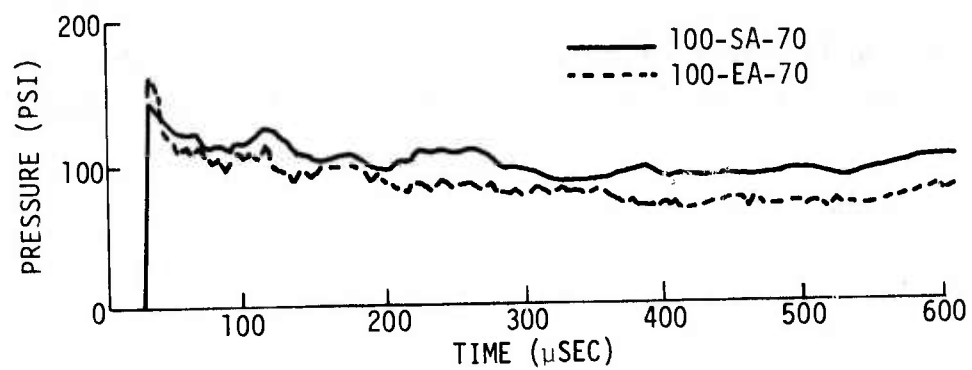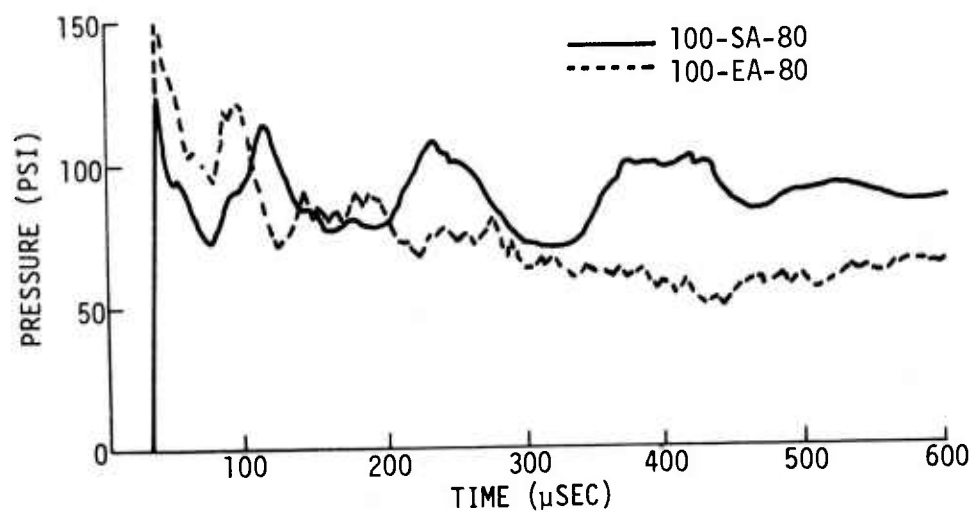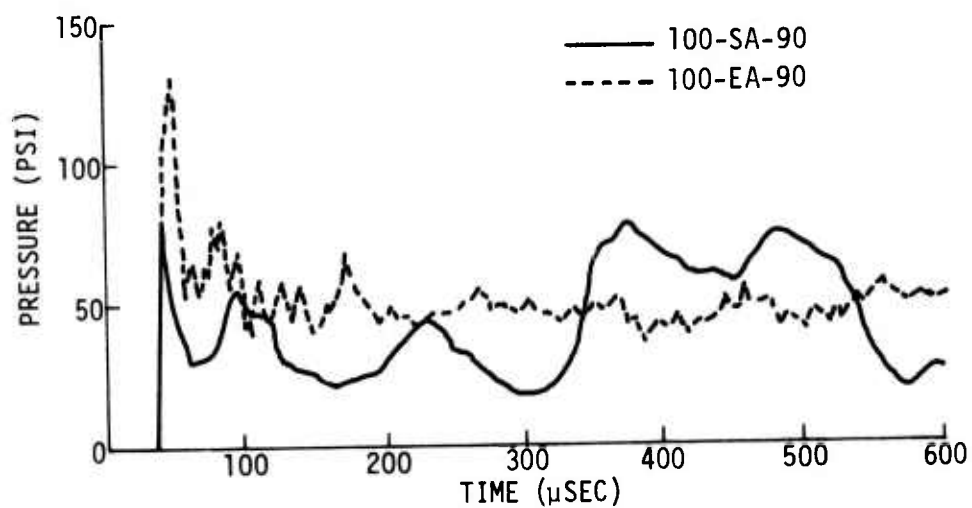
Figure 21. Simple Arch and Extended Arch Loading Comparisons -
100 Psi Overpressure

59

This effect would seem to be a geometry change relationship which will tend to alter the flow around the structure and the resulting dynamic pressures.

Arch structure loading comparisons for 300 psi incident overpressures are presented in figures 22 a, b, and c. The 70 degree locations exhibit no pronounced differences in either waveform or magnitude whereas the 80 and 90 degree locations again seem to realize the effects of the downstream extension. Also quite evident in these figures are later effects of combustion product arrivals for the extended models.

(2) Extended Rectangle

Simple rectangle (SR) and extended rectangle (ER) pressure-time histories are compared in figures 23 and 24 for the 100 psi and 300 psi overpressure levels. The obvious difference shown in the comparisons is for the extended model data to display somewhat higher pressure values after arrival of the initial loading wave. The higher values are in most cases then sustained throughout the recording time (prior to combustion products arrival). This result suggests that the extension produces a slight alteration in the flow around the rectangular structure which results in a higher total pressure acting on the top surface at the locations considered. The comparison shown in figure 23 e shows that the location near the top edge (100-SR-21T) realizes a significant effect from the deflection of the shock into the rear face region. However, the similar data for the 300 psi level shown in figure 24 e show a negligible effect. These two observations suggest that the 300 psi flow velocity exceeds the propagation velocity of any major disturbance from the downstream geometry change. The deviation in waveform shown in figure 24 d for the extended model 19T location does not seem to be a result of the model extension since a similar disturbance was not noted at the 21T location. This same reasoning indicates that the deviation does not result from an upstream disturbance either, based on the traces shown in figures 24 a, b, and c. Evidently the waveform change results either from a localized disturbance or from transient malfunctioning of the gage or recording system.

c. Wedge Extensions (Simulated Ground Planes)

The simulated ground plane tests were designed to collect data which would describe the behavior of reflected waves propagating upstream from the test structures. These data consisted of pressure-time measurements at the stagnation points (midheight) on the test structures and at one half and one
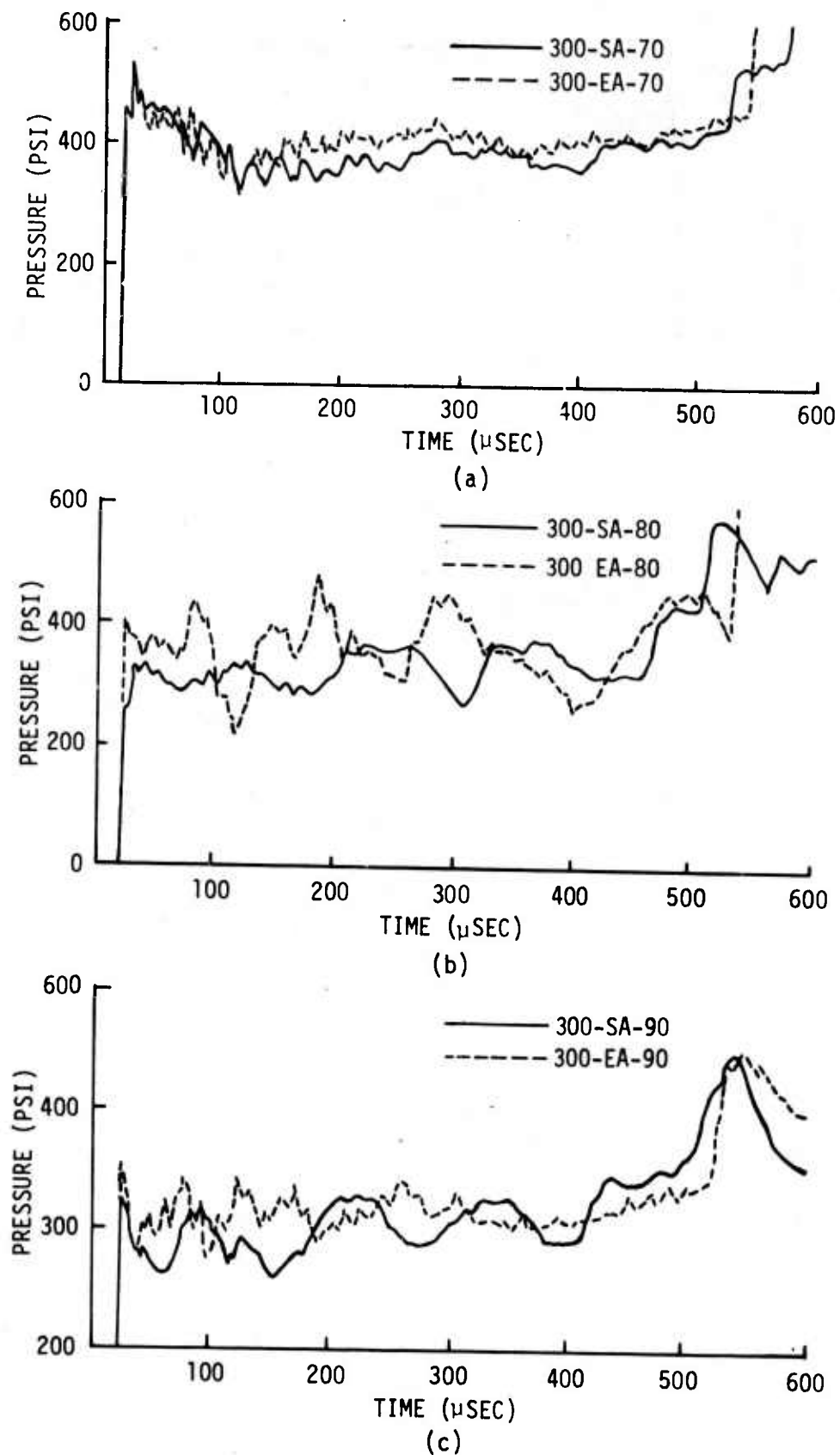
Figure 22. Simple Arch and Extended Arch Loading Comparisons - 300 Psi Overpressure
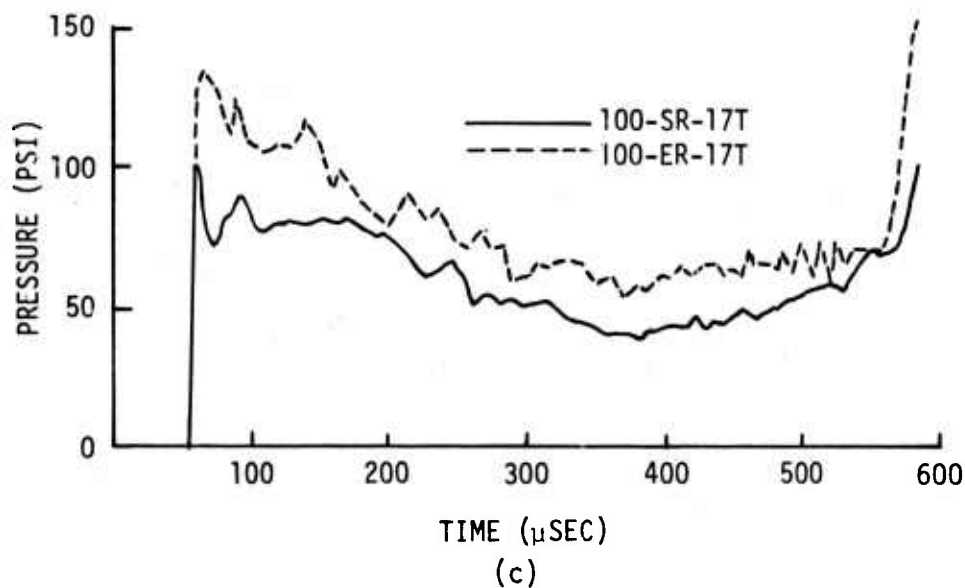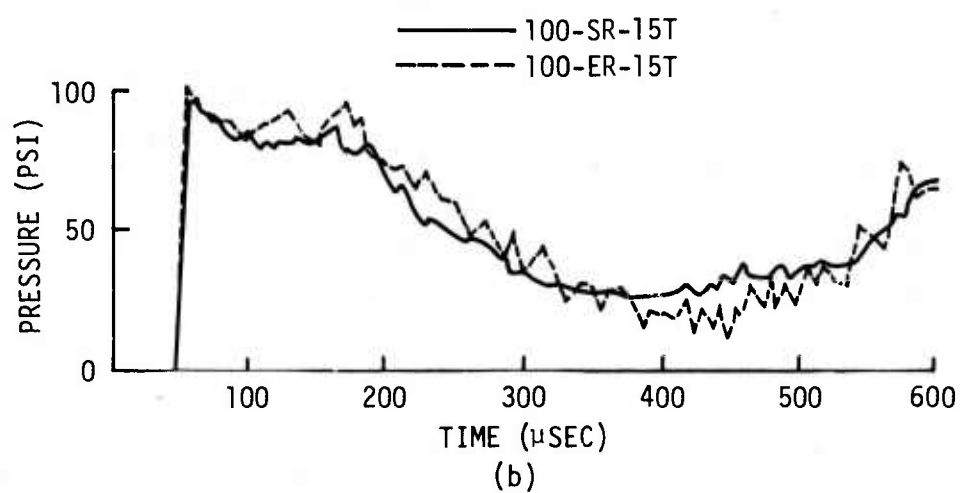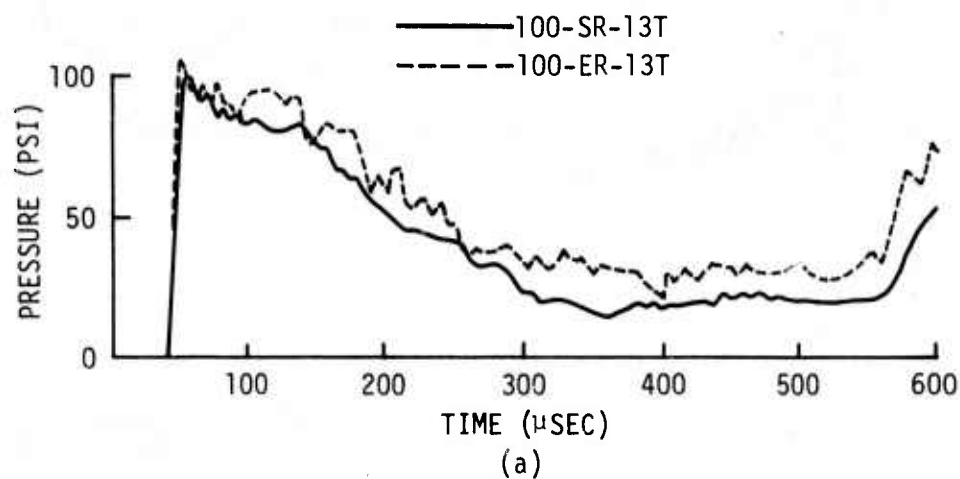
Figure 23. Simple Rectangle and Extended Rectangle Loading Comparisons - 100 Psi Overpressure
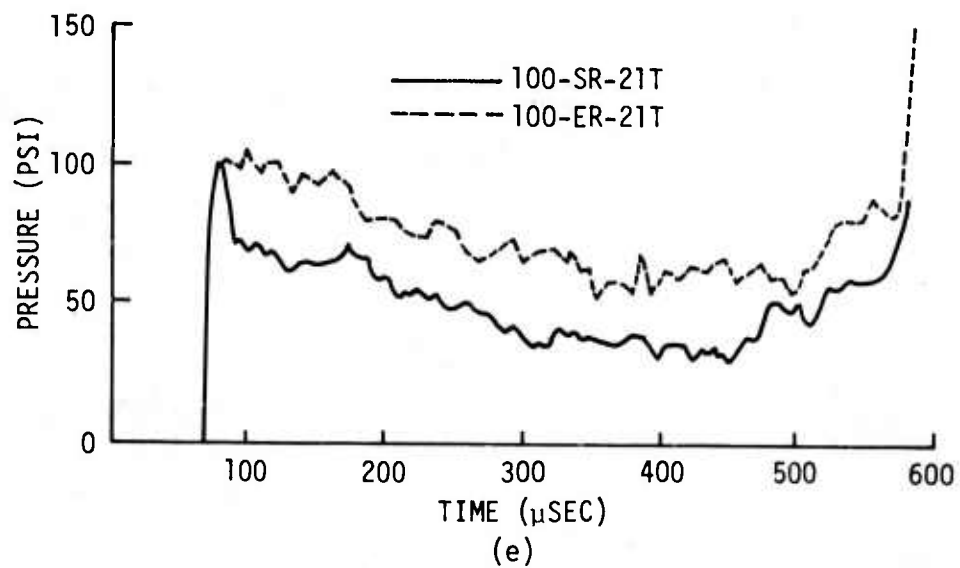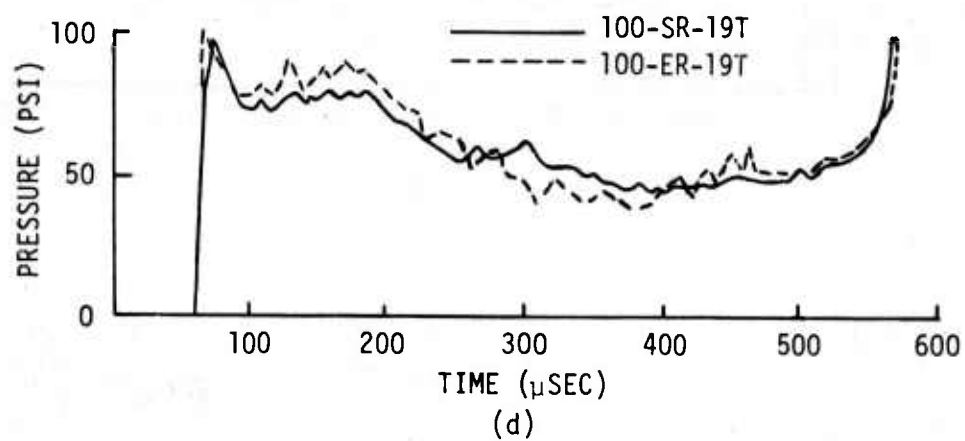
Figure 23. Simple Rectangle and Extended Rectangle Loading Comparisons - 100 Psi Overpressure (Continued)

Figure 24. Simple Rectangle and Extended Rectangle Loading Comparisons - 300 Psi Overpressure

(d)
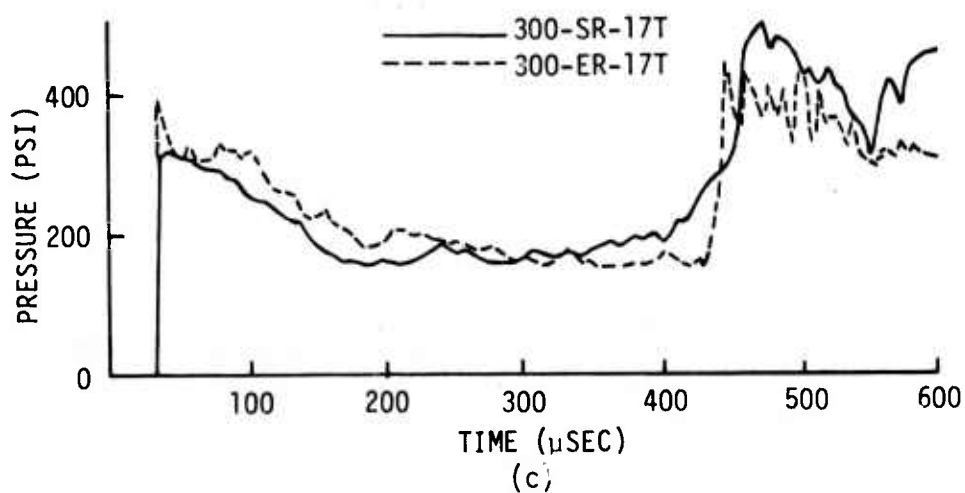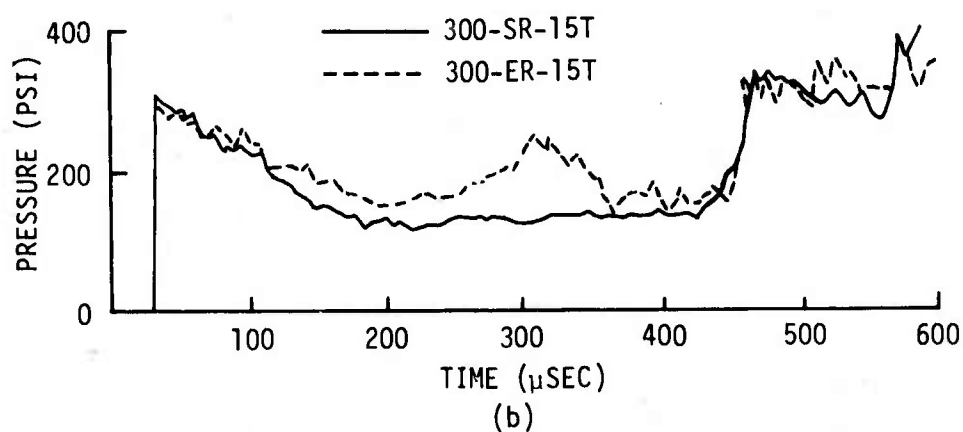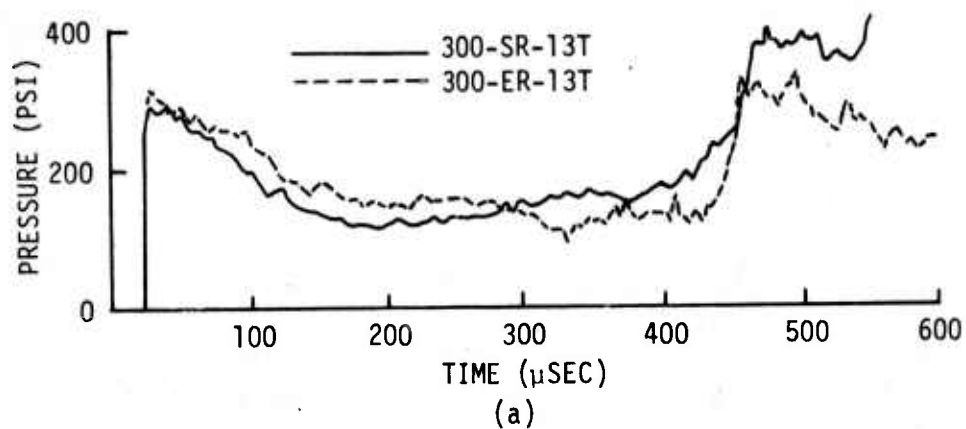
(e)
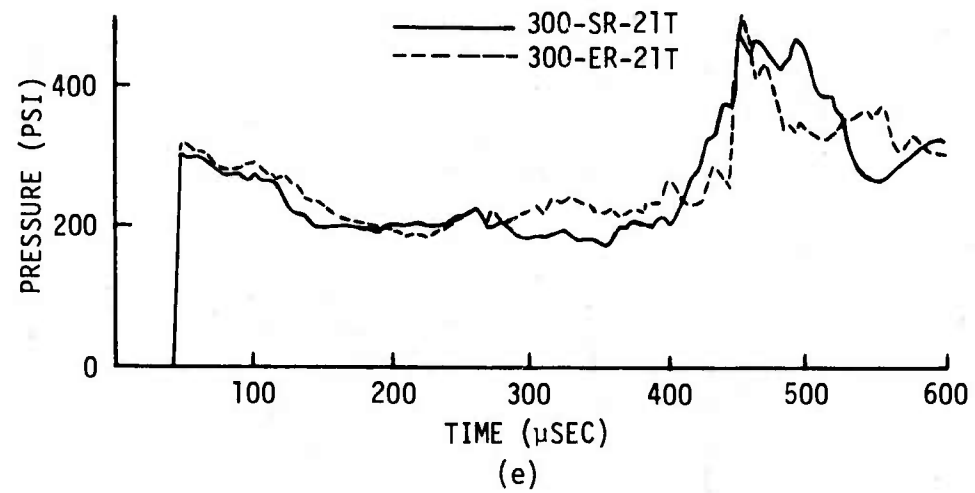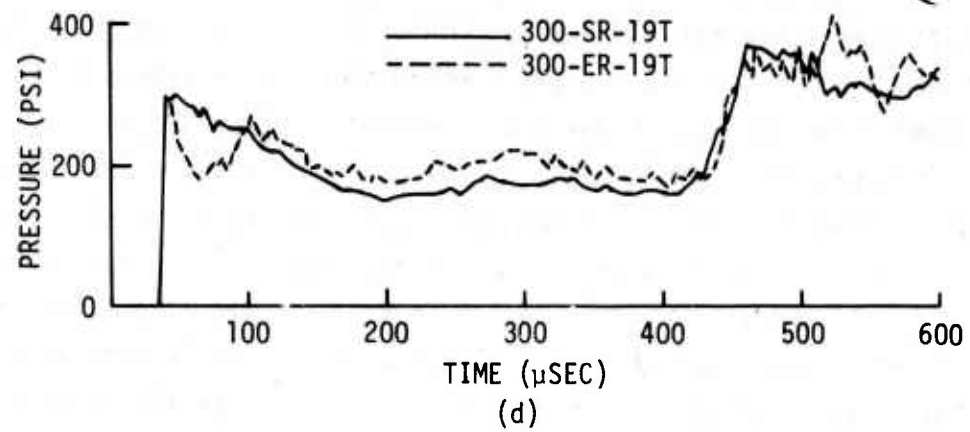
Figure 24. Simple Rectangle and Extended Rectangle Loading Comparisons - 300 Psi Overpressure (Continued)

structure height in front of the arch and rectangle. It was originally antici-
pated that the pressure-time recordings would additionally yield information
concerning rarefaction wave behavior, steady state pressure, and relief times
to steady state loading. The requirements for this information were based on
a preconception that the pressure-time history at a point away from the struc-
ture would be of the form shown in figure 25. This waveform would describe
the incident wave passage followed by the reflected wave from the structure.
It was then assumed the reflected wave would decrease uniformly to a steady
state level composed of free stream overpressure and an influence from the
dynamic pressure effects on the front face of the structure. As the experimen-
tal data in figures 26 and 27 demonstrate, this preconception was somewhat in
error. These figures show pressure-time measurements at the stagnation point
and at one half and one structure height in front of the structures for each
of the incident overpressure levels. Instead of a simple reduction to steady
state conditions after arrival of the reflected wave, the data show arrivals
of secondary loading effects from the structure.
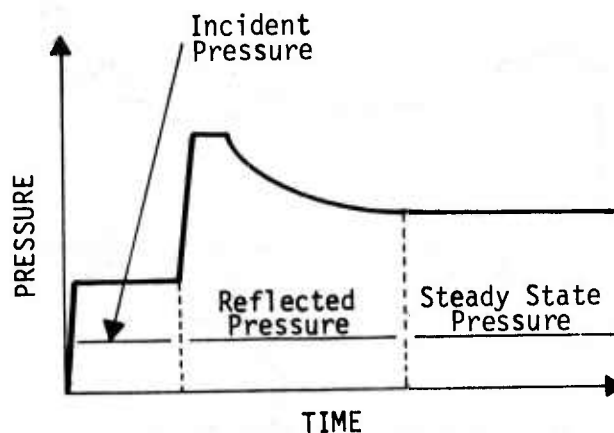
Figure 25. Expected Ground Plane Loading Behavior
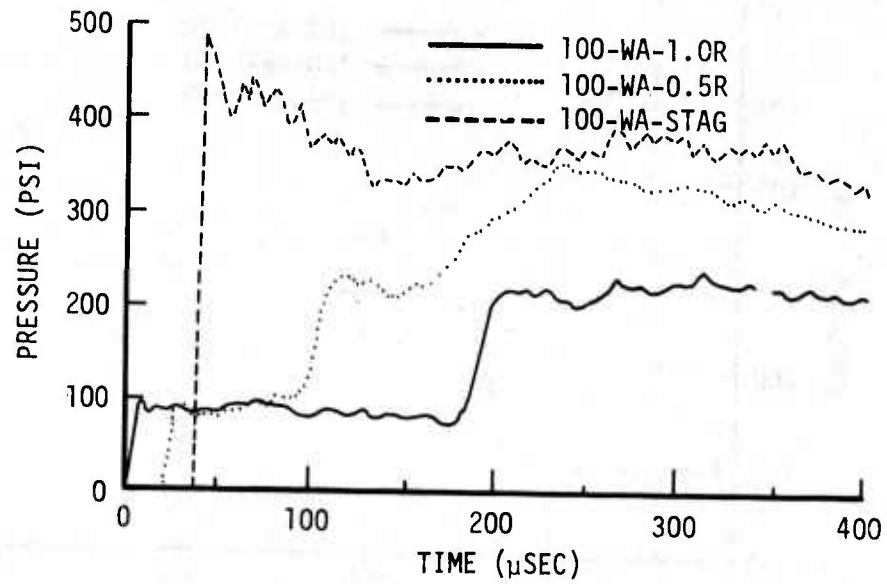
(a) 100 psi Overpressure
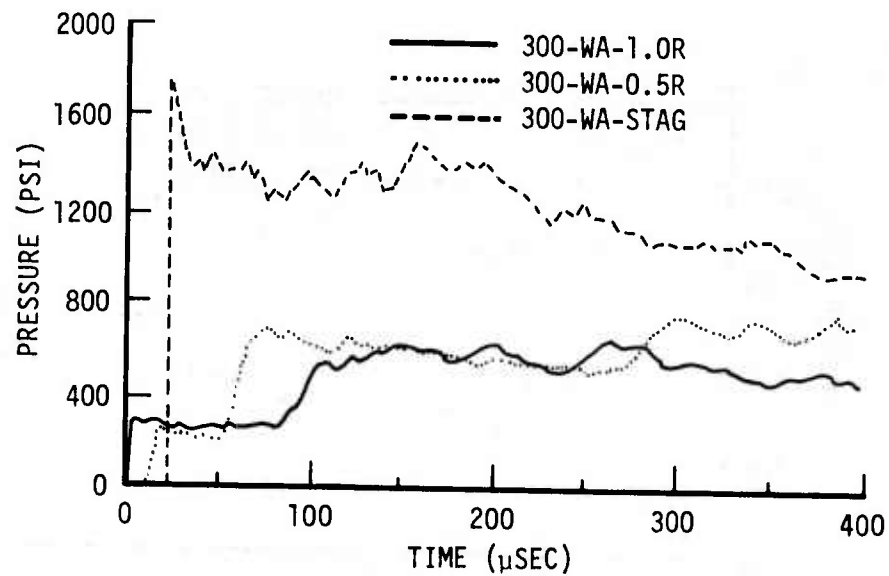
(b) 300 psi Overpressure

Figure 26. Measured Ground Plane Loading - Arch Structure
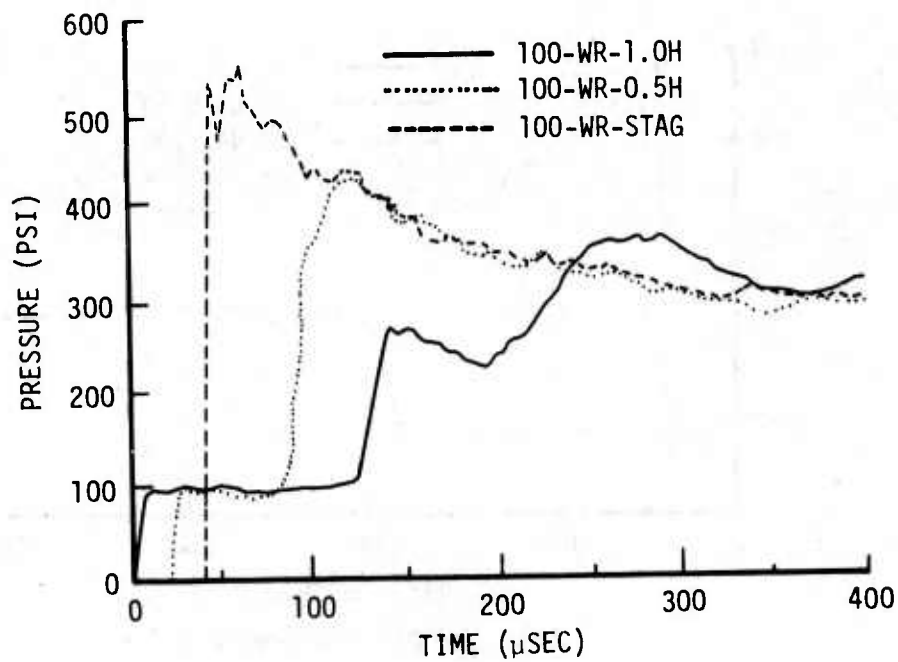
(a) 100 psi Overpressure
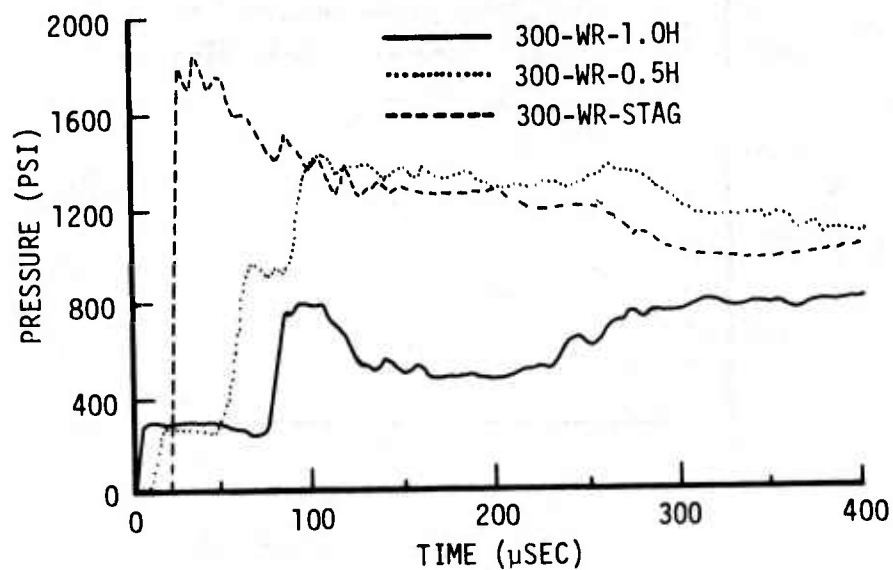
(b) 300 psi Overpressure

Figure 27. Measured Ground Plane Loading - Rectangular Structure

The 100 psi arch data in figure 26 show a marked attenuation of the reflected wave at the 0.5R position followed by a gradual rise in pressure which may be attributed to the dynamic pressure effects acting on the structure face and secondary reflections from the region near the intersection of the simulated ground plane and the structure face. Such reflections have been identified in Eulerian code calculations of shocks propagating into closed end tunnels where the initial reflected wave from the end face was found to reflect off the adjacent tunnel walls. The 1.0R location shows negligible attenuation of the reflected wave from the 0.5R location. The initial reflected wave magnitude at the 1.0R location is then sustained relatively constant for the remaining recording time. This sustained level is probably the result of the dynamic pressure effects generated by the structure.

The data in figure 26 b for the 300 psi arch show similar behavior. Again, a significant attenuation of the reflected wave occurs between the structure face and the 0.5R location. Between 0.5R and 1.0R, only a small reduction in reflected pressure is seen. Pressure levels at both locations then remain essentially constant. At the 300 psi level, the 0.5R location does not display the gradual increase in pressure noted for the 100 psi level. This observation suggests that the 300 psi incident pressure level is less susceptible to high secondary reflections than the 100 psi level. The fact that both positions register fairly constant pressure levels may indicate that the secondary reflections are within the pressure levels measured for the initial attenuated reflection and the later dynamic pressure effects from the structure.

The data collected for the 100 psi rectangular structure (figure 27 a) show lower attenuation rates and more pronounced secondary loads with late time pressures converging on the steady state pressure level measured at the stagnation point. The lower attenuation might be expected since the high initial reflected pressure is generated over a larger region and, further, these peak reflected values are sustained for a longer period of time on the face of the structure. The convergence of both curves to the steady state level measured at the stagnation point suggests that a constant dynamic pressure effect acts over a finite region in front of the rectangular structure. For the 100 psi level this region exceeds the structure height.

For the arch structure at the 100 psi level this region is approximately one half the structure height while at 300 psi this region is noticeably less than one half the structure height.

The 300 psi, rectangular structure data shown in figure 27 b exhibit a greater attenuation of the initial reflected wave between the structure and the 0.5H location than was shown for the 100 psi case. Between 0.5 and 1.0H the change in reflected pressure level is small followed by a rapid decrease to a relatively stable pressure level. After a period of time, the pressure again increases. This increase is too advanced in time to be a result of combustion products yet it seems too late to be a result of secondary reflections or dynamic pressure effects. The true source of the increase was not identified. The region of constant dynamic pressure effects from the structure extends beyond the 0.5H location, but does not reach the 1.0H location.

SECTION V

EVALUATION OF CURRENT PREDICTION TECHNIQUES

1. INTRODUCTION

The primary objective of this investigation was to determine the adequacy of existing methods to predict loadings on aboveground structures subjected to high incident overpressures. In this report the investigation was limited to those prediction techniques of a simplified nature. These simplified procedures allow a given overpressure-time history to be transformed into surface loads on a structure through the use of such parameters as reflection factors and drag coefficients and also with the use of shock wave characteristics and structure geometry considerations. The Air Force Manual for the Design and Analysis of Hardened Structures (ref. 3) was used as a source reference for the prediction techniques evaluated. This document represents the most current collection of recommended procedures for preliminary design or analysis of hardened strategic structures.

The format followed in evaluating these techniques was first to compare the basic transformation parameters proposed by the previous document with those determined in this effort. The actual structural loads measured during the investigation were then compared with those resulting from the prediction techniques.

2. REFLECTION FACTORS

a. Stagnation Probe Tests

Reproduced in figure 28 is the experimentally determined reflection factor curve from the stagnation probe test data. Superimposed on this figure is the normal reflection factor curve recommended by reference 3. The comparison shows higher values for the experimental data. These higher values should be expected since the experiments were conducted under atmospheric pressures of approximately 12 psi whereas the recommended curve was determined for sea level air. The comparison can therefore lend only additional support to the recommended curve.
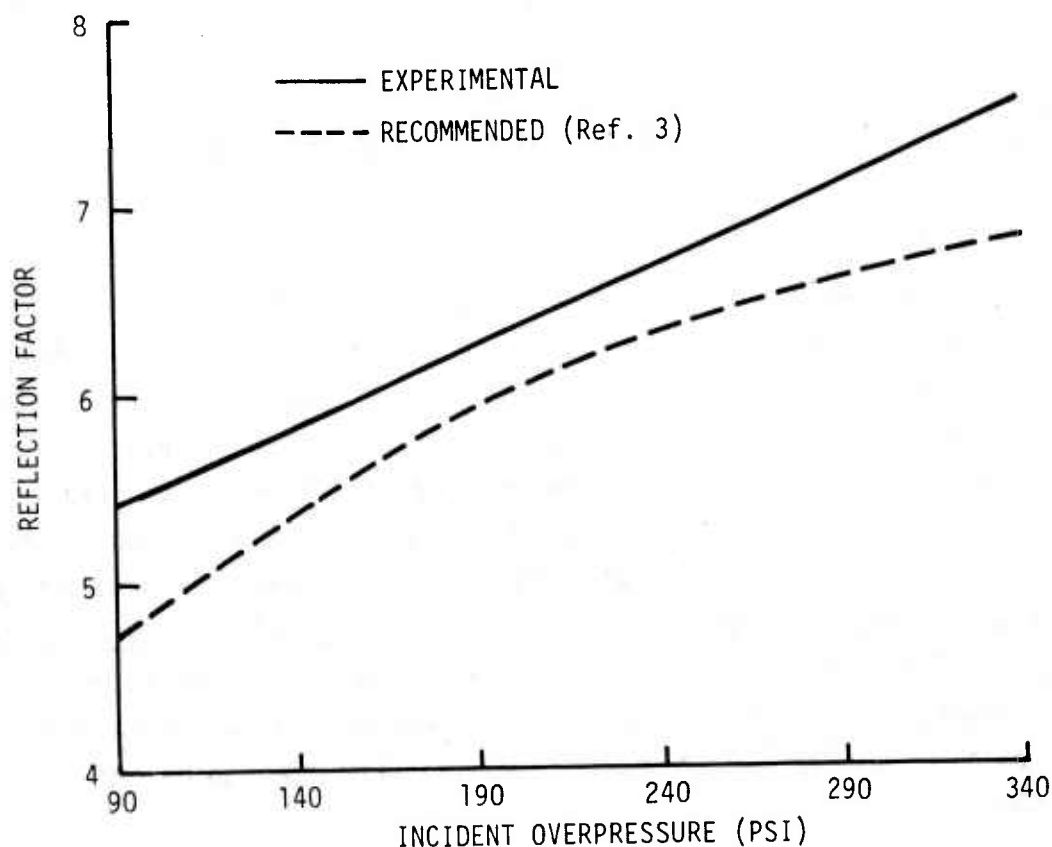
Figure 28. Variation of Reflection Factor with Incident
Overpressure - Stagnation Probe Tests

b. Simple Arch Structure

For the overpressures of interest in this investigation the "Design
Manual" does not clearly specify recommended reflection factors as functions of
angle of incidence on an arch structure. The "Manual" does, however, provide
reflection factors for shock waves impinging on inclined planar surfaces. Since
a user of this document will likely attempt to use these values in any analysis
requiring point load determinations, the comparisons in figure 29 are presented
for evaluation. The term "recommended" is used with a great degree of license
in these comparisons.

The recommended and experimental curves for the 100 psi level as a
whole demonstrate good agreement between reflection factors. The experimental
curve differs primarily by showing a greater variability in reflection factors

at angles of incidence between zero and the extreme angle for Mach reflection.
The actual location of the extreme angle is not clearly evident on the experi-
mental curve as a result of the poor resolution obtained with the relatively
coarse gage spacing. The true location of the extreme angle probably lies
either at the 40 degree location or at a slightly higher value since the 30
and 40 degree values represent a positive change in slope. If the extreme
angle was at some location between 30 and 40 degrees, a pronounced negative
slope change would be indicated.
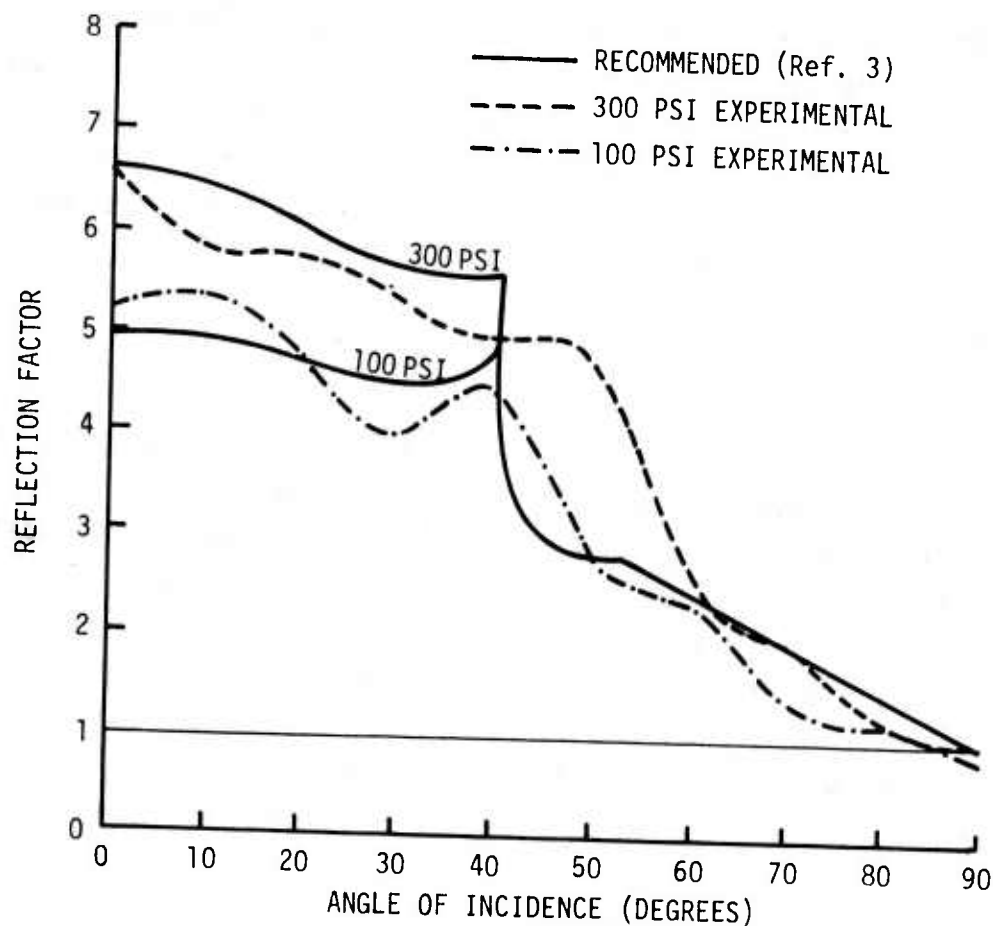
Figure 29. Variation of Reflection Factor with Angle of
Incidence - Arch Structure

At angles of incidence higher than the extreme angle, the experimental
values show slightly decreased reflection factors. This observation has even
greater impact remembering that the experimental values were determined under
ambient pressures of approximately 12 psi while the recommended values are for
sea level conditions which would yield even lower reflection factors for the
experimental data.

The comparisons for the 300 psi level indicate two areas of disagreement between the data. First, the experimental values are lower in magnitude within the region between zero angle of incidence and the extreme angle, again remembering the effect of lower ambient pressure. Second, the extreme angle is clearly located at an angle in excess of 40 degrees resulting in higher reflection factors encompassing a greater portion of the structure.

c. Simple Rectangular Structure

Because of the nature of its geometry and orientation to the shock wave, the simple rectangle will have an essentially constant reflection factor over its entire front face for any given overpressure level. Using composite pressure-time histories which yield the average pressure on the front face, reflection factor values of 4.8 and 6.4 were determined for the 100 and 300 psi overpressure levels. These values compare favorably with reflection factors of 4.9 and 6.6 recommended by the "Design Manual."

3. DRAG COEFFICIENTS

a. Stagnation Probe Tests

A comparison of the recommended drag coefficient curve for a disc-shaped object and the experimentally determined curve is presented in figure 30. The experimental curve shows a more definite increase in drag coefficient with increasing overpressure level. This larger increase may not be a completely accurate representation because of the small number of tests conducted at the higher overpressure levels. These values are all within the range of scatter experienced at the lower pressure levels (see figure 10). Only additional testing will determine truly representative values at these higher pressure levels. The larger number of lower pressure measurements does support the conclusion that the recommended curve (for lower pressures) overestimates drag coefficient values for these test conditions and the manner in which the dynamic pressures were determined.

b. Simple Arch Structure

The "Design Manual" does not provide recommended drag coefficients as a function of angle of incidence for the overpressure levels investigated in this report. The "Manual" does however suggest that for simplified loading conditions the total drag coefficient for an arch structure at high overpressures may be taken equal to one. This value compares fairly well with values of 1.25 and

1.15 determined from composite records which were constructed from the horizontal pressure components acting at each of the gage locations.
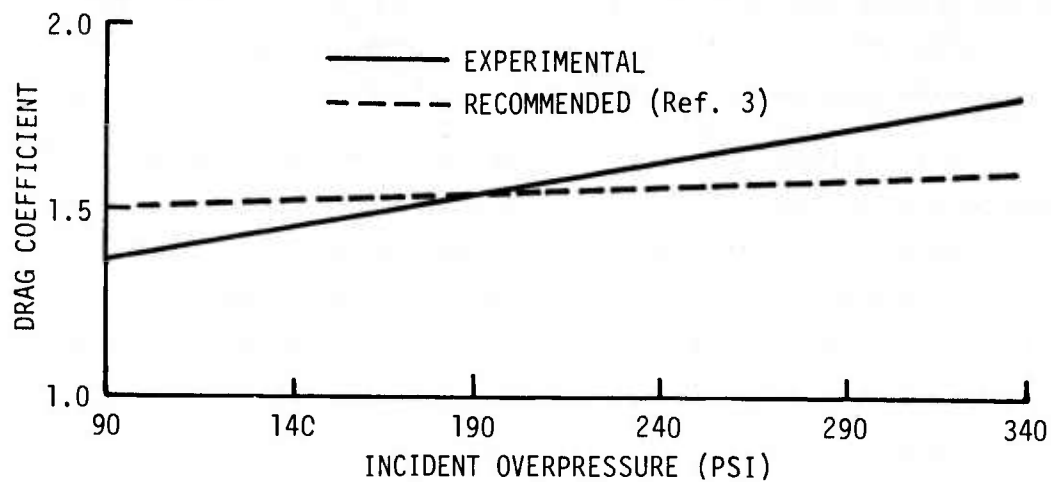
Figure 30. Variation of Drag Coefficient with Incident Overpressure - Stagnation Probe Tests

c. Simple Rectangular Structure

Surface drag coefficients are presented in the "Design Manual" for a rectangular structure, but only for average loads on an entire surface such as the front, roof, or rear face. For the roof and rear surfaces these recommendations are further restricted to incident overpressures less than 130 psi. In order to derive similar drag coefficient values, it was necessary to use composite records constructed from measurements common to each of the different structure surfaces. These composites are presented in subsection 4 where total loads on the structures will be presented.

Recommended front face drag coefficients of 1.25 and 1.45 are specified for the 100 and 300 psi overpressure levels. The experimental data yielded values of 1.3 and 1.5 for each of these pressure levels which resulted in excellent correlation between the experimental and recommended values.

A value of -0.2 is recommended for a drag coefficient on the roof of the rectangular structure at an overpressure level of 50 to 130 psi. The experimental data, on the other hand, indicate a drag coefficient of approximately -0.6 at the 100 psi level. At the 300 psi level the drag coefficient changes to a value of -0.3.
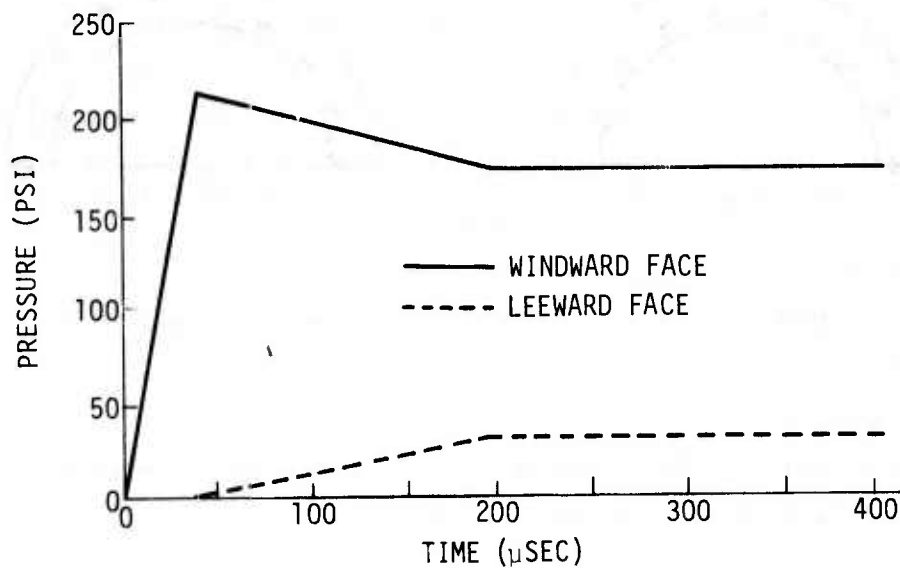
(a) 100 psi Overpressure
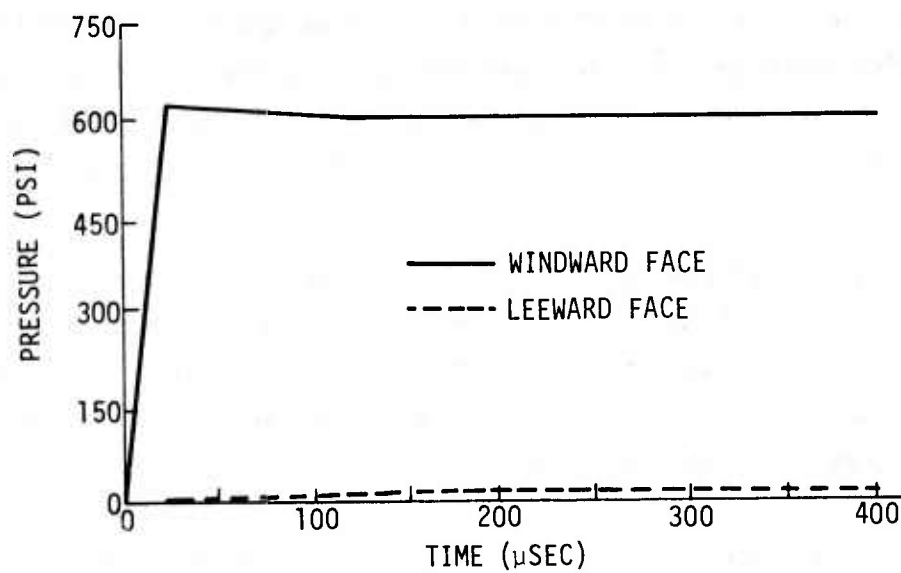
(b) 300 psi Overpressure

Figure 32. Predicted Average Surface Loadings-Arch Structure

Experimental drag coefficients of -0.5 and -0.1 were determined for the 100 and 300 psi overpressure levels on the rear face. However, these values are not truly representative of the entire rear face since only two pressure records were obtained at locations on the upper portion of the rear face (03B and 05B). The "Design Manual" recommends a value of -0.2 for overpressure levels between 50 and 130 psi.

It would seem that roof and rear face drag coefficients should be dependent upon surface size when specified as averages for an entire face. This statement is made in view of the occurrence of vortex behavior and possible flow separation at the leading edges of both the roof and rear faces. The accompanying reductions in pressure will therefore have a greater effect as the surface dimension in the direction of flow around the structure decreases.

4. TOTAL STRUCTURAL LOADS

A common technique used in preliminary design or analysis is to assume that surface loads on a structure are uniform along any given face of the structure such that time is the only variable considered. This technique allows estimates to be made of overturning moments, translational forces, and foundation reactions. In actuality, these estimates are often used for final design or analysis for lack of more precise capabilities. It is the purpose of this section to compare simplified analysis results with those determined experimentally.

a. Simple Arch Structure

Under simple loading conditions the "Design Manual" suggests an analysis which assumes an arch structure will respond in two primary modes; a breathing mode corresponding to a uniform overpressure and a flexural mode corresponding to a load applied radially inward on the upstream face and radially outward on the downstream face (see fig. 31). The assumed flexural loading is composed of two components which consider the unsymmetrical loads imparted to the structure as the shock wave passes over the arch and a drag component resulting from the continuing drag loading after the arch has been engulfed by the shock wave. The uniform radial pressure is assumed to increase linearly from zero to the maximum overpressure level in a time t_r given by

$$t_r = (1 - \phi/\pi)\tau$$

BREATHING MODE   FLEXURAL MODE
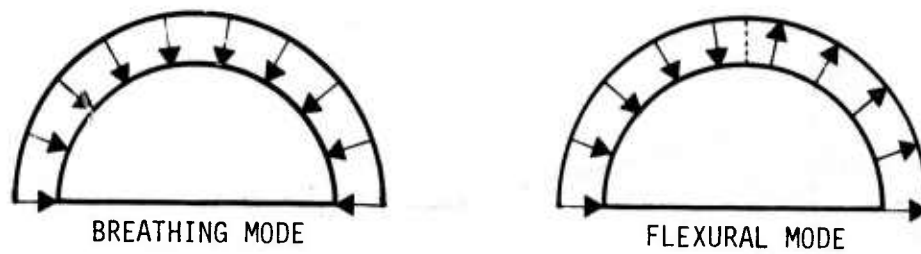
Figure 31. Assumed Response Modes for Arch Structure

where

τ = transit time of the shock wave across the structure

ϕ = half the central angle of the arch

Thereafter, the uniform radial pressure is assumed to vary as the free stream overpressure. The initial component of the flexural loading is assumed to increase linearly from zero to a maximum value of $\left[(1/2 + \phi/\pi) \, P_{so} - \dfrac{c_d q_o}{(2\pi/\phi)+6} \right]$ at a time $\tau/2$ and to decay linearly to zero at a time $(1 + 3\phi/\pi)\tau$. The drag component of the flexural loading increases linearly from zero to a maximum value of $(\phi/\pi)c_d q_o$ at a time $(1 + 3\phi/\pi)\tau$ and then remains equal to $(\phi/\pi)c_d q(t)$. For this effort the peak dynamic pressure, q_o, and time variation of dynamic pressure, $q(t)$, are equivalent. The "Design Manual" suggests that for high incident overpressures, a value of 1 may be used for the drag coefficient, c_d.

Using the above techniques, time variations of pressure as shown in figure 32 were determined for the 100 and 300 psi incident overpressure levels. The pressure levels at any given time shown in these figures may be compared to the pressure variations at similar times shown earlier in figures 11 and 12 where pressures as a function of position were presented. In making this type of comparison it is evident that not only do the predicted curves oversimplify the loading conditions, they also underestimate the average loads acting on either face of the arch at any given time. The effect of these differences on foundation reactions may be determined by considering the restraints necessary to prevent rigid body motion excluding inertial effects. The arch will be assumed rigid and to have pinned connections at the 0 and 180 degree points.
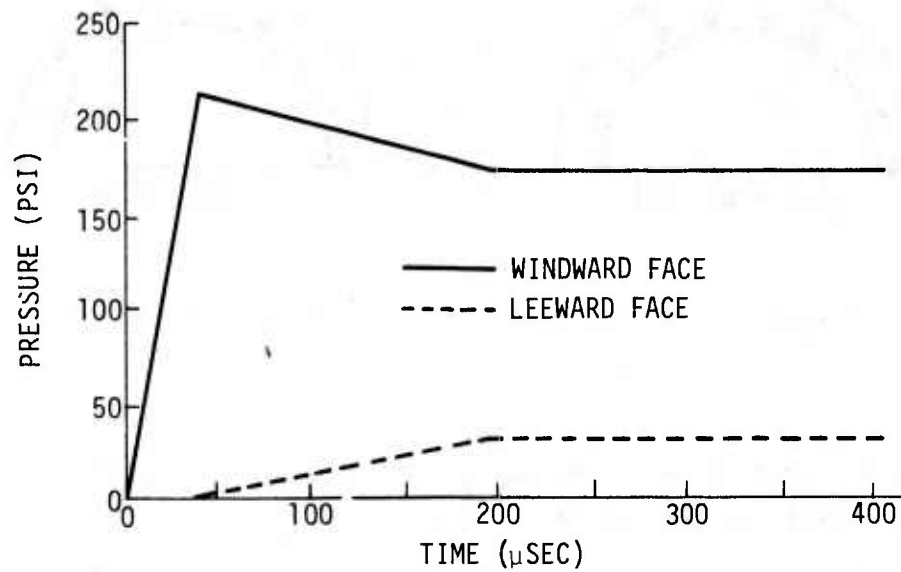
(a)   100 psi Overpressure
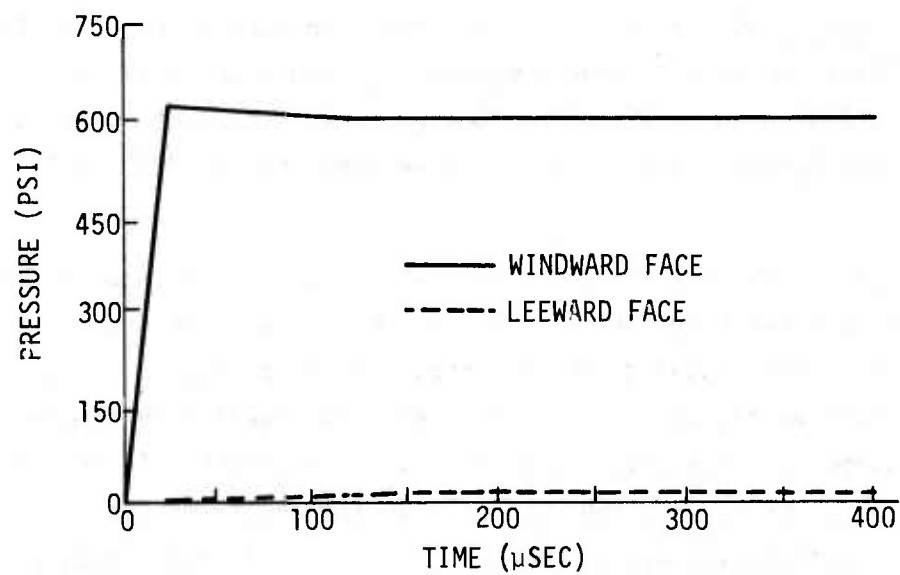
(b)   300 psi Overpressure

Figure 32. Predicted Average Surface Loadings-Arch Structure

Presented in figure 33 are the average vertical and horizontal pressures acting on the arch and the computed overturning moment about the downstream connection for the 100 psi overpressure level. During the true diffraction phase the predicted horizontal loading underestimates the actual by approximately 30 to 40 percent which is equivalent to stating that the required lateral restraint would be similarly underestimated. After the diffraction phase the differences between actual and predicted levels are small. The comparison in figure 33 b between the experimental and predicted average vertical pressures shows excellent agreement. However, this measurement is meaningless unless it is used with the calculated moments in figure 33 c to determine the vertical reactions at each of the connection points. The close correlations between the experimentally determined moments and predicted moments and the agreement shown for the average vertical loadings suggest that the prediction technique is satisfactory for determining vertical reactions at the structure supports.

Similar pressure and moment determinations are shown in figure 34 for the 300 psi overpressure level. The predicted horizontal pressures again underestimate the measured quantities showing greater differences during early times than were found for the 100 psi level. The late time quasi-steady pressure level is underestimated by approximately 15 percent. Unlike the previous lower pressure level, the 300 psi data show dissimilar comparisons for the average vertical pressures (fig. 34 b). These differences plug the major discrepancies between predicted and experimental overturning moments shown in figure 34 c will result in erroneous levels of predicted structure support reactions. After the maximum predicted levels of vertical pressure and moment are reached, the predicted levels result in an average underestimate of 30 percent at the upstream connection and an average overestimate of 18 percent at the downstream support (vertical reaction loads only). These differences plus the disagreement found between predicted and measured average horizontal pressures suggest that the simplified analysis techniques are somewhat unfavorable for the higher 300 psi overpressure level.

Both the 100 psi and 300 psi predicted time histories of horizontal pressure resulted in large underestimates of average loading during the diffraction phase. A review of the simplified analysis techniques presented earlier shows that these underestimates would quite naturally result since these techniques do not accurately address the reflection behavior on the front
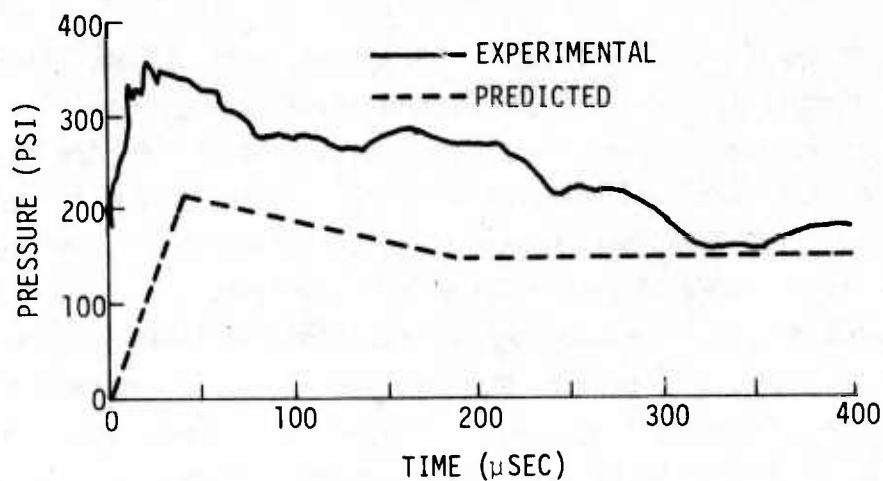
(a) Net Horizontal Loading
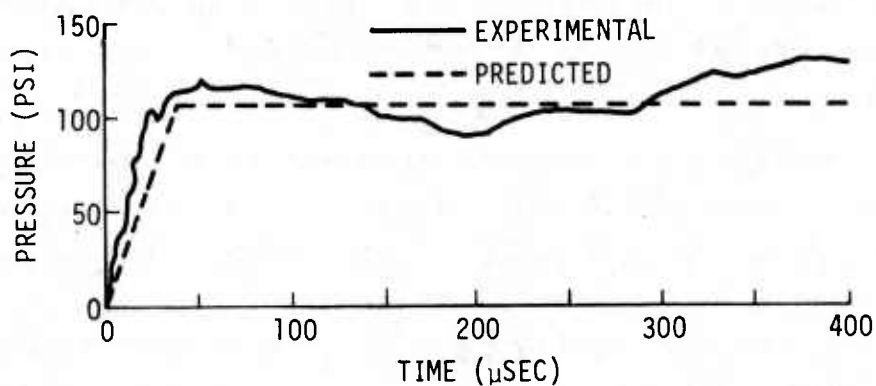
(b) Net Vertical Loading
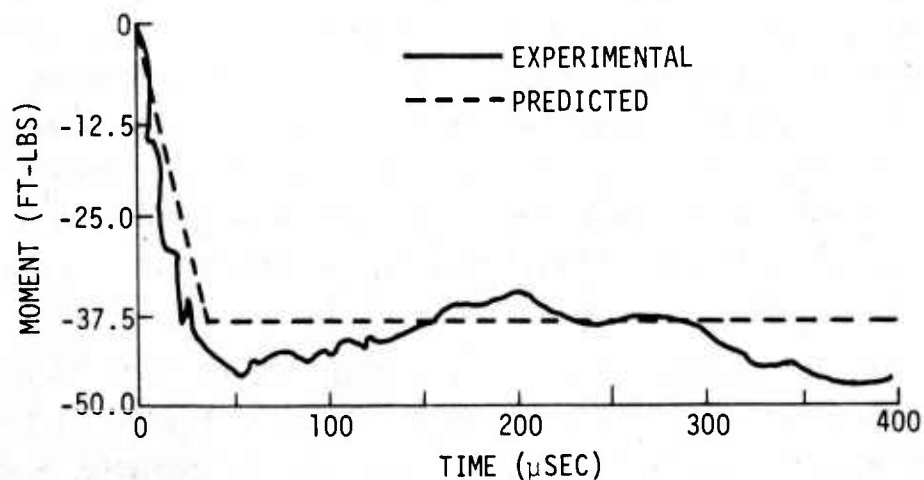
(c) Overturning Moment

Figure 33. Experimental and Predicted Arch Loadings - 100 Psi Overpressure
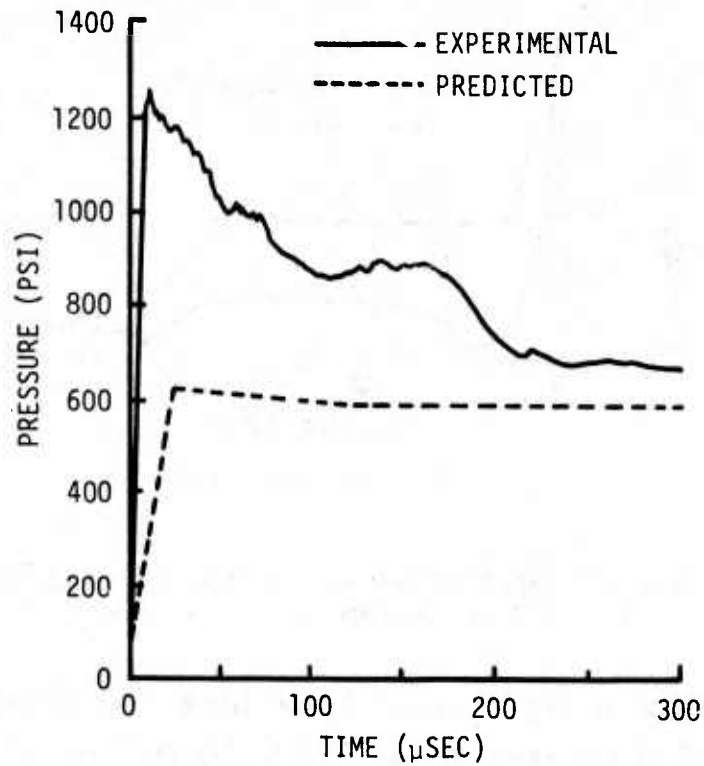
(a) Net Horizontal Loading
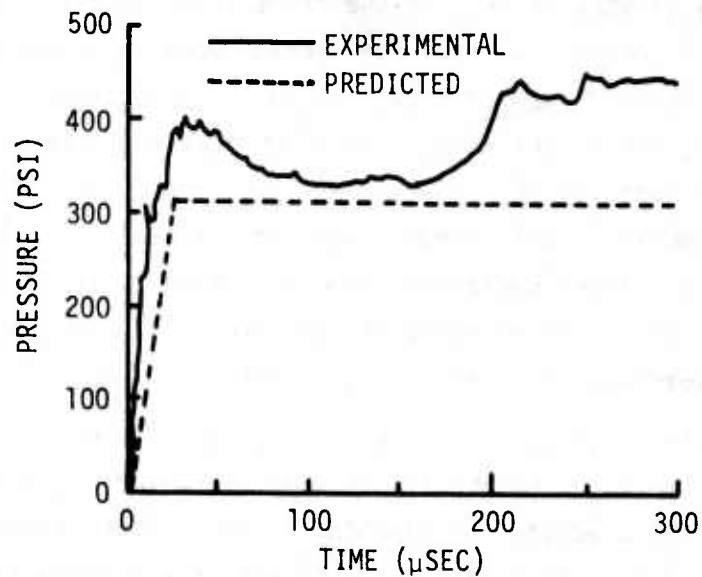
(b) Net Vertical Loading

Figure 34. Experimental and Predicted Arch Loadings - 300 Psi Overpressure
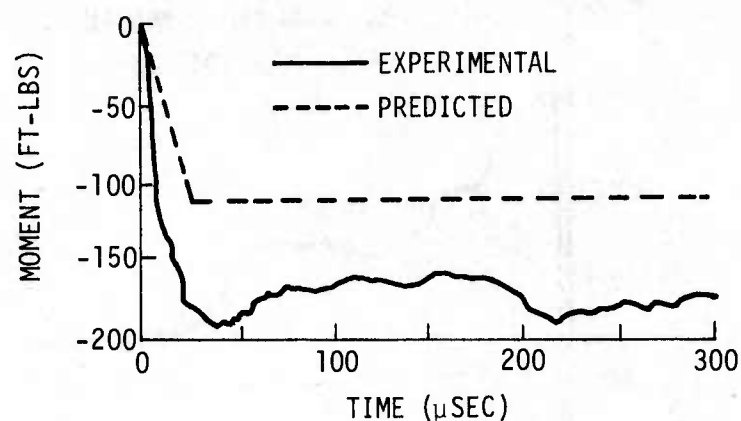
(c) Overturning Moment

Figure 34. Experimental and Predicted Arch Loadings -
300 Psi Overpressure (Continued)

face. The maximum average pressure on the front face for any given overpressure is limited by the value of the $[1/2 + \phi/\pi]$ term in the expression for the initial flexural loading. For the cases investigated this term has a value of 1. Since the drag component of flexural loading represents a negligible quantity during the time of peak loading, the peak average reflected pressure is effectively limited to $2P_{so}$ on the front face. Referring back to figures 11 and 12 the data indicate that the average peak values are on the order of $3P_{so}$ (300 psi and 1000 psi) for each of the overpressures investigated. The error is compounded by the assumption of uniform pressure across the surface. The higher pressure levels occur at the lower angles of incidence (less than $\simeq 45°$) where the loading is predominantly horizontal. The uniform assumption would result in a lower horizontal component even if the average pressure level was accurate. In a similar sense the uniformity assumption also will affect the values determined for overturning moment.

The later time quasi-steady loading showed somewhat reasonable prediction values in terms of horizontal loading. However, as shown in figures 33 c and 34 c, the predicted overturning moments differ appreciably from the measured data. Again, this difference is directly related to the assumption of uniform surface loading on the front face. In all cases the assumption of uniform pressure on the rear face is not too unreasonable since the pressure levels tend to vary about a median level.

For the average vertical loads across the entire structure, the prediction techniques result in uniform pressure equal to the incident overpressure. This result is caused by the cancellation of vertical components from the flexural loadings which are radial and in on the front face and radial and out on the rear face. In reality, this effect could be realized during the post diffraction loadings and under simple loading conditions only if the average drag coefficients on the front face were equal in magnitude and opposite in sign to the rear face value. Figure 14 shows this not to be the case and figures 33 b and 34 b show the result at late times. For low overpressure levels the assumed behavior may be more accurate.

The predicted pressure-time histories additionally underestimate the time duration of the diffraction process which is limited by the $[1 + 3\phi/\pi]$ term. A more accurate value for the conditions examined is $[1 + 7\phi/\pi]$.

b. Simple Rectangular Structure

The "Design Manual" techniques for estimating average loads on an aboveground rectangular structure are based on the simplified loading behavior shown in figure 35. The average load on the front face is assumed to rise to a peak reflected pressure (P_{RO}) in a time (T_R) equal to the rise time of the incident overpressure. The value of P_{RO} is determined from the incident overpressure and its corresponding reflection factor for normal reflection. The peak reflected pressure is then assumed to decay linearly to a quasi-steady pressure level equal to the overpressure plus the drag component of loading which is determined from the free stream dynamic pressure and front face drag coefficient. This quasi-steady loading is assumed to decay in the same manner as the free stream overpressure plus resulting drag pressure. The decay time of the reflected pressure is assumed equal to the time required for a rarefaction wavefront to travel from the nearest edge of the front face to the stagnation point and then return to the edge of the structure (stagnation time). The average roof loading on the structure is assumed to rise linearly to a peak value in a time equal to the rise time of the blast wave plus the transit time of the shock wave across the roof. The peak value is defined as being equal to the incident overpressure reduced by a drag component resulting from a negative drag coefficient and the peak dynamic pressure. After this time the average pressure is taken equal to the current overpressure reduced by the negative drag pressure determined from the current dynamic pressure. The "Design Manual" additionally provides a similar technique for determining

83

the average loading on the rear face of the rectangular structure. However, an insufficient number of measurements were conducted on this face to justify a comparison.
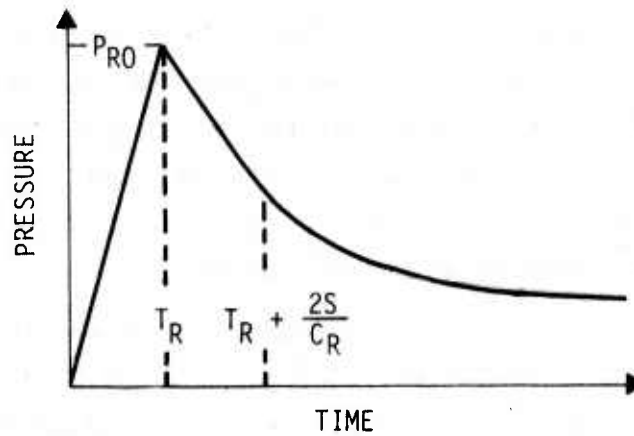
(a) Front Face
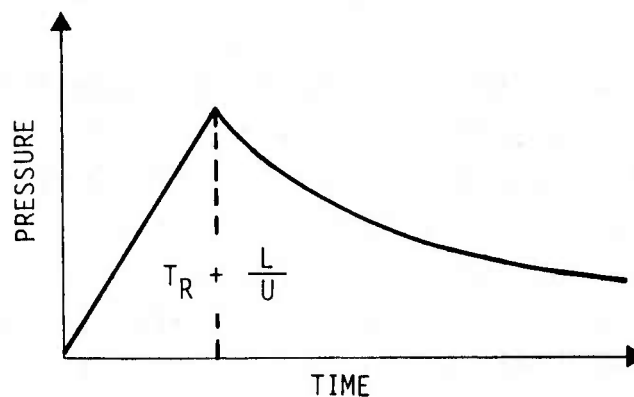
(b) Roof

Figure 35. Simplified Loading Behavior - Rectangular Structure

Using the above techniques, average pressures were determined for the front and roof surfaces of the rectangular structure and are compared to the experimentally determined averages in figures 36 and 37. The predicted time histories for the 100 psi level shown in figure 36 were determined using a reflection factor of 4.9, a front face drag coefficient of 1.25, and a roof drag coefficient of -0.2. As the comparisons demonstrate, the prediction
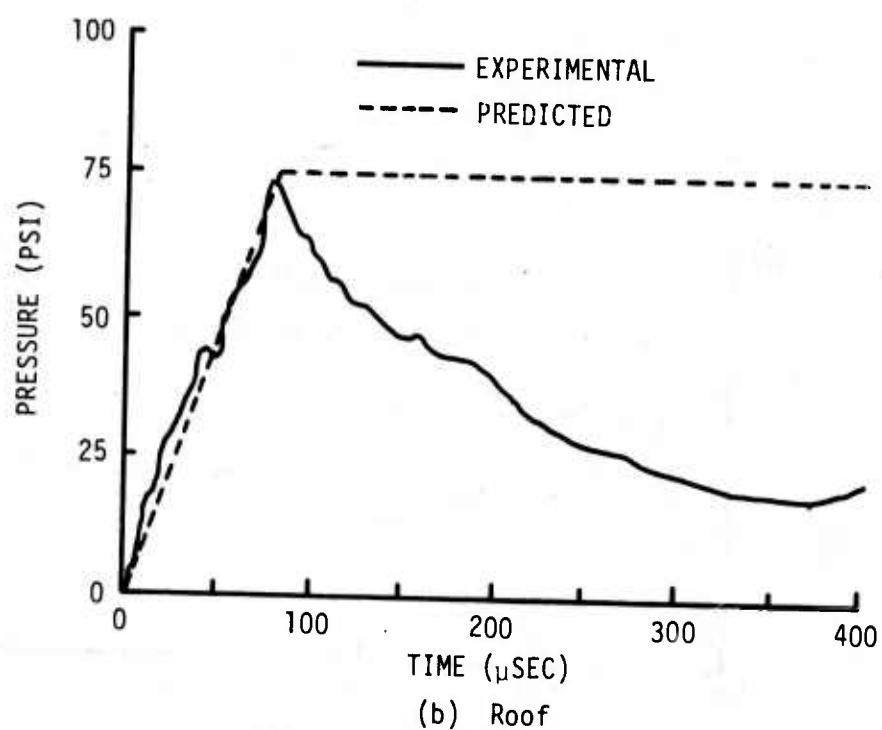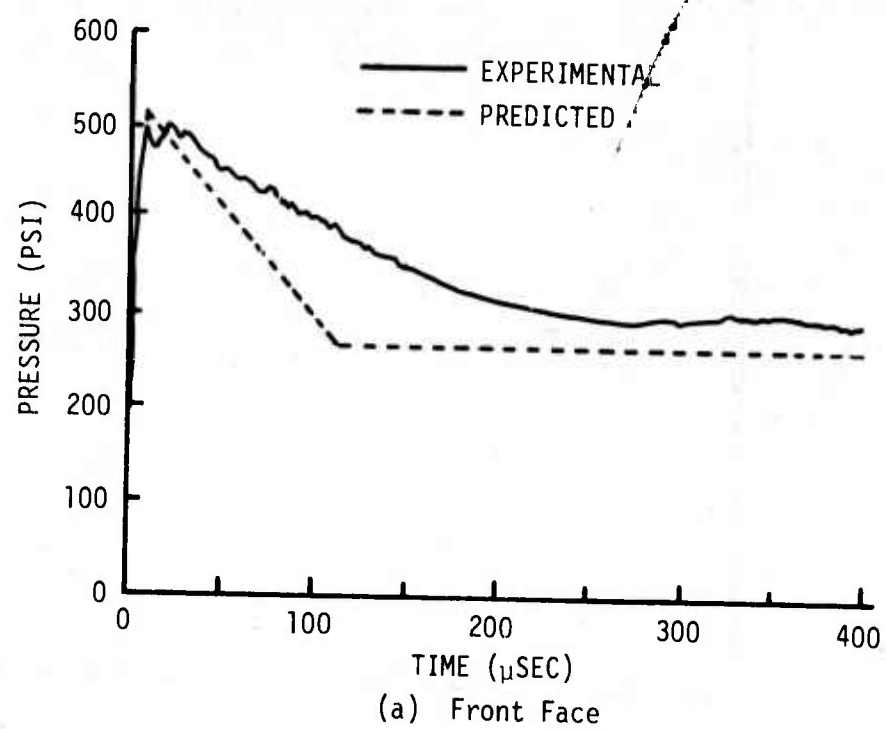
(a) Front Face

(b) Roof

Figure 36. Experimental and Predicted Rectangular Structure
Loadings - 100 Psi Overpressure
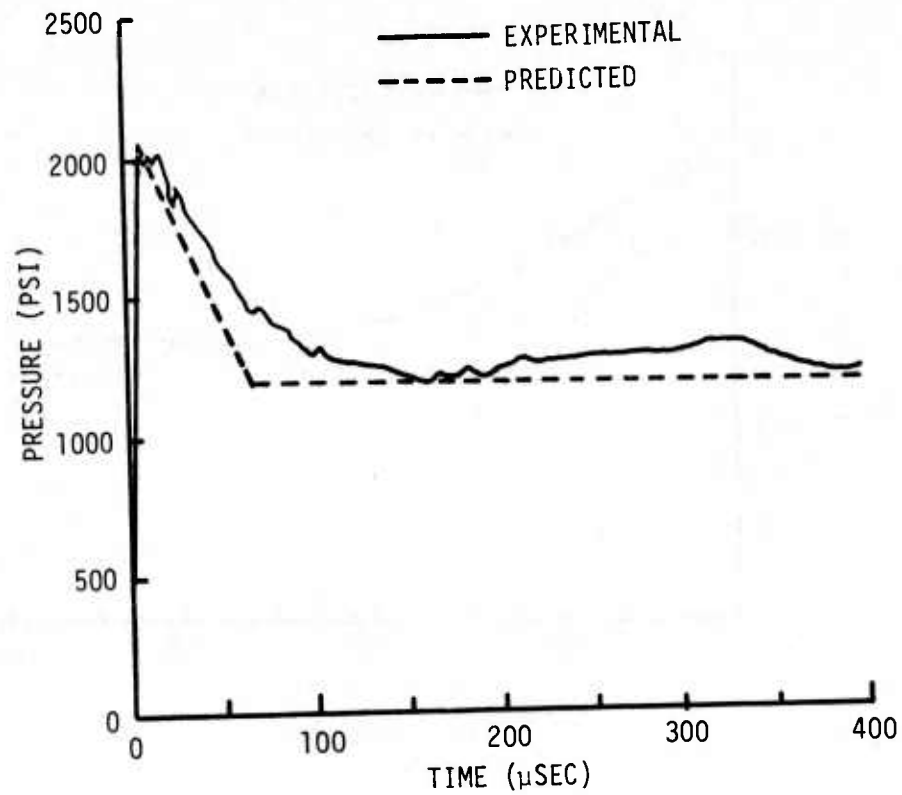
(a) Front Face
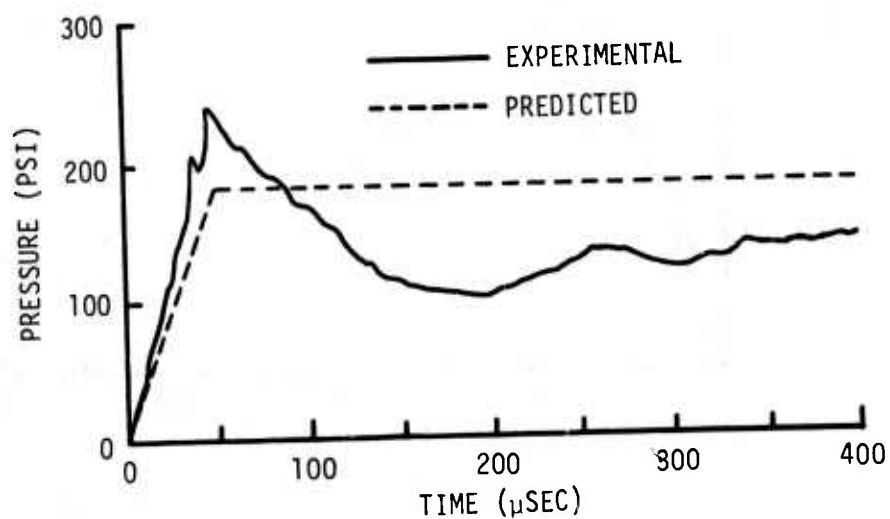
(b) Roof

Figure 37. Experimental and Predicted Rectangular Structure
Loadings - 300 Psi Overpressure

techniques yield favorable results for the front face loading, with the exception of stagnation time, and unsatisfactory results for the roof loading. The experimental data show that for the front face more appropriate load parameters would be a reflection factor of 4.8, a drag coefficient of 1.3, and a stagnation time of $4S/C_R$. The increased stagnation time is probably the result of the simplified procedure not taking into account the duration of the rarefaction wave. Excellent agreement is shown for the roof loading during the transit time of the shock across the structure top surface. However, the simplified technique significantly overestimates the average loading occurring during the quasi-steady loading period. As discussed earlier, the initial flow across the top surface is probably parallel to that surface such that a drag coefficient of -0.2 is appropriate for determining the initial peak pressure level. However, once the flow field has stabilized following the diffraction period the flow is no longer parallel across the top surface of the structure. This resulting nonparallel flow results in a quasi-steady drag coefficient of -0.6. Assuming that the relationship is scalable, the experimental findings suggest that for structures with similar height (stagnation distance) to length ratio (S/L = 2) the average roof loading may be described by a linear rise to a peak pressure defined by the overpressure reduced by a negative drag component resulting from a drag coefficient of -0.2 in a time equal to the transit time across the roof surface. The quasi-steady loading may then be taken equal to the current overpressure reduced by a negative drag component determined by a drag coefficient of -0.6. The decrease from peak pressure level to quasi-steady level may be assumed linear and to occur over a period of time equal to twice the shock wave transit time across the surface.

The predicted front and top surface average pressure loadings are compared in figure 37 to the measured time histories for the 300 psi overpressure level. A reflection factor of 6.5, front face drag coefficient of 1.45 and a rear face drag coefficient of -0.2 were used in the predictions. The front face loading comparison demonstrates excellent agreement between predicted and measured values. The only discrepancy shown is that the predicted curve indicates a shorter clearing time than was actually measured. The actual stagnation time was approximately 3.5 S/C_R. However, to maintain the total impulse delivered to the front face during the diffraction period, a linear decay to quasi-steady pressure level in a time equal to 3 S/C_R is more appropriate for the 300 psi overpressure level. The comparison of average roof loadings shows that the predicted curve underestimates the initial peak load

and overestimates the late time quasi-steady loading. Drag coefficients of -0.1 and -0.3 are more correct for the initial load and the late time loading, respectively. A linear relief to the lower pressure level in a time period of 1.5 transit times of the shock across the structure surface would adequately simulate the average loading behavior.

The experimental and predicted overturning moments calculated about the lower rear edge of the rectangle are presented in figure 38 for both overpressure levels. These moment determinations do not consider the resistance provided by the rear face loadings since an average experimental rear face pressure could not be accurately determined with only two measurements. Nevertheless, the curves may be used with the average front face and roof loadings to provide some information on the nature and degree of error inherent in the simplified techniques for determining the required foundation restraints to prevent overturning. The same assumptions concerning rigid body behavior, inertial effects, and structure supports as made for the arch structure are applied to the rectangular structure.

Figure 39 shows a comparison of the experimental and predicted vertical support reactions determined for the 100 and 300 psi overpressure levels. A sign convention of positive values representing compressive reactions is adopted. At both overpressures, the comparisons indicate good agreement during the diffraction period for each support location. The later time comparisons are not quite as good except for the 300 psi downstream support where excellent agreement is found. The 100 psi data show a relatively large overestimate of compressive reaction and underestimate of tensile reaction. An underestimate of tensile reaction is also observed for the 300 psi data. Both the overestimate of compressive reaction and underestimates of tensile reactions are directly related to the late time overestimate of roof loading which resulted from the prediction technique.

c. Simulated Ground Plane

When surface flush elements are located in the vicinity of aboveground obstructions, these elements may be subject to reflected pressures and drag pressures originating at the obstruction. Whether these effects are realized depends on the location of the element with respect to the aboveground protrusion. The "Design Manual" provides a technique for estimating the loading on surface flush elements located near rectangular aboveground structures. This technique will additionally be used for the arch structure although not
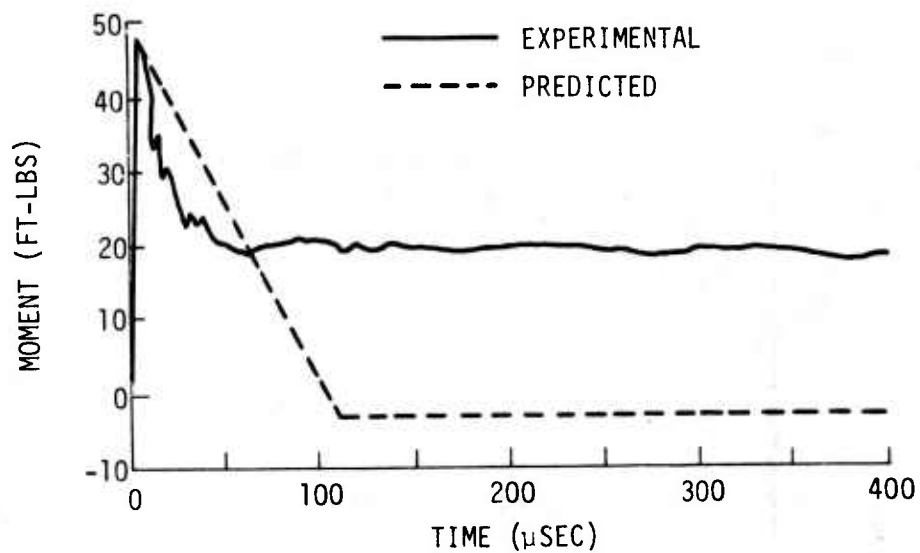
(a) 100 psi Overpressure
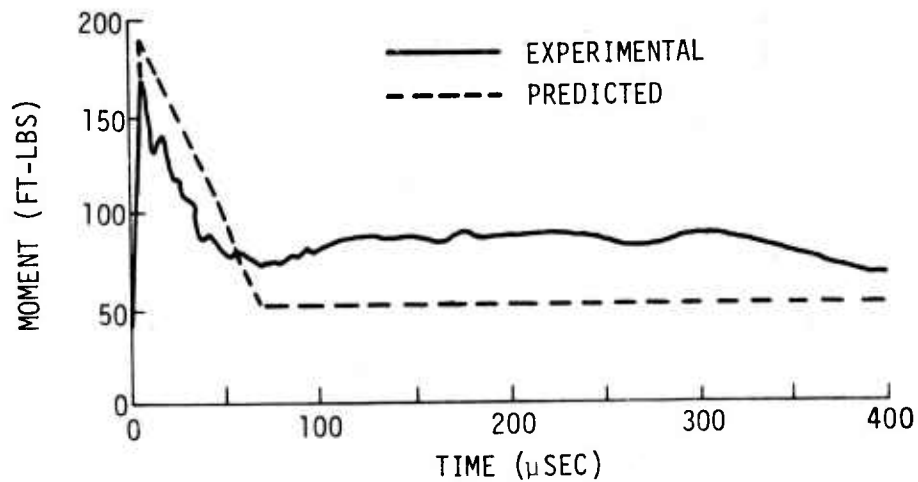
(b) 300 psi Overpressure

Figure 38. Experimental and Predicted Overturning Moments - Rectangular Structure
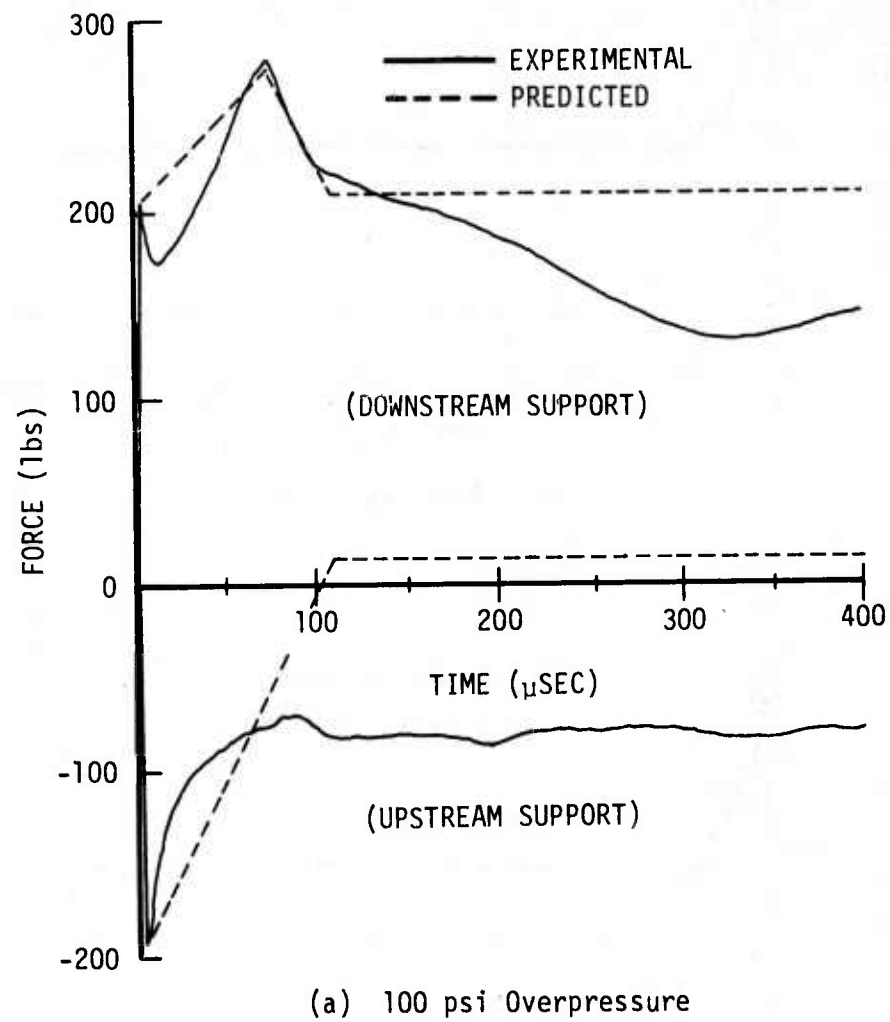
89
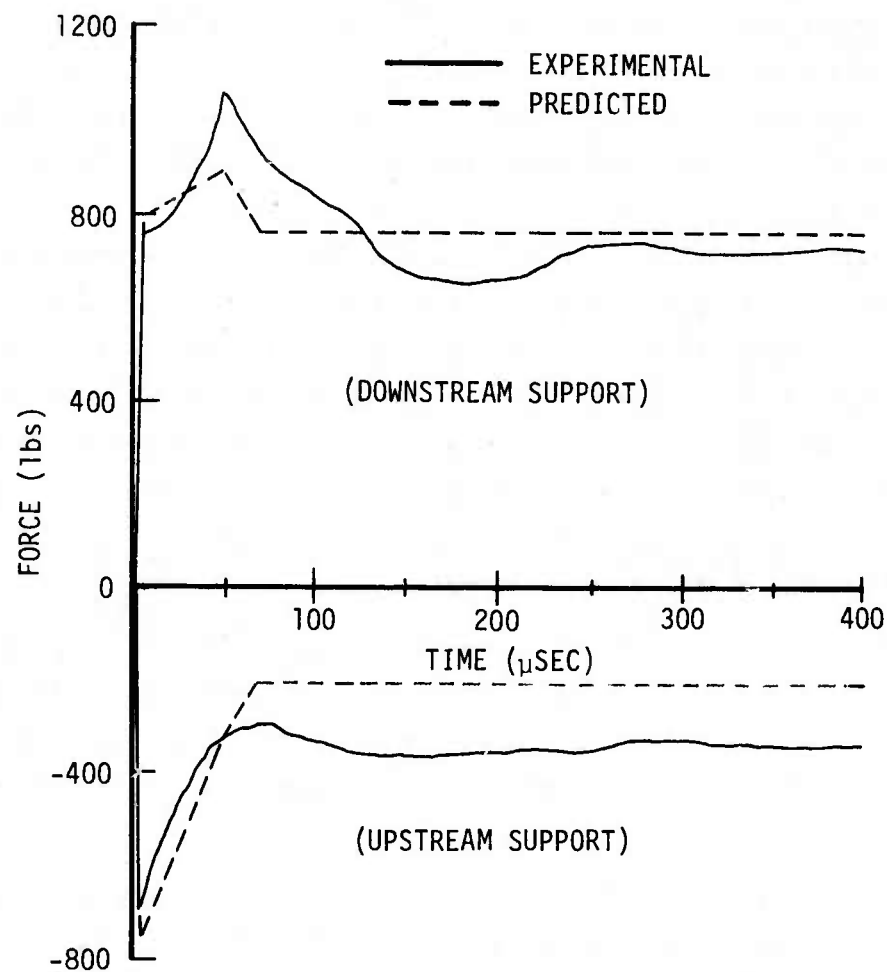
(a)   100 psi Overpressure

Figure 39. Experimental and Predicted Vertical Support Reactions -
Rectangular Structure

(b)   300 psi Overpressure

Figure 39. Experimental and Predicted Vertical Support Reactions - Rectangular Structure (Continued)

recommended. The "Design Manual" states that drag effects are felt within a range equal to the height of the structure along the ground surface in front of or behind the structure. The magnitude of this drag effect is taken equal to that acting on the front or rear face depending on where the surface flush element of interest is located. Reflected pressures are assumed to act over a distance KS in front of the structure where S is the structure height and K is a factor depending on the rarefaction (C_R) and reflected (U_R) wave speeds. The value of K may be estimated by $K = 2/(C_R/U_R - 1)$. For a distance KS/2 in front of the structure, the reflected pressure level is assumed equal to that acting on the front face. Over the remaining KS/2 distance the peak reflected pressure above the incident overpressure level is assumed to attenuate linearly to zero from the pressure level acting on the front face. Allowing D to represent the distance of the point of interest in front of the structure, the reflected pressure is assumed to vary as the front face reflected pressure for a period of time equal to $\left[\dfrac{S}{C_R} - \dfrac{2D}{KC_R}\right]$. For times greater than this value or distances D greater than KS/2 the reflected pressure level is assumed to attenuate linearly to the incident overpressure level or incident overpressure plus drag pressure if D is less than the structure height. The total duration of the reflected pressure at any point is taken equal to $\left[\dfrac{2S}{C_R} - \dfrac{2D}{KC_R}\right]$.

The results of the above prediction techniques are compared with the measured data in figures 40 and 41 for each structural shape and each overpressure level. The front face pressure waveforms (D=0) used for the predictions are those determined earlier with the techniques presented in subsections 4.a and 4.b.

The comparison for the 100 psi arch shown in figure 40a immediately shows that the prediction technique grossly underestimates the drag component of loading throughout the distance equal to the structure height. The comparison additionally shows that the prediction does not properly account for the reflected wave behavior. Near the structure face the technique results in an underestimate of reflected pressure level because the predicted average initial peak pressure level across the entire windward face was used in the determination. This average value incorrectly represents the reflection level at low angles of incidence near the ground plane. Away from the structure face (D = 0.5S) the comparison of reflected pressure levels is more favorable. However, the improved comparison is felt to be only coincidental. At the most removed point (D = 1.0S) the data suggest that the reflected wave has been
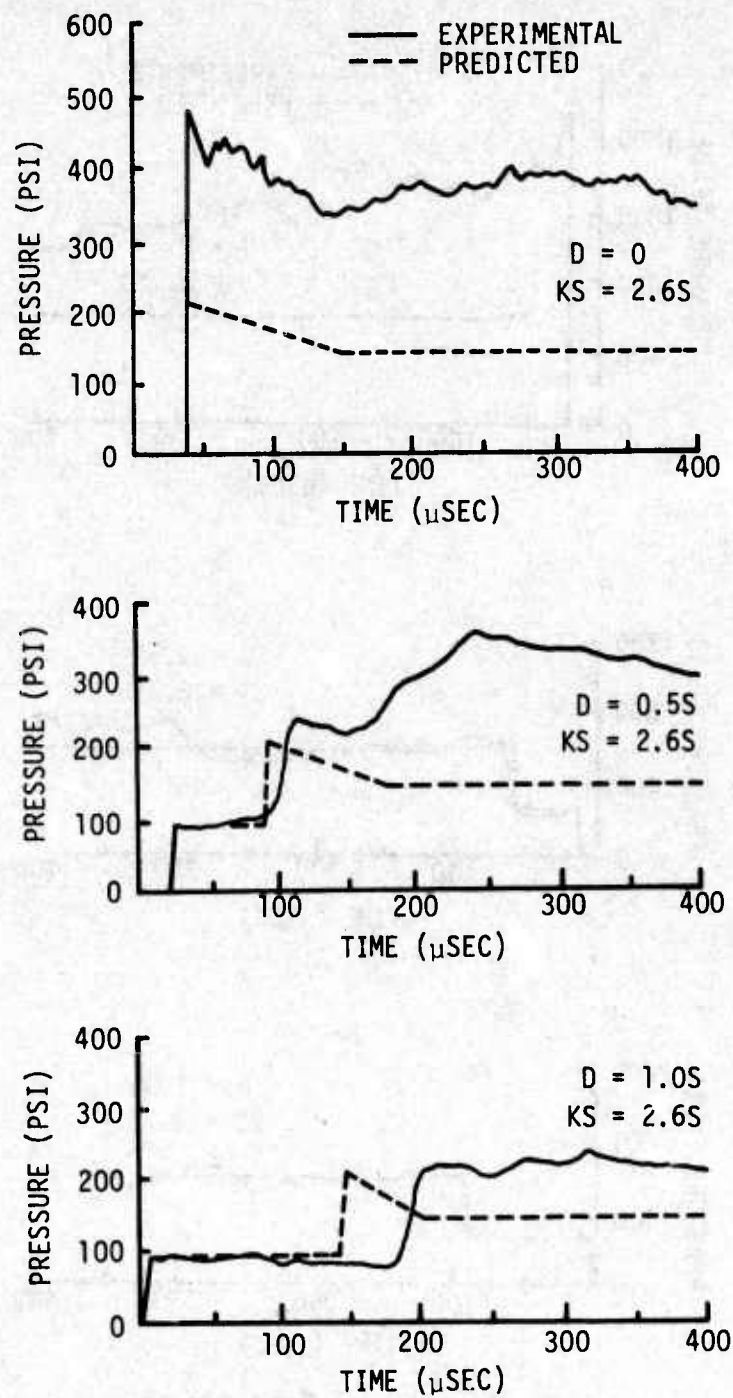
(a) 100 psi Overpressure

Figure 40. Experimental and Predicted Ground Surface Loading -
Arch Structure
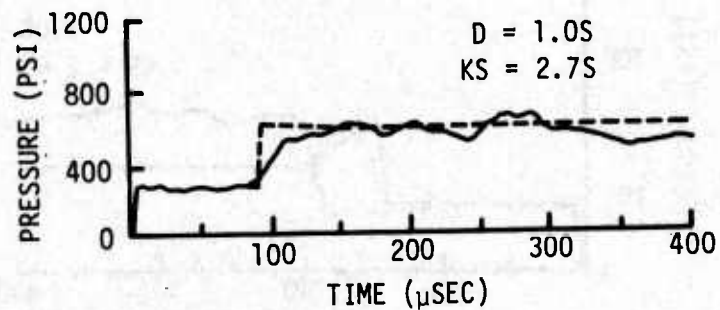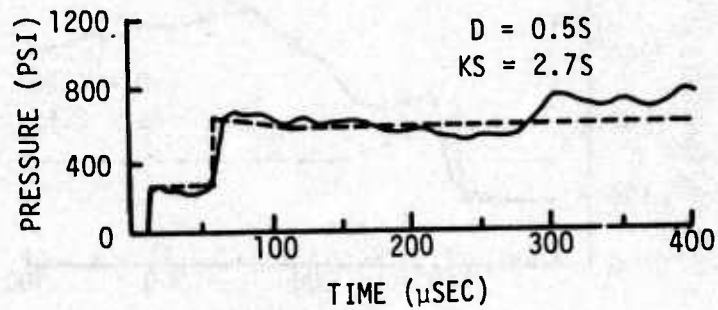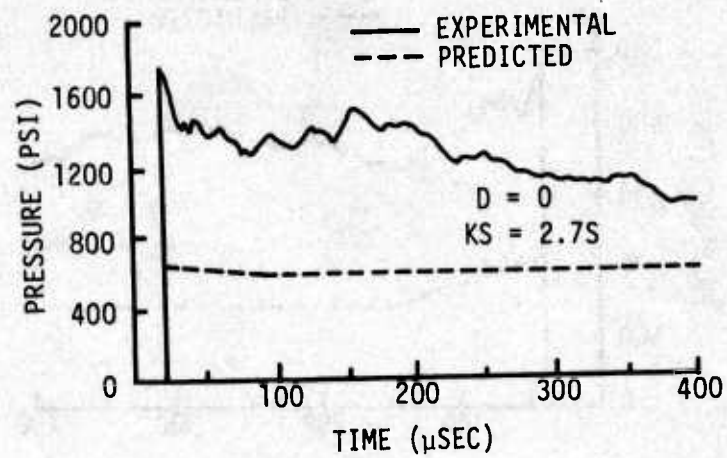
(b) 300 psi Overpressure

Figure 40. Experimental and Predicted Ground Surface Loading -
Arch Structure (Continued)
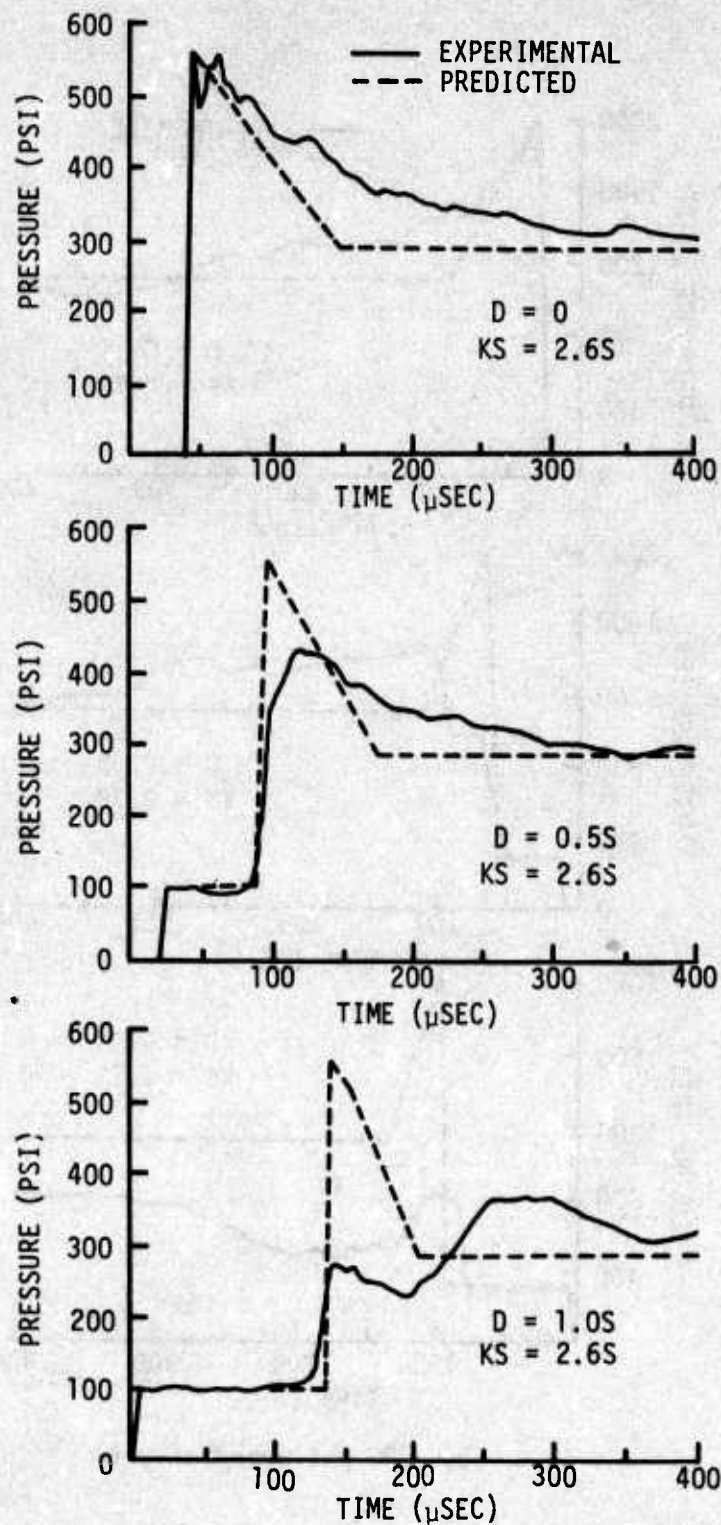
(a) 100 psi Overpressure

Figure 41. Experimental and Predicted Ground Surface Loading -
Rectangular Structure
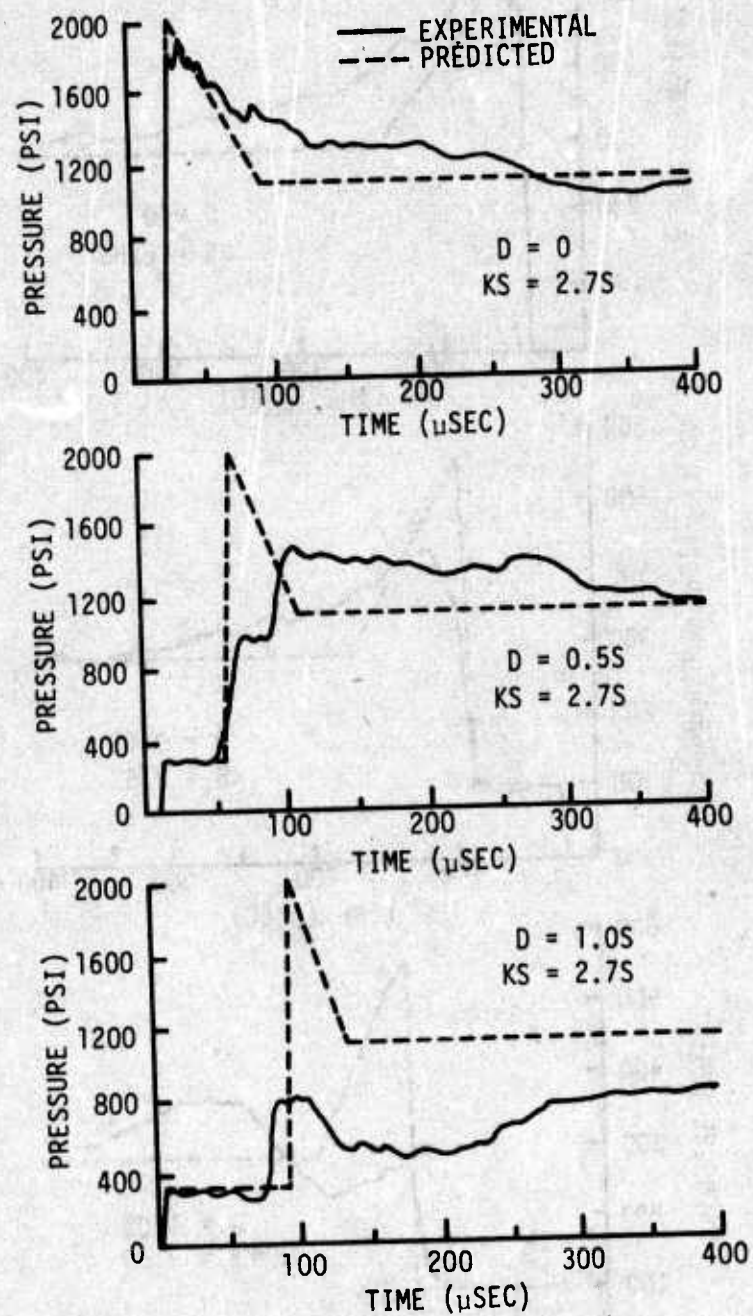
(b) 300 psi Overpressure

Figure 41. Experimental and Predicted Ground Surface Loading -
Rectangular Structure (Continued)

completely eroded by rarefactions and that drag loading effects only are felt at this point which is a reverse of the prediction technique. The later time dynamic pressure effects from the structure are seen to attenuate with distance from the structure face. This attenuation rate is much lower than that for the reflected wave. The indicated attenuation rate is such that the dynamic pressure effects are felt at a range in excess of the structure height. The underestimation of the drag loading again is related to the use of an average drag loading across the windward face which is not representative of the pressure levels near the ground plane. Had the predicted reflected pressure been determined using a reflection factor for zero angle of incidence, the near structure locations would have shown favorable comparisons. However, the locations farther from the structure would have shown large overestimates. A similar relationship would develop if a zero angle of incidence drag coefficient was used.

The comparison for the 300 psi arch shown in figure 40 b again shows an underestimate of reflected pressure level near the structure face. Unlike the previous comparison, though, the data show very good agreement between prediction and experiment for locations away from the structure face. This agreement also extends to the drag loading effects occurring in later time at the 0.5 and 1.0S locations. An immediate observation though is that the predicted levels of reflected pressure and drag loading are almost equal. This observation may suggest then that the actual quantity being measured at these locations is drag loading only and that the reflected wave has been relieved completely by rarefactions within a distance less than one half the structure height.

The experimental data for the arch structure have shown two important factors which are contrary to the prediction technique. The first is that the reflected pressure level attenuates rapidly with propagation distance. The second is that the drag loading effects are not constant over a distance equal to the structure height. Although not proven in this investigation the data additionally suggest that drag loading effects extend past a range equal to the structure height. Because of the limited data and complexity of the loading behavior no recommendations for changes to the prediction technique will be made. Instead, it is recommended that a preliminary analysis use either the incident overpressure only or the loading at the lower extremity of the structure face as the ground surface loading. The choice of which to

use will be dependent on the type of structure being investigated and the degree of conservatism desired. Ideally, additional analysis to include parametric investigations is needed which will define the attenuation rates of the reflected wave and drag pressure loadings as functions of structure radius and overpressure level. Once this is accomplished modification of the prediction technique is warranted.

The comparisons of experimental and predicted data for the rectangular structure are presented in figure 41 for each of the overpressure levels. These comparisons demonstrate essentially the same limitations in the prediction technique as were found for the arch structure. Specifically, the technique does not accurately represent the attenuation rates of the reflected wave and drag loading effects. Recognizing the similar limitations, the same recommendations concerning preliminary analyses and future improvement of the prediction technique are applicable to the rectangular structure. Additional efforts will be required to address the reason for the double reflection phenomena.

SECTION VI

SUMMARY

The objective of this investigation was to collect data describing high pressure shock diffraction associated with simple arch and rectangular structural shapes. Additional information was also collected from a stagnation probe mounted in the center of the shock tube test section. The data collected were then used to determine the adequacy of existing simplified prediction techniques. The prediction techniques evaluated were those proposed by the Air Force Manual for the Design and Analysis of Hardened Structures (AFWL-TR-74-102). In satisfying the above objective, the data were first presented in forms which provided both a general description of the loading phenomena and also more specific characteristics such as reflection factors, drag coefficients, and clearing times. The values determined for these more specific characteristics were then compared to values proposed by the preceding "Design Manual." Finally, the total structural loads predicted and measured were compared so that the accuracy of the prediction methods could be observed. The total structural loads were limited to average structure face loadings, overturning moments, structural support reactions, and ground surface loadings in front of the simple structural shapes.

The comparisons between recommended and experimentally measured reflection factors resulted in the following findings. For a disc-shaped plane (stagnation probe) the recommended values of reflection factors for incident overpressures between 90 and 330 psi are reliable. The arch structure tests revealed that reflection factors determined on an inclined planar surface at various angles of incidence may be used to represent reflection factors along the arch face at similar angles of incidence. Naturally, this finding is applicable only to the pressure levels investigated (100 and 300 psi overpressure). The major difference between the recommended and measured values occurred at the location of the extreme angle for Mach reflection which shifts with overpressure level. The recommended curve for a planar surface indicates a fixed position. The reflection factors determined for the rectangular structure suggested that the recommended values are somewhat conservative yielding higher values at the 100 and 300 psi overpressure levels.

The drag coefficient data determined during the stagnation probe tests revealed a large scatter in data which did not seem to be a result of experimental error. This statement is made based on the repeatability of other measurements. This wide data scatter suggests that dynamic pressure is very sensitive to test conditions when compared to the other measurements. The comparison between the median variation of measured drag coefficient and recommended value as functions of overpressure level showed that the measured curve indicated a larger increase in drag coefficient with overpressure levels. For the arch structure no comparison between drag coefficient and angle of incidence was possible since no recommended curves were presented for the overpressures of interest.

Comparisons were made, however, of net horizontal drag coefficient using recommended free stream cylinder values. The comparison showed the recommended values to be reliable. Average drag coefficients for the front and roof surfaces of the rectangular structure were compared. The front face comparison showed excellent agreement. Recommended drag coefficients for the roof structure were presented only for overpressures less than 130 psi which allowed only one comparison. The recommended value for the 100 psi overpressure test resulted in a large overestimate of roof surface loading. The data suggest that an average drag coefficient for the roof surface should be a function also of the structure dimensions and not just overpressure level.

The comparisons of total structural loading for the arch structure showed that the prediction techniques significantly underestimate the horizontal loading during the diffraction phase. At later times, the techniques are fairly reliable. For the average vertical loading, excellent agreement was found at the 100 psi level. However, a large underestimate of vertical loading was found at 300 psi overpressure after the diffraction phase. The comparisons of predicted and measured overturning moments for the arch structure showed excellent agreement at the 100 psi level and poor agreement at the higher level. This poor agreement plus the erroneous average vertical loading in the post diffraction period resulted in underestimates of as much as 30 percent for the vertical reactions. A review of the prediction technique to determine the reasons for these differences suggested that the prediction techniques do not adequately address reflection phenomena or later time drag pressure variations with structure position. Therefore, instead of recommending changes in the input values for the techniques it would be more appropriate to completely

revise the techniques. Since deficiencies were found in the techniques for gross structural behavior it is not recommended that they be used for refined analysis. The prediction techniques for the rectangular structure resulted in excellent loading determinations for the front face with the exception that the techniques underestimated the clearing time. A revised clearing time parameter is recommended which includes the estimated duration of the rarefaction wave. For the roof surface the techniques resulted in favorable loading during the diffraction process, but later time loads were significantly overestimated. A post diffraction drag coefficient and clearing time are recommended as changes to the prediction techniques. As a direct result of the overestimates of late time roof loadings, the prediction techniques underestimate the overturning moments acting on the structure at each overpressure which then result in erroneous vertical structural support reactions. The comparisons of predicted and measured ground surface loadings showed that the prediction techniques are seriously in error. Revision is necessary to include changes in the recommended attenuation rates of the reflected wave and attenuation rates should also be developed for the upstream effects of drag loading.

REFERENCES

1. Srinivasa, D.S., Airblast Loading Calculations-Parametric Study, To be Published.

2. Wright, J. K., Shock Tubes, John Wiley and Sons, Inc., New York, 1961.

3. Crawford, R.E., Higgins, C.J., and Bultmann, E.H., The Air Force Manual for Design and Analysis of Hardened Structures, AFWL-TR-74-102, Air Force Weapons Laboratory, Kirtland AFB, New Mexico, October 1975.

APPENDIX A

MODEL ST4 GAGE SPECIFICATIONS

Manufacturer	Susquehanna Instruments
Sensor	Tourmaline
Range	10 - 10,000 psi
Sensitivity	0.1 pcmbs/psi
Transducer Capacitance	10 pico Farads
Overload	Maximum Pressure 15,000 psi
Maximum Temperature	150°F Gauge, Intermittent Gas 5,000°F
Linearity	± 2 percent Full Scale
Natural Frequency	1.5 megahertz
Resistance	10^{10} ohms
Dimensions	1/2 inch diameter by 2 inches length

APPENDIX B

DESCRIPTION OF TESTS

Table B.1

STAGNATION PROBE SHOTS

MEAS. NO.	MODEL	INCIDENT PRESSURE		GAGE POSITION	MIXTURES	AMBIENT PRESSURE (PSI)	AMBIENT TEMP. (°C)
		TOP	BOTTOM				
295 296 297 298	Stag. Probe	95	95	Incident Incident Stag. Stag.	12 O_2 24 H_2	12.01	26.7
299 300 301 302	Stag. Probe	92	95	Incident Incident Stag. Stag.	12 O_2 24 H_2	12.02	26.7
303 304 305 306	Stag. Probe	135	135	Incident Incident Stag. Stag.	19 O_2 38 H_2	12.00	27.2
307 308 309 310	Stag. Probe	165	150	Incident Incident Stag. Stag.	22 O_2 44 H_2	11.99	28.9
311 312 313 314	Stag. Probe	167	155	Incident Incident Stag. Stag.	22 O_2 44 H_2	11.98	30.0
315 316 317 318	Stag. Probe	150	155	Incident Incident Stag. Stag.	22 O_2 44 H_2	12.09	26.7
319 320 321 322	Stag. Probe	230	217	Incident Incident Stag. Stag.	33 O_2 66 H_2	12.04	25.7
323 324 325 326	Stag. Probe	320	340	Incident Incident Stag. Stag.	50 O_2 100 H_2	12.04	24.4
327 328 329 330	Stag. Probe	300	300	Incident Incident Stag. Stag.	46 O_2 92 H_2	12.04	26.7

Table B.1

STAGNATION PROBE SHOTS (Continued)

MEAS. NO.	MODEL	INCIDENT PRESSURE		GAGE POSITION	MIXTURES	AMBIENT PRESSURE (PSI)	AMBIENT TEMP. (°C)
		TOP	BOTTOM				
331 332 333 334	Stag. Probe	100	100	Incident Incident Stag. Stag.	13 O_2 26 H_2	12.08	26.1
335 336 337 338	Stag. Probe	105	103	Incident Incident Stag. Stag.	13 O_2 26 H_2	12.06	26.1
339 340 341 342	Stag. Probe	110	104	Incident Incident Stag. Stag.	13 O_2 26 H_2	12.04	26.1
343 344 345 346	Stag. Probe	108	100	Incident Incident Stag. Stag.	12.5 O_2 25 H_2	12.00	24.9
347 348 349 350	Stag. Probe	105	106	Incident Incident Stag. Stag.	12.5 O_2 25 H_2	12.01	25.0
351 352 353 354	Stag Probe	145*	110	Incident Incident Stag. Stag.	12.5 O_2 25 H_2	12.00	24.4
355 356 357 358	Stag. Probe	120	105	Incident Incident Stag. Stag.	12.5 O_2 25 H_2	11.97	24.4
359 360 361 362	Stag. Probe	110	98	Incident Incident Stag. Stag.	12.5 O_2 25 H_2	11.98	25.0

* Questionable

Table B.2

ARCH MODEL SHOTS

MEAS. NO.	MODEL	INCIDENT PRESSURE		GAGE POSITION	MIXTURES	AMBIENT PRESSURE (PSI)	AMBIENT TEMP. (°C)
		TOP	BOTTOM				
1	Arch			Incident			
2	Arch			Incident			
3	Arch	105	100	190°	12.5 O_2	11.97	23.5
4	Arch			170°	25 H_2		
5	Arch			180°			
6	Arch			180°			
7	Arch			Incident			
8	Arch			Incident			
9	Arch	340	340	190°	50 O_2	11.97	23.0
10	Arch			170°	100 H_2		
11	Arch			180°			
12	Arch			180°			
13	Arch			Incident			
14	Arch			Incident			
15	Arch	105	100	145°	12.5 O_2	11.46	23.3
16	Arch			125°	25 H_2		
17	Arch			135°			
18	Arch			135°			
19	Arch			Incident			
20	Arch			Incident			
21	Arch	325	340	145°	46 O_2	11.94	23.6
22	Arch			125°	92 H_2		
23	Arch			135°			
24	Arch			Incident			
25	Arch			Incident			
26	Arch	110	100	100°	12.5 O_2	11.46	22.0
27	Arch			80°	25 H_2		
28	Arch			90°			
29	Arch			90°			
30	Arch			Incident			
31	Arch			Incident			
32	Arch	325	335	100°	46 O_2	11.97	21.5
33	Arch			80°	92 H_2		
34	Arch			90°			
35	Arch			Incident			
36	Arch			Incident			
37	Arch	105	100	80°	12.5 O_2	11.95	22.5
38	Arch			60°	25 H_2		
39	Arch			70°			
40	Arch			70°			

* Not Recorded

Table B.2

ARCH MODEL SHOTS (Continued)

MEAS. NO.	MODEL	INCIDENT PRESSURE		GAGE POSITION	MIXTURES	AMBIENT PRESSURE (PSI)	AMBIENT TEMP. (°C)
		TOP	BOTTOM				
41	Arch			Incident			
42	Arch			Incident			
43	Arch	110	105	10°	12.5 O_2	11.94	22.8
44	Arch			350°	25 H_2		
45	Arch			0°			
46	Arch			0°			
47	Arch			Incident			
48	Arch			Incident			
49	Arch	110	105	30°	12.5 O_2	12.05	23.3
50	Arch			10°	25 H_2		
51	Arch			20°			
52	Arch			20°			
53	Arch			Incident			
54	Arch			Incident			
55	Arch	105	110	50°	12.5 O_2	12.06	21.7
56	Arch			30°	25 H_2		
57	Arch			40°			
58	Arch			40°			
59	Arch			Incident			
60	Arch			Incident			
61	Arch	115	100	70°	12.5 O_2	12.06	22.8
62	Arch			50°	25 H_2		
63	Arch			Incident			
64	Arch			Incident			
65	Arch	110	110	90°	12.5 O_2	12.04	23.7
66	Arch			70°	25 H_2		
67	Arch			80°			
68	Arch			80°			
69	Arch			Incident			
70	Arch			Incident			
71	Arch	110	110	110°	12.5 O_2	12.03	23.7
72	Arch			90°	25 H_2		
73	Arch			100°			
74	Arch			100°			
75	Arch			Incident			
76	Arch			Incident			
77	Arch	110	110	140°	12.5 O_2	12.02	23.7
78	Arch			120°	25 H_2		
79	Arch			130°			
80	Arch			130°			

* Not Recorded

Table B.2

ARCH MODEL SHOTS (Continued)

MEAS. NO.	MODEL	INCIDENT PRESSURE		GAGE POSITION	MIXTURES	AMBIENT PRESSURE (PSI)	AMBIENT TEMP. (°C)
		TOP	BOTTOM				
81	Arch			Incident			
82	Arch			Incident			
83	Arch	105	110	170°	12.5 O_2	12.01	23.7
84	Arch			150°	25 H_2		
85	Arch			160°			
86	Arch			160°			
87	Arch			Incident			
88	Arch			Incident			
8.	Arch	105	110	20°	12.5 O_2	11.97	22.7
90	Arch			0°	25 H_2		
91	Arch			10°			
92	Arch			10°			
93	Arch			Incident			
95	Arch	310	*	0°	45 O_2	12.00	23.7
96	Arch			350°	90 H_2		
97	Arch			10°			
98	Arch			10°			
99	Arch			Incident			
100	Arch			Incident			
101	Arch	285	270	30°	44 O_2	11.98	23.8
102	Arch			20°	88 H_2		
103	Arch			40°			
104	Arch			Incident			
105	Arch			Incident			
106	Arch	300	315	50°	44 O_2	11.96	24.0
107	Arch			40°	88 H_2		
108	Arch			60°			
109	Arch			60°			
110	Arch			Incident			
111	Arch			Incident			
112	Arch	300	310	80°	44 O_2	11.96	23.5
113	Arch			70°	88 H_2		
114	Arch			90°			
115	Arch			90°			
116	Arch			Incident			
117	Arch			Incident			
118	Arch	300	235	110°	44 O_2	11.96	24.5
119	Arch			100°	88 H_2		
120	Arch			120°			
121	Arch			120°			

* Not Recorded

Table B.2

ARCH MODEL SHOTS (Continued)

MEAS. NO.	MODEL	INCIDENT PRESSURE		GAGE POSITION	MIXTURES	AMBIENT PRESSURE (PSI)	AMBIENT TEMP. (°C)
		TOP	BOTTOM				
122	Arch			Incident			
123	Arch			Incident			
124	Arch	290	275	140°	44 O_2	11.95	24.2
125	Arch			130°	88 H_2		
126	Arch			150°			
127	Arch			150°			
128	Arch			Incident			
129	Arch			Incident			
130	Arch	295	290	170°	44 O_2	11.95	24.3
131	Arch			160°	88 H_2		
132	Arch			180°			
133	Arch			180°			
134	Arch			Incident			
135	Arch			Incident			
136	Arch	305	295	20°	44 O_2	11.94	24.1
137	Arch			10°	88 H_2		
138	Arch			30°			
139	Arch			30°			
140				70°			
141	Ex-			80°			
142	tend-			90°	12.5 O_2	12.04	20.5
143	ed	105	125	90°	25 H_2		
144	Arch			Incident			
145				Incident			
146				70°			
147	Ex-			80°			
148	tend-	310	325	90°	44 O_2	12.02	20.75
149	ed			90°	88 H_2		
150	Arch			Incident			
151				Incident			
152	Arch			70°			
153	Arch			80°			
154	Arch	105	110	90°	12.5 O_2	11.92	*
155	Arch			90°	25 H_2		
156	Arch			Incident			
157	Arch			Incident			
158	Arch			70°			
159	Arch			80°			
160	Arch	295	290	90°	44 O_2	11.92	21.5
161	Arch			90°	88 H_2		
162	Arch			Incident			
163	Arch			Incident			

* Not Recorded

Table B.2

ARCH MODEL SHOTS (Continued)

MEAS. NO.	MODEL	INCIDENT PRESSURE		GAGE POSITION	MIXTURES	AMBIENT PRESSURE (PSI)	AMBIENT TEMP. (°C)
		TOP	BOTTOM				
164 165 166 167 168 169	Arch with wedge extension	110	110	1.0 R 0.5 R Stag. Stag. Incident Incident	12.5 O_2 25 H_2	11.92	20.5
170 171 172 173 174 175	Arch with wedge extension	105	110	1.0 R 0.5 R Stag. Stag. Incident Incident	12.5 O_2 25 H_2	11.91	21.5
176 177 178 179 180 181	Arch with wedge extension	280	325	1.0 R 0.5 R Stag. Stag. Incident Incident	44 O_2 88 H_2	11.89	22.0

Table B.3

RECTANGULAR MODEL SHOTS

MEAS.	MODEL	INCIDENT PRESSURE		GAGE POSITION	MIXTURES	AMBIENT PRESSURE (PSI)	AMBIENT TEMP. (°C)
		TOP	BOTTOM				
182				05F			
183				09F			
184				11F			
185	Rec-tangle	100	90*	07F	12.5 O_2	11.97	22.4
186				03F	25 H_2		
187				03F			
188				Incident			
189				Incident			
190				05F			
191				09F			
192				11F			
193	Rec-tangle	100	105	07F	12.5 O_2	11.92	22.5
194				03F	25 H_2		
195				Incident			
196				Incident			
197				05F			
198				09F			
199	Rec-tangle	315	310	11F	44 O_2	11.92	22.0
200				07F	88 H_2		
201				Incident			
202				Incident			
203				05F			
204				09F			
205				11F			
206	Rec-tangle	300	320	07F	44 O_2	11.90	23.0
207				03F	88 H_2		
208				03F			
209				Incident			
210				Incident			
211				05T			
212				09T			
213	Rec-tangle	100	*	11T	12.5 O_2	11.88	21.0
214				03T	25 H_2		
215				03T			
216				Incident			
217				05T			
218				09T			
219				11T			
220	Rec-tangle	280	310	03T	44 O_2	11.88	21.5
221				03T	88 H_2		
222				Incident			
223				Incident			

* Not Recorded

Table B.3

RECTANGULAR MODEL SHOTS (Continued)

MEAS. NO.	MODEL	INCIDENT PRESSURE		GAGE POSITION	MIXTURES	AMBIENT PRESSURE (PSI)	AMBIENT TEMP. (°C)
		TOP	BOTTOM				
224				19T			
225				15T			
226				13T			
227	Rec-tangle	290	310	17T	44 O_2 88 H_2	11.87	23.0
228				21T			
229				21T			
230				Incident			
231				Incident			
232				19T			
233				15T			
234				13T			
235	Rec-tangle	95	100	17T	12.5 O_2 25 H_2	11.85	24.2
236				21T			
237				21T			
238				Incident			
239				Incident			
240				19T			
241				15T			
242	Ex-tend-ed Rec-tangle	95	95	13T	12.5 O_2 25 H_2	11.97	22.0
243				17T			
244				21T			
245				21T			
246				Incident			
247				Incident			
248				19T			
249	Ex-tend-ed Rec-tangle	*	*	15T	44 O_2 88 H_2	11.98	22.5
250				13T			
251				17T			
252				21T			
253				21T			
254				19T			
255				15T			
256				13T			
257	Rec-tangle	100	*	17T	12.5 O_2 25 H_2	11.96	23.5
258				21T			
259				21T			
260				Incident			
262				19T			
263				15T			
264	Rec-tangle	300	*	13T	44 O_2 88 H_2	11.95	23.1
265				17T			
266				21T			
267				21T			
268				Incident			

* Not Recorded

113

Table B.3

RECTANGULAR MODEL SHOTS (Continued)

MEAS.	MODEL	INCIDENT PRESSURE		GAGE POSITION	MIXTURES	AMBIENT PRESSURE (PSI)	AMBIENT TEMP. (°C)
		TOP	BOTTOM				
269 270 271 272	Rec- tangle	110	170	05B Incident 03B Incident	12.5 O_2 25 H_2	12.03	19.75
273 274 275 276	Rec- tangle	285	*	05B Incident 03B 03B	44 O_2 88 H_2	12.02	20.5
277 278 279 280 281 282	Rec- tangle with wedge ex- ten- sion	110	125	1.0H 0.5H Stag. Stag. Incident Incident	12.5 O_2 25 H_2	11.94	21.1
283 284 285 286 287 288	Rec- tangle with wedge ex- ten- sion	295	340	1.0H 0.5H Stag. Stag. Incident Incident	12.5 O_2 25 H_2	11.93	21.7
289 290 291 292 293 294	Rec- tangle with wedge ex- ten- sion	275	325	1.0H 0.5H Stag. Stag. Incident Incident	12.5 O_2 25 H_2	11.92	23.0

* Not Recorded

APPENDIX C

TEST DATA TRACES

Table C.1. <u>LOCATION OF COMPOSITE DATA TRACES</u>

<u>Type of Data</u>	<u>Inclusive Page Numbers</u>
100 psi Arch	116 through 179
300 psi Arch	180 through 233
100 psi Rectangle	234 through 272
300 psi Rectangle	273 through 312

COMPOSITE 100-SA-INC
MN   1, 2,

COMPOSITE 100-SA-INC
MN   13, 14,

116

COMPOSITE 100-SA-INC
MN 24, 25,

PRESSURE(PSI) vs TIME(U-SEC)

COMPOSITE 100-SA-INC
MN 35, 36,

PRESSURE(PSI) vs TIME(U-SEC)

COMPOSITE 100-SA-INC
MN   41, 42,

COMPOSITE 100-SA-INC
MN   47, 48,

118

COMPOSITE 100-SA-INC
MN 53, 54,

COMPOSITE 100-SA-INC
MN 59, 60,

119

COMPOSITE 100-SA-INC
MN 63, 64,

COMPOSITE 100-SA-INC
MN 69, 70,

COMPOSITE 100-SA-INC
MN 75, 76,

PRESSURE(PSI)

TIME(U-SEC)

COMPOSITE 100-SA-INC
MN 81, 82,

PRESSURE(PSI)

TIME(U-SEC)

COMPOSITE 100-SA-INC
MN 87, 88,

COMPOSITE 100-SA-INC
MN 156, 157,

COMPOSITE 100-SA-0
MN 45, 90,

COMPOSITE 100-SA-10
MN 43, 44,

123

COMPOSITE 100-SA-10
MN 43, 44, 50, 91,

COMPOSITE 100-SA-20
MN 51, 89,

124

COMPOSITE 100-SA-30
MN 49, 56,

COMPOSITE 100-SA-50
MN 55, 62,

COMPOSITE 100-SA-70
MN   39, 61, 66, 152,

TIME(U-SEC)

COMPOSITE 100-SA-80
MN   27, 37, 67, 153,

TIME(U-SEC)

COMPOSITE 100-SA-90
MN 28, 65,

COMPOSITE 100-SA-90
MN 28, 65, 72,

COMPOSITE 100-SA-90
MN 28, 65, 72, 154,

COMPOSITE 100-SA-90
MN 28, 65, 154,

COMPOSITE 100-SA-100
MN   26, 73,

COMPOSITE 100-SA-170
MN   3, 4, 83,

100-SA-INC*001

100-SA-INC*002

100-SA-INC*013

100-SA-INC*014

100-SA-INC*024

100-SA-INC*025

132

100-SA-INC*035

PRESSURE(PSI) vs TIME(U-SEC)

100-SA-INC*036

PRESSURE(PSI) vs TIME(U-SEC)

133

100-SA-INC*041

100-SA-INC*042

100-SA-INC*047

100-SA-INC*048

135

100-SA-INC*053

PRESSURE(PSI)

200.

175.

150.

125.

100.

75.

50.

25.

-0.
0.   50. 100. 150. 200. 250. 300. 350. 400. 450. 500. 550. 600.
TIME(U-SEC)

100-SA-INC*054

PRESSURE(PSI)

200.

175.

150.

125.

100.

75.

50.

25.

-0.
0.   50. 100. 150. 200. 250. 300. 350. 400. 450. 500. 550. 600.
TIME(U-SEC)

100-SA-INC*059

100-SA-INC*060

137

100-SA-INC*063

100-SA-INC*064

100-SA-INC*069

100-SA-INC*070

100-SA-INC*075

PRESSURE(PSI)

TIME(U-SEC)

100-SA-INC*076

PRESSURE(PSI)

TIME(U-SEC)

100-SA-INC*081

100-SA-INC*082

100-SA-INC*087

100-SA-INC*088

100-SA-INC*156

100-SA-INC*157

143

100-SA- 0*045

PRESSURE(PSI)

TIME(U-SEC)

100-SA- 0*046

PRESSURE(PSI)

TIME(U-SEC)

100-SA-   0*090

100-SA- 10*043

100-SA-350*044

100--SA- 10*050

100-SA- 10*091

100-SA- 10*092

147

100-SA- 20*051

100-SA- 20*052

148

100-SA- 20*089

100-SA- 30*049

149

100-SA- 30*056

100-SA- 40*057

150

100-SA- 40*058

100-SA- 50*055

100-SA- 50*062

100-SA- 60*038

100-SA- 70*039

100-SA- 70*040

100-SA- 70*061

100-SA- 70*066

154

100-SA- 70*152

100-SA- 80*027

100-SA- 80*037

100-SA- 80*067

156

100-SA- 80*068

100-SA- 80*153

100-SA- 90*028

100-SA- 90*029

158

100-SA   90*065

100-SA- 90*072

159

100-SA- 90*154

100-SA- 90*155

160

100-SA-100*026

100-SA-100*073

100-SA-100*074

100-SA-110*071

100-SA-120*078

100-SA-125*016

100-SA-130*079

100-SA-130*080

100-SA-135*017

PRESSURE(PSI)

175.

150.

125.

100.

75.

50.

25.

0.

-25.
0. 50. 100. 150. 200. 250. 300. 350. 400. 450. 500. 550. 600.
TIME(U-SEC)

100-SA-135*018

PRESSURE(PSI)

175.

150.

125.

100.

75.

50.

25.

0.

-25.
0. 50. 100. 150. 200. 250. 300. 350. 400. 450. 500. 550. 600.
TIME(U-SEC)

100-SA-140*077

100-SA-145*015

100-SA-150*084

100-SA-160*085

167

100-SA-160*086

100-SA-170*004

100-SA-170*083

100-SA-190*003

100-SA-180*005

100-SA-180*006

100-EA-INC*144

100-EA-INC*145

100-EA- 70*140

100-EA- 80*141

172

100-EA- 90*142

100-EA- 90*143

100-WA-INC*168

100-WA-INC*169

100-WA-INC*174

100-WA-INC*175

175

100-WA-1.0R*164

100-WA-1.0R*170

100-WA-0.5R*165

100-WA-0.5R*171

177

100-WA-STAG*166

100-WA-STAG*167

178

100-WA-STAG*172

100-WA-STAG*173

179

COMPOSITE 300-SA-INC
MN 7, 8,

COMPOSITE 300-SA-INC
MN 19, 20,

COMPOSITE 300-SA-INC
MN 30, 31,

COMPOSITE 300-SA-INC
MN 93, 99,

COMPOSITE 300-SA-INC
MN 104, 105,

COMPOSITE 300-SA-INC
MN 110, 111,

COMPOSITE 300-SA-INC
MN 116, 117,

COMPOSITE 300-SA-INC
MN 122, 123,

COMPOSITE 300-SA-INC
MN 128, 129,

COMPOSITE 300-SA-INC
MN 134, 135,

184

COMPOSITE 300-SA-INC
MN 162, 163,

COMPOSITE 300-SA-350
MN 96, 97,

185

COMPOSITE 300-SA-10
MN 96, 97, 137,

COMPOSITE 300-SA-20
MN 102, 136,

COMPOSITE 300-SA-30
MN 101, 138,

COMPOSITE 300-SA-40
MN 103, 107,

COMPOSITE 300-SA-70
MN 113, 158,

COMPOSITE 300-SA-80
MN 33, 112, 159,

COMPOSITE 300-SA-90
MN 114, 160,

COMPOSITE 300-SA-90
MN 34, 114, 160,

COMPOSITE 300-SA-90
MN 34, 114,

COMPOSITE 300-SA-100
MN 32, 119,

190

COMPOSITE 300-SA-170
MN   9, 10,

COMPOSITE 300-SA-170
MN   9, 10, 130,

191

COMPOSITE 300-SA-170
MN 10, 130,

COMPOSITE 300-SA-180
MN 11, 132,

192

COMPOSITE 300-EA-INC
MN 150, 151,

COMPOSITE 300-WA-INC
MN 180, 181,

300-SA-INC*007

300-SA-INC*008

300-SA-INC*019

300-SA-INC*020

300-SA-INC*030

300-SA-INC*031

300-SA-INC*093

300-SA-INC*099

197

300-SA-INC*100

300-SA-INC*104

300-SA-INC*105

300-SA-INC*110

300-SA-INC*111

300-SA-INC*116

300-SA-INC*117

300-SA-INC*122

300-SA-INC*123

300-SA-INC*128

300-SA-INC*129

300-SA-INC*134

203

300-SA-INC*135

PRESSURE(PSI)

TIME(U-SEC)

300-SA-INC*162

PRESSURE(PSI)

TIME(U-SEC)

300-SA-INC*163

300-SA- 0*095

300-SA-350*096

300-SA- 10*097

300-SA- 10*098

207

300-SA- 10*137

300-SA- 20*102

300-SA- 20*136

300-SA- 30*101

300-SA- 30*138

300-SA- 30*139

300-SA- 40*103

300-SA- 40*107

211

300-SA- 50*106

300-SA- 60*108

300-SA- 70*158

300-SA- 80*033

213

300-SA- 60*109

300-SA- 70*113

300-SA- 80*112

300-SA- 80*159

300-SA- 90*034

300-SA- 90*114

216

300-SA- 90*115

300-SA- 90*160

217

300-SA-110*118

300-SA-120*120

300-SA-120*121

300-SA-125*022

300-SA-130*125

300-SA-125*023

300-SA-140*124

300-SA-145*021

300-SA-150*126

300-SA-150*127

300-SA-160*131

300-SA-170*010

224

300-SA-170*130

300-SA-190*009

300-SA-180*011

300-SA-180*012

300-SA-180*132

300-SA-180*133

227

300-EA- 70*146

300-EA- 80*147

300-EA- 90*148

300-EA- 90*149

300-WA-INC*180

300-WA-INC*181

231

300-WA-1.OR*176

300-WA-0.5R*177

232

300-WA-STAG*178

300-WA-STAG*179

233

COMPOSITE 100-SR-INCF
MN 188, 195, 196,

COMPOSITE 100-SR-INCF
MN 195, 196,

COMPOSITE 100-SR-INCT
MN 238, 239,

COMPOSITE 100-SR-INCT
MN 216, 238, 239, 260,

235

COMPOSITE 100-SR-INCB
MN 270, 272,

COMPOSITE 100-SR-11F
MN 184, 192,

236

COMPOSITE 100-SR-09F
MN 183, 191,

COMPOSITE 100-SR-07F
MN 185, 193,

237

COMPOSITE 100-SR-05F
MN 182, 190,

COMPOSITE 100-SR-03F
MN 186, 194,

238

COMPOSITE 100-SR-15T
MN 233, 255,

COMPOSITE 100-SR-17T
MN 235, 257,

239

COMPOSITE 100-SR-19T
MN 232, 254,

COMPOSITE 100-ER-INCT
MN 246, 247,

COMPOSITE 100-WR-INC
MN 281, 282,

COMPOSITE 100-SA-190
MN 3, 4,

COMPOSITE 100-EA-INC
MN 144, 145,

COMPOSITE 100-WA-INC
MN 168, 169,

COMPOSITE 100-WA-INC
MN 170, 175,

COMPOSITE 100-WA-1.0R
MN 164, 170,

COMPOSITE 100-WA-0.5R
MN 165, 171,

COMPOSITE 100-WA-STAG
MN 166, 173,

100-SR-INCF*188

100-SR-INCF*189

100-SR-INCF*195

100-SR-INCF*196

247

100-SR-INCT*216

100-SR-INCT*238

100-SR-INCT*239

100-SR-INCT*260

249

100-SR-INCB*270

100-SR-INCB*272

100-SR-11F*184

100-SR-11F*192

100-SR-09F*183

100-SR-09F*191

100-SR-07F*185

PRESSURE(PSI)

TIME(U-SEC)

100-SR-07F*193

PRESSURE(PSI)

TIME(U-SEC)

100-SR-O5F*182

100-SR-O5F*190

254

100-SR-03F*186

100-SR-03F*187

100-SR-03F*194

100-SR-03T*214

100-SR-03T*215

100-SR-05T*211

100-SR-09T*212

100-SR-11T*213

100-SR-13T*234

100-SR-13T*256

100-SR-15T*233

100-SR-15T*255

100-SR-17T*235

100-SR-17T*257

100-SR-19T*232

100-SR-19T*254

100-SR-21T*236

100-SR-21T*237

263

100-SR-21T*258

100-SR-21T*259

100-SR-U3B*271

100-SR-05B*269

100-ER-INCT*246

100-ER-INCT*247

266

100-ER-13T*242

100-ER-15T*241

100-ER-17T*243

100-ER-19T*240

100-ER-21T*244

100-ER-21T*245

100-WR-INC*281

100-WR-INC*282

100-WR-1.0H=277

100-WR-0.5H=278

271

100-WR-STAG*279

100-WR-STAG*280

COMPOSITE 300-SR-INCF
MN 201, 202,

COMPOSITE 300-SR-INCF
MN 209, 210,

COMPOSITE 300-SR-INCF
MN 201, 202, 209, 210,

COMPOSITE 300-SR-INCT
MN 222, 223,

274

COMPOSITE 300-SR-INCT
MN 230, 231,

COMPOSITE 300-SR-INCT
MN 222, 223, 230, 231, 268,

COMPOSITE 300-SR-11F
MN 199, 205,

COMPOSITE 300-SR-09F
MN 198, 204,

COMPOSITE 300-SR-07F
MN 200, 206,

COMPOSITE 300-SR-05F
MN 197, 203,

277

COMPOSITE 300-SR-13T
MN 226, 264,

COMPOSITE 300-SR-15T
MN 225, 263,

COMPOSITE 300-SR-17T
MN 227, 265,

COMPOSITE 300-SR-19T
MN 224, 262,

COMPOSITE 300-SR-21T
MN 228, 266,

COMPOSITE 300-WR-INC
MN 287, 288,

COMPOSITE 300-WR-INC
MN 293, 294,

COMPOSITE 300-WR-INC
MN 287, 288, 293, 294,

COMPOSITE 300-WR-1.0H
MN 283, 289,

COMPOSITE 300-WR-0.5H
MN 284, 290,

COMPOSITE 300-WR-STAG
MN 285, 292,

300-SR-INCF*201

300-SR-INCF*202

284

300-SR-INCF*209

300-SR-INCF*210

300-SR-INCT*222

300-SR-INCT*223

300-SR-INCT*230

300-SR-INCT*231

300-SR-INCT*268

300-SR-INCB*274

300-SR-11F*199

300-SR-11F*205

300-SR-09F*198

300-SR-09F*204

300-SR-07F*200

300-SR-07F*206

291

300-SR-05F*197

300-SR-05F*203

292

300-SR-03F*207

300-SR-03F*208

300-SR-03T*220

300-SR-03T*221

300-SR-05T*217

300-SR-09T*218

300-SR-11T*219

300-SR-13T*226

296

300-SR-13T*264

300-SR-15T*225

300-SR-15T*263

300-SR-17T*227

300-SR-17T*265

300-SR-19T*224

299

300-SR-19T*262

300-SR-21T*228

300-SR-21T*229

300-SR-21T*266

301

300-SR-21T*267

300-SR-03B*275

302

300-SR-03B*276

300-SR-05B*273

303

300-ER-17T*251

300-ER-19T*248

300-ER-21T*252

300-ER-21T*253

306

300-WR-INC#287

300-WR-INC#288

300-WR-INC*293

300-WR-INC*294

300-WR-1.0H*283

300-WR-1.0H*289

300-WR-0.5H*284

300-WR-0.5H*290

300-WR-STAG≠285

300-WR-STAG≠286

311
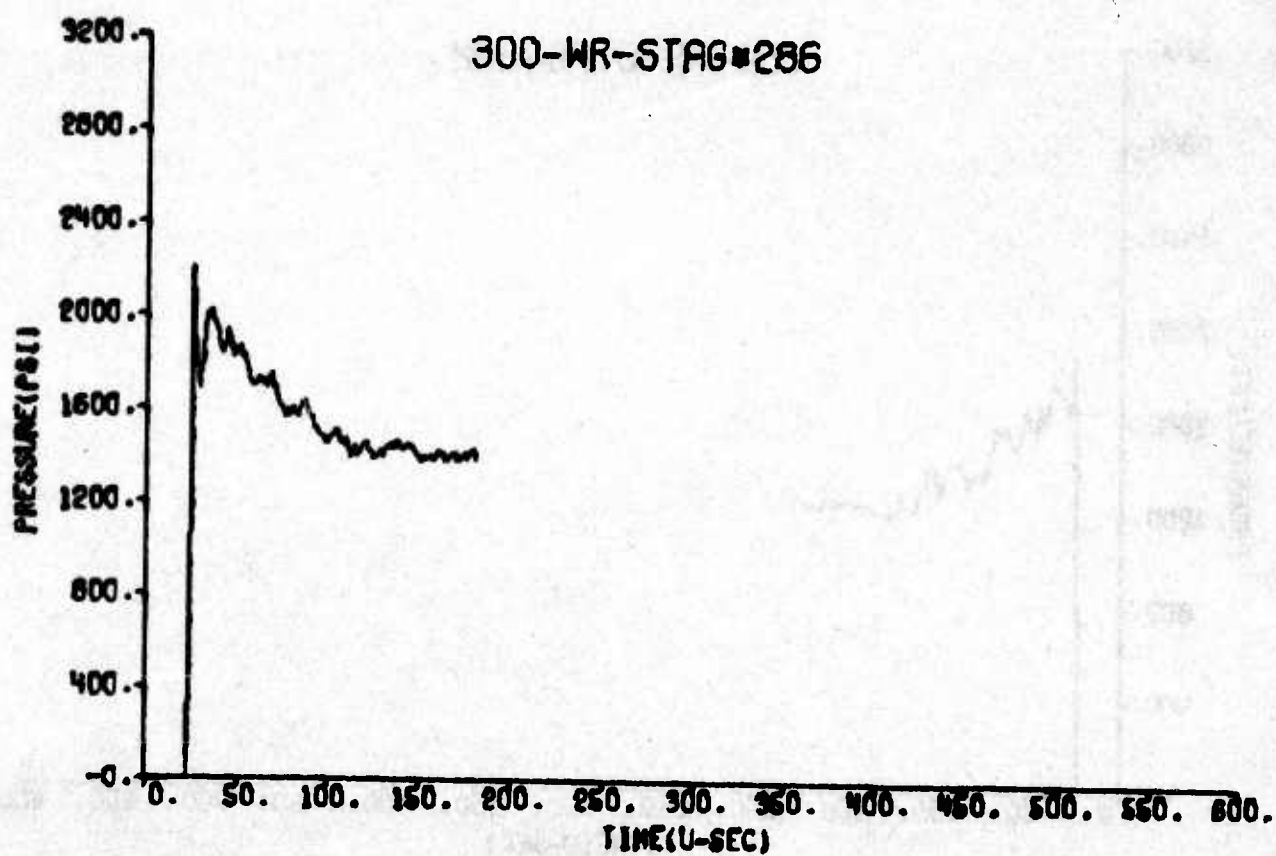
300-WR-STAG#291

300-WR-STAG#292

Table C.2   LOCATION OF INDIVIDUAL DATA TRACES, STAGNATION PROBE

Gage Location	Measurement Number	Page Number
Incident	295	316
Incident	296	316
FF	297	317
FF	298	317
Incident	299	318
Incident	300	318
FF	301	319
FF	302	319
Incident	303	320
Incident	304	320
FF	305	321
FF	306	321
Incident	307	322
Incident	308	322
FF	309	323
FF	310	323
Incident	311	324
Incident	312	324
FF	313	325
FF	314	325
Incident	315	326
Incident	316	326
FF	317	327
FF	318	327
Incident	319	328

313

Table C.2 (cont'd)

Gage Location	Measurement Number	Page Number
Incident	320	328
FF	321	329
FF	322	329
Incident	323	330
Incident	324	330
FF	325	331
FF	326	331
Incident	327	332
Incident	328	332
FF	329	333
FF	330	333
Incident	331	334
Incident	332	334
FF	333	335
FF	334	335
Incident	335	336
Incident	336	336
FF	337	337
FF	338	337
Incident	339	338
Incident	340	338
FF	341	339
FF	342	339
Incident	343	340

Table C.2 (cont'd)

Gage Location	Measurement Number	Page Number
Incident	344	340
FF	345	341
FF	346	341
Incident	347	342
Incident	348	342
FF	349	343
FF	350	343
Incident	351	344
Incident	352	345
FF	353	345
FF	354	345
Incident	355	346
Incident	356	346
FF	357	347
FF	358	348
Incident	359	348
Incident	360	348
FF	361	349
FF	362	349

1-STAG.PROBE-INC*295

1-STAG.PROBE-INC*296

316

1-STAG.PROBE-FF *297

1-STAG.PROBE-FF *298

2-STAG.PROBE-INC*299

PRESSURE(PSI)

TIME(U-SEC)

2-STAG.PROBE-INC*300

PRESSURE(PSI)

TIME(U-SEC)

2-STAG.PROBE-FF *301

2-STAG.PROBE-FF *302

3-STAG.PROBE-INC*303

3-STAG.PROBE-INC*304

320

3-STAG.PROBE-FF*305

3-STAG.PROBE-FF *306

4-STAG.PROBE-INC*307

4-STAG.PROBE-INC*308

322

4-STAG.PROBE-FF *309

4-STAG.PROBE-FF *310

5-STAG.PROBE-INC*311

PRESSURE(PSI)

TIME(U-SEC)

5-STAG.PROBE-INC*312

PRESSURE(PSI)

TIME(U-SEC)

5-STAG.PROBE-FF *313

5-STAG.PROBE-FF *314

6-STAG.PROBE-INC*315

PRESSURE(PSI)

TIME(U-SEC)

6-STAG.PROBE-INC*316

PRESSURE(PSI)

TIME(U-SEC)

6-STAG.PROBE-FF *317

6-STAG.PROBE-FF *318

327

7-STAG.PROBE-INC*319

PRESSURE(PSI)

TIME(U-SEC)

7-STAG.PROBE-INC*320

PRESSURE(PSI)

TIME(U-SEC)

7-STAG.PROBE-FF *321

7-STAG.PROBE-FF *322

8-STAG.PROBE-INC*323

8-STAG.PROBE-INC*324

8-STAG.PROBE-FF *325

8-STAG.PROBE-FF *326

9-STAG.PROBE-INC*327

PRESSURE(PSI) vs TIME(U-SEC)

9-STAG.PROBE-INC*328

PRESSURE(PSI) vs TIME(U-SEC)

9-STAG.PROBE-FF *329

9-STAG.PROBE-FF *330

10-STAG.PROBE-INC*331

10-STAG.PROBE-INC*332

334

10-STAG.PROBE-FF *333

10-STAG.PROBE-FF *334

335

11-STAG.PROBE-INC*335

11-STAG.PROBE-INC*336

11-STAG.PROBE-FF *337

11-STAG.PROBE-FF *338

12-STAG.PROBE-INC×339

12-STAG.PROBE-INC×340

12-STAG·PROBE-FF ✳341

12-STAG·PROBE-FF ✳342

339

13-STAG.PROBE-INC*343

13-STAG.PROBE-INC*344

340

13-STAG.PROBE-FF *345

13-STAG.PROBE-FF *346

14-STAG.PROBE-INC*347

14-STAG.PROBE-INC*348

14-STAG.PROBE-FF *349

14-STAG.PROBE-FF *350

15-STAG.PROBE-INC*351

15-STAG.PROBE-INC*352

15-STAG.PROBE-FF *353

15-STAG.PROBE-FF *354

16-STAG.PROBE-INC*355

16-STAG.PROBE-INC*356

346

16-STAG.PROBE-FF *357

16-STAG.PROBE-FF *358

17-STAG.PROBE-INC*359

17-STAG.PROBE-INC*360

17-STAG.PROBE-FF *361

17-STAG.PROBE-FF *362

DISTRIBUTION LIST

DEPARTMENT OF DEFENSE

Assistant to the Secretary of Defense
Atomic Energy
    ATTN: Honorable Donald R. Cotter

Director
Defense Advanced Research Projects Agency
    ATTN: Tech. Lib.
    ATTN: NMRO
    ATTN: PMO
    ATTN: STO
    ATTN: NMR
    ATTN: Dr. Stan Ruby

Director
Defense Civil Preparedness Agency
    ATTN: Staff Dir., Research, George N. Sisson
    ATTN: Tech. Lib.

Director
Defense Communications Agency
    ATTN: Code 930
    ATTN: Code 930, Franklin D. Moore

Defense Documentation Center
2 cy ATTN: TC

Director
Defense Intelligence Agency
    ATTN: DI-7D, Edward O'Farrell
    ATTN: DI-7E
    ATTN: DIAAP-8B
    ATTN: DIAST-3
    ATTN: DT-1C, Jack Vorona
    ATTN: DT-2, Wpns. & Sys. Div.
    ATTN: Tech. Lib.

Director
Defense Nuclear Agency
    ATTN: DDST
    ATTN: STAP
    ATTN: STSI, Archives
2 cy ATTN: STTL, Tech. Lib.
3 cy ATTN: SPSS

Chairman
Department of Defense Explo. Safety Board
    ATTN: DD/S&SS
    ATTN: Thomas Zaker

Director of Defense Research & Engineering
Department of Defense
    ATTN: AD/SW
    ATTN: DD/I&SS
    ATTN: DD/S&SS
    ATTN: DD/TWP

Commander
Field Command
Defense Nuclear Agency
    ATTN: FCPR
    ATTN: FCT
    ATTN: FCTMO
    ATTN: Captain T. Edwards

DEPARTMENT OF DEFENSE (Continued)

Commandant
Industrial College of the Armed Forces
    ATTN: Tech. Lib.

Director
Interservice Nuclear Weapons School
    ATTN: Tech. Lib.

Director
Joint Strategic Target Planning Staff, JCS
    ATTN: JLTW
    ATTN: JLTW-2
    ATTN: DOXT
    ATTN: STINFO Library
    ATTN: XPFS

Chief
Livermore Division, Field Command, DNA
    ATTN: FCPRL

Chief
LVLO
    ATTN: FCTC

Commandant
National War College
    ATTN: NWCLB-CR

Weapons Systems Evaluation Group
    ATTN: Doc. Con.

DEPARTMENT OF THE ARMY

Assistant Chief of Staff for Ops. & Plans
    ATTN: Dir. of Chem. & Nuc. Ops.
    ATTN: Tech. Lib.

Commander
Ballistic Defense System Command
    ATTN: BDMSC-TEN, Noah J. Hurst

Director
BMD Advanced Tech. Ctr.
Huntsville Office
    ATTN: CRDABH-X
    ATTN: CRDABH-S

Manager
BMD Program Office
    ATTN: John Shea

ESD
    ATTN: DEE

Chief of Research, Development & Acquisition
Department of the Army
    ATTN: Tech. Lib.

Department of the Army
NIKE-X Field Office
    ATTN: AMCPM-NXE-FB

Chief of Engineers
Department of the Army
    ATTN: ENGMC-EM

DEPARTMENT OF THE ARMY (Continued)

Director
Construction Engineering Research Lab.
    ATTN: CERL-SL
    ATTN: Library

Commanding Officer
USACDC

Commander
Harry Diamond Laboratories
    ATTN: AMXDO-NP
    ATTN: AMXDO-RBI, John A. Rosado
    ATTN: AMXDO-TI, Tech. Lib.

Department of the Army
Office Chief of Engineers
    ATTN: DAEN-MCE-D
    ATTN: DAEN-RDM

Commander
Picatinny Arsenal
    ATTN: Tech. Lib.

Director
U.S. Army Ballistic Research Labs.
    ATTN: J. H. Keefer
    ATTN: W. Taylor
    ATTN: AMXBR-X, Julius J. Meszaros
    ATTN: Edward Baicy, Tech. Lib.

Commander
U.S. Army Communications Command
    ATTN: Tech. Lib.

Commander
U.S. Army Engineer Center
    ATTN: ATSEN-SY-L

Project Engineer
U.S. Army Engineer District, Huntsville
    ATTN: HNDSE-R, Michael M. Dembo

Division Engineer
U.S. Army Engineer District, Ohio River
    ATTN: Tech. Lib.

Director
U.S. Army Engineer Waterways Experiment Station
    ATTN: James Ballard
    ATTN: Guy Jackson
    ATTN: William Flathau
    ATTN: John N. Strange
    ATTN: Leo Ingram
    ATTN: Tech. Lib.
3 cy ATTN: WESRL

Commander
U.S. Army Mat. & Mechanics Research Center
    ATTN: Richard Shea
    ATTN: John Mescall
    ATTN: Tech. Lib.

Commander
U.S. Army Materiel Command
    ATTN: Research & Concepts Branch

DEPARTMENT OF THE ARMY (Continued)

Commander
U.S. Army Materiel Command
    ATTN: W. H. Hubbard
    ATTN: Tech. Lib.
    ATTN: AMCRD-WN-RE, John F. Corrigan
2 cy ATTN: AMCRD-BN
2 cy ATTN: AMCRD-WN

Commander
U.S. Army Missile Command
    ATTN: Tech. Lib.
    ATTN: AMSMI-XS, Chief Scientist

Commander
U.S. Army Mobility Equipment R & D Center
    ATTN: Tech. Lib.

Commander
U.S. Army Nuclear Agency
    ATTN: Tech. Lib.
    ATTN: ATCA-NAW

Commandant
U.S. Army War College
    ATTN: Library

Commander
U.S. Army Weapons Command
    ATTN: Tech. Lib.

DEPARTMENT OF THE NAVY

NCEL
3 cy

Chief of Naval Material
Navy Department
    ATTN: MAT 0323

Chief of Naval Operations
Navy Department
    ATTN: OP-03EG
    ATTN: OP-985F

Chief of Naval Research
Navy Department
    ATTN: Nicholas Perrone
    ATTN: Tech. Lib
    ATTN: Code 464, Thomas P. Quinn
    ATTN: Code 464, Jacob L. Warner

Officer-in-Charge
Civil Engineering Laboratory
    ATTN: Stan Takahashi
    ATTN: R. J. Odello
    ATTN: Tech. Lib.

Commander
Naval Electronic Systems Command
Naval Electronic Systems Command Headquarters
    ATTN: PME 117-21A

Superintendent
Naval Postgraduate School
    ATTN: Code 2124, Tech. Rpts. Lib.

DEPARTMENT OF THE NAVY (Continued)

Commander
Naval Facilities Engineering Command
Headquarters
    ATTN: Code 03A
    ATTN: Code 04B
    ATTN: Code 04B, M. Yachnis
    ATTN: Tech. Lib.

Director
Naval Research Laboratory
    ATTN: Code 2027, Tech. Lib.
    ATTN: Code 8404
    ATTN: Code 8440, F. Rosenthal

Commander
Naval Sea Systems Command
Navy Department
    ATTN: Code 03511
    ATTN: ORD-91313, Library

Commander
Naval Ship Engineering Center
    ATTN: NSEC 6105G
    ATTN: Tech. Lib.

Commander
Naval Ship Research & Development Center
    ATTN: Code L42-3, Library

Commander
Naval Ship Research & Development Center
Underwater Explosive Research Division
    ATTN: John Gordon
    ATTN: Code 17, William W. Murray
    ATTN: Tech. Lib.

Commander
Naval Surface Weapons Center
    ATTN: Code 241, J. Petes
    ATTN: Code 730, Tech. Lib.
    ATTN: Code 1224, Navy Nuc. Prgms. Off.

Commander
Naval Surface Weapons Center
    ATTN: Tech. Lib.

Commander
Naval Undersea Center
    ATTN: E. P. Cooper
    ATTN: Tech. Lib.

President
Naval War College
    ATTN: Tech. Lib.

Commander
Naval Weapons Center
    ATTN: Paul Cordle
    ATTN: Carl Austin
    ATTN: Code 533, Tech. Lib.

Commanding Officer
Naval Weapons Evaluation Facility
    ATTN: R. Hughes
    ATTN: Code ADS
    ATTN: Tech. Lib.

ONR
Department of the Navy
    ATTN: Code 418

DEPARTMENT OF THE NAVY (Continued)

Director
Strategic Systems Project Office
Navy Department
    ATTN: NSP-43, Tech. Lib.
    ATTN: NSP-272

DEPARTMENT OF THE AIR FORCE

AFTAC

Commander
ADC/DE
    ATTN: DDEEN
2 cy ATTN: DOA

Commander
ADC/XP
    ATTN: XP
    ATTN: XPQDQ
    ATTN: XPXY

Commander
Aeronautical Systems Division, AFSC
    ATTN: Tech. Lib.

AF Armament Laboratory, AFSC
    ATTN: DLOSL, Library

AF Cambridge Research Labs., AFSC
    ATTN: LWW, Ker C. Thompson
    ATTN: SUOL, AFCRL, Research Lib.

AF Institute of Technology, AU
    ATTN: CES
    ATTN: Library, AFIT, Bldg. 640, Area B

AFCEC
    ATTN: PREC

AFFDL
    ATTN: Library

AFML
    ATTN: Tech. Lib.

AFOSR
    ATTN: W. Walker

AU
    ATTN: ED, Dir., Civ. Eng.

AUL
    ATTN: LDE

AF Weapons Laboratory, AFSC
    ATTN: DEV, M. A. Plamondon
    ATTN: DEV, Jimmie L. Bratton
    ATTN: DE-I
    ATTN: DEX
    ATTN: DE
    ATTN: DYT
    ATTN: Robert Henny
    ATTN: Robert Port
    ATTN: Capt Jerry S. Doughty
    ATTN: HO, Dr. Minge
2 cy ATTN: SUL
5 cy ATTN: DEV

Headquarters
Air Force Systems Command
    ATTN: DLCAW
    ATTN: Tech. Lib.
    ATTN: DO
    ATTN: DOB
    ATTN: DLSP

Commander
Armament Development & Test Center
    ATTN: ADBRL-2
    ATTN: Tech. Lib.

Commander
Foreign Technology Division, AFSC
    ATTN: TD-BTA Library

HQUSAF/IN
    ATTN: INATA
    ATTN: IN

CINCUSAFE
    ATTN: DOA

CINCPACAF
    ATTN: DOA

HQUSAF/PR
    ATTN: PRE
    ATTN: PREE
    ATTN: PREPB

HQUSAF/SA
    ATTN: SAMI

HQUSAF/RD
    ATTN: RDPM
    ATTN: RDQS
    ATTN: RDQPN
    ATTN: RDPQ

HQUSAF/XO
    ATTN: XOOWD

Commander
Rome Air Development Center, AFSC
    ATTN: EMTLD, Document Library

SAMSO/DE
    ATTN: DEB
    ATTN: DEN

SAMSO/DY
    ATTN: DYS

SAMSO/MN
    ATTN: MNN
    ATTN: MNNH
    ATTN: MNI
    ATTN: MMH

SAMSO/XR
    ATTN: XRTB

USAFA
    ATTN: DFSLB
3 cy ATTN: DFCE

TAC
    ATTN: DEE
    ATTN: LGMD

DEPARTMENT OF THE AIR FORCE (Continued)

Director of Nuclear Safety
    ATTN: SN

Commander in Chief
Strategic Air Command
    ATTN: DEE
    ATTN: DOXS
    ATTN: NRI-STINFO Library
    ATTN: XPFC
    ATTN: XPFS

ENERGY RESEARCH & DEVELOPMENT ADMINISTRATION

Division of Military Application
U.S. Energy Research & Development Administration
    ATTN: Doc. Con. for Test Office

Holmes & Narver, Inc.
    ATTN: R. Kennedy

University of California
Lawrence Berkeley Laboratory
    ATTN: Tech. Info. Dept.

University of California
Lawrence Livermore Laboratory
    ATTN: Jack Kahn
    ATTN: J. R. Hearst, L-41
    ATTN: J. Coruthers, L-18
    ATTN: Richard G. Dong, L-424
    ATTN: Robert Schock
    ATTN: Larry W. Woodruff, L-125
    ATTN: Tech. Info. Dept., L-3
    ATTN: Ted Butkovich
    ATTN: Douglas Stephens
    ATTN: D. M. Norris, L-90
    ATTN: Library

Los Alamos Scientific Laboratory
    ATTN: Doc. Con. for Reports Lib.
    ATTN: Doc. Con. for Al Davis
    ATTN: Doc. Con. for G. R. Spillman

Sandia Laboratories
Livermore Laboratory
    ATTN: Doc. Con. for L. Hill
    ATTN: Doc. Con. for Tech. Lib.

Sandia Laboratories
    ATTN: Doc. Con. for 3141, Sandia Rpt. Coll.
    ATTN: Doc. Con. for A. J. Chaban
    ATTN: Doc. Con. for M. L. Merritt
    ATTN: Doc. Con. for W. Roherty
    ATTN: Doc. Con. for Luke J. Vortman

U.S. Energy Research & Development Administration
Albuquerque Operations Office
    ATTN: Doc. Con. for Tech. Lib.

U.S. Energy Research & Development Administration
Division of Headquarters Services
    ATTN: Doc. Con. for Class. Tech. Lib.

U.S. Energy Research & Development Administration
Nevada Operations Office
    ATTN: Doc. Con. for Tech. Lib.

ENERGY RESEARCH & DEVELOPMENT ADMINISTRATION (Continued)

Union Carbide Corporation
Holifield National Laboratory
    ATTN: Doc. Con. for Tech. Lib.
    ATTN: Civil Def. Res. Proj.

OTHER GOVERNMENT AGENCIES

Bureau of Mines
Twin Cities Research Center
    ATTN: Tech. Lib.

Department of the Interior
Bureau of Mines
    ATTN: Tech. Lib.

Department of the Interior
U.S. Geological Survey
    ATTN: Cecil B. Raleigh
    ATTN: J. H. Healy

DEPARTMENT OF DEFENSE CONTRACTORS

Aerospace Corporation
    ATTN: Prem N. Mathur
    ATTN: Library
    ATTN: Tech. Info. Services

Agbabian Associates
    ATTN: M. Agbabian

Analytic Services, Inc.
    ATTN: George Hesselbacher

Applied Theory, Inc.
2 cy ATTN: John G. Trulio

Artec Associates, Inc.
    ATTN: Steven Gill

Avco Research & Systems Group
    ATTN: Research Library, A-830, Rm. 7201

Battelle Memorial Institute
    ATTN: R. W. Klingesmith
    ATTN: Tech. Lib.

The BDM Corporation
    ATTN: A. Lavagnino
    ATTN: Tech. Lib.

The BDM Corporation
    ATTN: Richard Hensley
    ATTN: Mr. George Pringle

Bechtel Corporation
    ATTN: P. L. Williams

The Boeing Company
    ATTN: Aerospace Library
2 cy ATTN: R. H. Carlson

Brown Engineering Company, Inc.
    ATTN: Manu Patel
    ATTN: J. Cahoon

Jack Cahoon & Associates

DEPARTMENT OF DEFENSE CONTRACTORS (Continued)

California Research & Technology, Inc.
    ATTN: Ken Kreyenhagen
    ATTN: Tech. Lib.

University of California
    ATTN: G. Sackman

Calspan Corporation
    ATTN: Tech. Lib.

Civil Engineering Res. Fac.
5 cy ATTN: Tech. Lib.

Civil/Nuclear Systems Corporation
    ATTN: Robert Crawford

University of Dayton
    ATTN: Hallock F. Swift

University of Denver
    ATTN: Sec. Officer for Fred P. Venditti
    ATTN: Sec. Officer for J. Wisotski
    ATTN: Sec. Officer for Ron W. Buchanon
    ATTN: Sec. Officer for Tech. Lib.

EG&G, Inc.
Albuquerque Division
    ATTN: Tech. Lib.

Environmental Research Corporation
    ATTN: W. W. Hays

General American Transportation Corporation
General American Research Division
    ATTN: G. L. Neidhardt

General Electric Company
Space Division
    ATTN: M. H. Bortner, Space Sci. Lab.

General Electric Company
TEMPO-Center for Advanced Studies
    ATTN: DASIAC

General Research Corporation
    ATTN: Benjamin Alexander

IIT Research Institute
    ATTN: Milton R. Johnson
    ATTN: R. E. Welch
    ATTN: Tech. Lib.

Institute for Defense Analyses
    ATTN: IDA, Librarian, Ruth S. Smith

J. H. Wiggins Co., Inc.
    ATTN: John Collins

J. L. Merritt
Consulting & Special Engr. Svs., Inc.
    ATTN: J. L. Merritt
    ATTN: Tech. Lib.

Kaman Sciences Corporation
    ATTN: Frank H. Shelton
    ATTN: Paul A. Ellis
    ATTN: Library

Kaman AviDyne
Division of Kaman Sciences Corporation
    ATTN: Norman P. Hobbs
    ATTN: E. S. Criscione
    ATTN: Tech. Lib.

Lockheed Missiles & Space Co. Inc.
    ATTN: Tech. Lib.

Lockheed Missiles & Space Company
    ATTN: Tom Geers, Dept. 52-33, Bldg. 205
    ATTN: Tech. Info. Ctr., D/Coll.

Lovelace Foundation for Medical Education
    ATTN: Asst. Dir. of Res., Robert K. Jones
    ATTN: Tech. Lib.

Martin Marietta Aerospace
Orlando Division
    ATTN: G. Fotieo

McDonnell Douglas Corporation
    ATTN: Robert W. Halprin
    ATTN: Library

Mechanics Research, Inc.

Meteorology Research, Inc.
    ATTN: William D. Green

The Mitre Corporation
    ATTN: Library

Nathan M. Newmark
Consulting Engineering Services
    ATTN: Nathan M. Newmark

Pacifica Techology
    ATTN: R. Bjork
    ATTN: J. Kent

R. M. Parsons Company
    ATTN: Mr. Herb Saffell

Physics International Company
    ATTN: Doc. Con. for Charles Godfrey
    ATTN: Doc. Con. for E. T. Moore
    ATTN: Doc. Con. for Dennis Orphal
    ATTN: Doc. Con. for Fred M. Sauer
    ATTN: Doc. Con. for Coye Vincent
    ATTN: Doc. Con. for Tech. Lib.
    ATTN: Doc. Con. for Robert Swift
    ATTN: Doc. Con. for Larry A. Behrmann

R & D Associates
    ATTN: Jerry Carpenter
    ATTN: Sheldon Schuster
    ATTN: William B. Wright, Jr.
    ATTN: J. G. Lewis
    ATTN: Tech. Lib.
    ATTN: Harold L. Brode
    ATTN: Cyrus P. Knowles
    ATTN: Bruce Hartenbaum
    ATTN: Henry Cooper
    ATTN: Albert L. Latter

The Rand Corporation
    ATTN: C. C. Mow
    ATTN: Library

Research Analysis Corporation
    ATTN: Documents Library

Science Applications, Inc.
    ATTN: D. E. Maxwell
    ATTN: David Bernstein

Science Applications, Inc.
    ATTN: R. Seebaugh
    ATTN: John Mansfield
    ATTN: William M. Layson

Science Applications, Inc.
    ATTN: Michael McKay
    ATTN: Tech. Lib.

Science Applications, Inc.
    ATTN: R. A. Shunk

Shock Hydrodynamics, Inc.
A Division of Whittaker Corporation
    ATTN: L. Zernow

Southwest Research Institute
    ATTN: Wilfred E. Baker
    ATTN: A. B. Wenzel

Stanford Research Institute
    ATTN: Burt R. Gasten
    ATTN: Carl Peterson
    ATTN: George R. Abrahamson
    ATTN: SRI, Library, Rm. G-021

Sundstrand Corporation
    ATTN: Curtis B. White

Systems, Science & Software, Inc.
    ATTN: Thomas D. Riney
    ATTN: Robert T. Allen
    ATTN: Tech. Lib.
    ATTN: Donald R. Grine
    ATTN: Ted Cherry

Terra Tek, Inc.
    ATTN: Sidney Green
    ATTN: A. H. Jones
    ATTN: Tech. Lib.

Tetra Tech, Inc.
    ATTN: Tech. Lib.
    ATTN: Li-San Hwang

TRW Systems Group
    ATTN: Tech. Info. Ctr., S-1930
    ATTN: Pravin Bhutta
    ATTN: Paul Lieberman
    ATTN: William Rowan
    ATTN: Norm Lipner
    ATTN: Jack Farrell
    ATTN: Benjamin Sussholtz
3 cy ATTN: Dr. P. Dai

TRW Systems Group
San Bernardino Operations
3 cy ATTN: Greg Hulcher

Universal Analytics, Inc.
    ATTN: E. I. Field

DEPARTMENT OF DEFENSE CONTRACTORS (Continued)

University of Illinois
    ATTN: Dr. N. M. Newmark
    ATTN: Dr. W. Hall
    ATTN: Dr. J. Haltiwanger

URS Research Company
    ATTN: Ruth Schneider
    ATTN: Tech. Lib.

The Eric H Wang
Civil Engineering Research Facility
    ATTN: Neal Baum
    ATTN: Larry Bickle

Washington State University
Administrative Office
    ATTN: Arthur Miles Hohorf for George Duval

Weidlinger Assoc. Consulting Engineers
    ATTN: Melvin L. Baron

Weidlinger Assoc. Consulting Engineers
    ATTN: J. Isenberg

Westinghouse Electric Company
    ATTN: W. A. Volz